

AD-A134 594

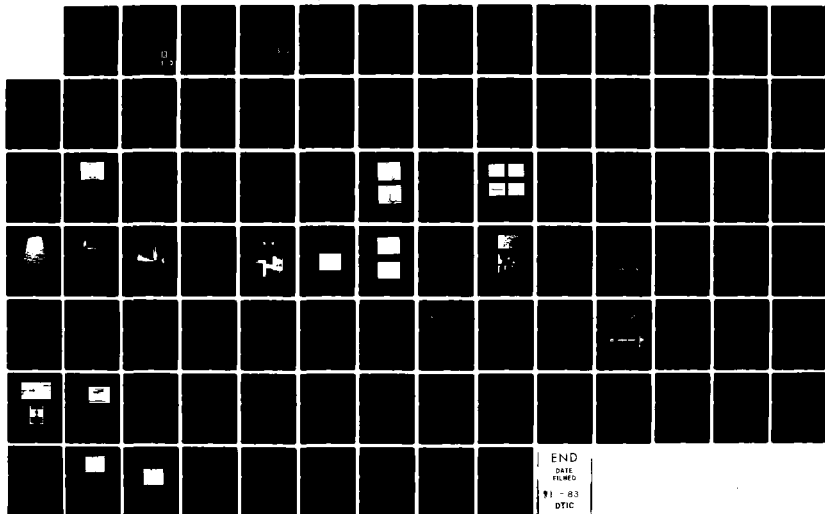
SOLID STATE RESEARCH WORK OF THE SOLID STATE DIVISION  
AT LINCOLN LABORATORY(U) MASSACHUSETTS INST OF TECH  
LEXINGTON LINCOLN LAB A L MCWHORTER 15 MAY 83 1983-2  
ESD-TR-83-029

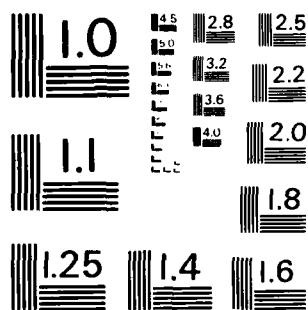
1/1

UNCLASSIFIED

F/G 20/12

NL



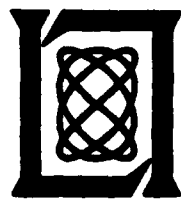


MICROCOPY RESOLUTION TEST CHART  
NATIONAL BUREAU OF STANDARDS - 1963 - A

A134 594

12

ESD-TR-83-029

	2
Solid State Research	1983
Prepared under Electronic Systems Division Contract F19628-80-C-0002 by <b>Lincoln Laboratory</b> MASSACHUSETTS INSTITUTE OF TECHNOLOGY LEXINGTON, MASSACHUSETTS	

DTIC FILE COPY

Approved for public release; distribution unlimited.

DTIC  
ELECTE  
NOV 9 1983  
S B

83 11 00 001

The work reported in this document was performed at Lincoln Laboratory, a center for research operated by Massachusetts Institute of Technology, with the support of the Department of the Air Force under Contract F19628-80-C-0002.

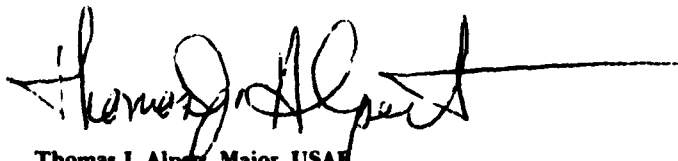
This report may be reproduced to satisfy needs of U.S. Government agencies.

The views and conclusions contained in this document are those of the contractor and should not be interpreted as necessarily representing the official policies, either expressed or implied, of the United States Government.

The Public Affairs Office has reviewed this report, and it is releasable to the National Technical Information Service, where it will be available to the general public, including foreign nationals.

This technical report has been reviewed and is approved for publication.

FOR THE COMMANDER



Thomas J. Alpert, Major, USAF  
Chief, ESD Lincoln Laboratory Project Office

Non-Lincoln Recipients

**PLEASE DO NOT RETURN**

Permission is given to destroy this document  
when it is no longer needed.

MASSACHUSETTS INSTITUTE OF TECHNOLOGY  
LINCOLN LABORATORY

**SOLID STATE RESEARCH**

**QUARTERLY TECHNICAL SUMMARY REPORT**

1 FEBRUARY — 30 APRIL 1983

ISSUED 10 AUGUST 1983

DTIC  
ELECTE  
S NOV 9 1983 D  
B

Approved for public release; distribution unlimited.

LEXINGTON

MASSACHUSETTS

SEP 10 1983 SEPTEMBER 9, 1983 015

## ABSTRACT

This report covers in detail the solid state research work of the Solid State Division at Lincoln Laboratory for the period 1 February through 30 April 1983. The topics covered are Solid State Device Research, Quantum Electronics, Materials Research, Microelectronics, and Analog Device Technology. Funding is primarily provided by the Air Force, with additional support provided by the Army, DARPA, Navy, NASA, and DOE.

Approved for	
NTIS	<input checked="" type="checkbox"/>
DTIC	
Unannounced	
Justification	
Page	
Distribution	
Availability Codes	
Available and/or	
Dist Special	
<b>A-1</b>	



## TABLE OF CONTENTS

Abstract	iii
List of Illustrations	vii
List of Tables	x
Introduction	xi
Reports on Solid State Research	xv
Organization	xxv
 1. SOLID STATE DEVICE RESEARCH	 1
1.1 2-Bit 1-GSample/s Electrooptic Guided-Wave Analog-to-Digital Converter System	1
1.2 Broadband Guided-Wave Optical Frequency Translator Using an Electrooptical Bragg Array	4
 2. QUANTUM ELECTRONICS	 5
2.1 Combined Signal Averaging and Cross-Correlation Effects in Laser Remote Sensing	5
2.2 Optical Heterodyne Spectroscopy with Frequency and Amplitude Modulated GaAlAs Diode Lasers	6
2.3 UV Laser-Initiated Deposition of Al <sub>2</sub> O <sub>3</sub>	11
 3. MATERIALS RESEARCH	 15
3.1 Reduction in Impurity Striations in InP Crystals Grown by the Liquid-Encapsulated Czochralski Method	15
3.2 Lateral Bipolar/MOS Transistors Fabricated in Zone- Melting-Recrystallized Si Films on SiO <sub>2</sub>	19
3.3 Dual-Ion Implantation Technique for Formation of Shallow p <sup>+</sup> /n Junctions in Silicon	23
3.4 Electronic Structure of Deep-Lying Sulfur Centers in Si	27
3.5 Hole Traps in Tungsten-Doped GaAs Grown by Molecular Beam Epitaxy	31

4. MICROELECTRONICS	37
4.1 A Precise Wide-Range Optical Scheme for Gap Measurements	37
4.2 Monolithic Frequency Doublers	39
4.3 Resonant Tunneling Through Quantum Wells at Frequencies Up to 2.5 THz	49
5. ANALOG DEVICE TECHNOLOGY	55
5.1 Low-Loss Substrates for Superconductive Circuits	55
5.1.1 Supported Silicon Substrates	55
5.1.2 Material Evaluation Technique	56
5.1.3 Substrate Properties	57
5.2 Superconductor-Insulator-Superconductor Junctions	58
5.3 Paraxial Electroacoustic Coefficients in $\text{LiNbO}_3$ and $\text{LiTaO}_3$ and Their Application to Holographically Written Bulk Acoustic Wave Gratings	63
5.3.1 Experimental Determination of Electroacoustic Coefficients	63
5.3.2 Application to Holographically Written Acoustic Gratings	63



## LIST OF ILLUSTRATIONS

Figure No.		Page
1-1	Schematic Diagram of Guided-Wave Electrooptic A/D Converter	1
1-2	Schematic Test System for A/D Converter. Switches Permit Simultaneous D/A Reconstructions Derived from Any Two Samples.	2
1-3	Beat-Frequency Test of Electrooptic A/D Converter. The Frequency of the Input RF Test Signal Is 499 MHz and the Sampling Rate Is 1 GHz. Shown Are a Derived Beat Signal (Top Trace) and Reconstructed Beat Signal from Adjacent Samples (Middle and Bottom Traces).	3
2-1	Experimental Setup for Optical Heterodyne Spectroscopy with Diode Lasers	7
2-2	Power Spectrum of Current-Modulated TJS Diode Laser: (a) $\nu_m = 750$ MHz; (b) $\nu_m = 2.6$ GHz	8
2-3	Heterodyne Spectrum of Fabry-Perot Resonance: (a) In-Phase Signal, $\nu_m = 750$ MHz; (b) Quadrature Signal, $\nu_m = 750$ MHz; (c) In-Phase Signal, $\nu_m = 2.6$ GHz; (d) Quadrature Signal, $\nu_m = 2.6$ GHz	10
2-4	UV Laser-Induced Film Deposition System	12
2-5	Refractive Index and Thickness of Laser-Deposited $\text{Al}_2\text{O}_3$ Films as Function of Position Across Film. The Central Region Was Irradiated at a 193-nm Energy Fluence of 0.7 mJ/cm <sup>2</sup> (Top) and 1.6 mJ/cm <sup>2</sup> (Bottom). The Substrate Temperature Was 400°C.	13
3-1	X-Ray Topograph of (110) Longitudinal Section from Sn-Doped LEC InP Crystal	16
3-2	Absorption Coefficient at 10.6 $\mu\text{m}$ and Carrier Concentration Vs. Distance from Seed End of Sn-Doped LEC InP Crystal	17
3-3	Absorption Coefficient at 10.6 $\mu\text{m}$ and Carrier Concentration Vs. Distance from Seed End of Sn-Doped LEC Crystal	18
3-4	(a) Cross Section of Lateral Bipolar/MOS Transistor Fabricated in Zone-Melting-Recrystallized Si Film, and Photomicrograph (Top View) (b) of a Finished Device	20
3-5	Drain-Source I-V Characteristics of Device Operated as n-Channel MOSFET with Gate Voltages of 0-7 V	21

Figure No.		Page
3-6	Source-Drain (Emitter-Collector) I-V Characteristics of Device Operated with Base and Gate Contacts Floating	22
3-7	Common-Emitter Characteristics of Device Operated as Lateral npn Bipolar Transistor	22
3-8	TEM Micrographs for Annealed Si Samples with (a) Single B <sup>+</sup> Implant, (b) Si <sup>+</sup> Implant at Room Temperature Followed by B <sup>+</sup> Implant, (c) Si <sup>+</sup> Implant at LN <sub>2</sub> Temperature Followed by B <sup>+</sup> Implant	24
3-9	Boron Depth Profiles Obtained by SIMS Analysis for Samples with (a) Single B <sup>+</sup> Implant and (b) Successive Si <sup>+</sup> and B <sup>+</sup> Implants	26
3-10	Current-Voltage Characteristic of Diode with Shallow p <sup>+</sup> /n Junction Produced by Dual-Ion Implantation Technique	28
3-11	Energy Levels of S Centers in Si	29
3-12	Results of Capacitance Vs. Temperature and ODLTS Measurements on a GaAs Layer (3-58) Grown by MBE in the Presence of a W Flux	32
3-13	Results of Capacitance Vs. Temperature Measurements on GaAs Layers (3-55, 3-56, 3-58) Grown by MBE in the Presence of a W Flux and on a Control Layer (3-59) Grown Without a W Flux	32
4-1	Optical Scheme to Measure Gap Between Two Plane Surfaces	37
4-2	Illustration of the Position of Virtual Point Sources Which Result from Multiple Reflections Between Planes 1 and 2	38
4-3	Experimental System to Determine Accuracy of Gap Measurement Scheme. Auxiliary Interferometer Measures Relative Motion of Mask and Substrate with High Accuracy.	40
4-4	Plot of Gap Measurement Error Vs. Gap. Lines Bounding $\pm 0.25\%$ Error Are Shown.	41
4-5	Scaled Model for Design of Monolithic Frequency Doublers. Scaling Factor Is 22.57 to 1.	41
4-6	Planar Monolithic Varactor Diode with n and n <sup>+</sup> Epitaxial Layers for Anode and Cathode Contacts, Respectively. Transmission Lines Are Formed Over Proton Bombarded Regions.	42

Figure No.		Page
4-7	Highlights of Fabrication Sequence: (a) Ohmic Contact Formation; (b) Device Isolation: Mesa and Proton Bombardment; (c) Schottky Barrier Formation and Circuit Plating	44
4-8	Monolithic Frequency Doubler. Varactor Diode Is Integrated with Microstrip Circuits and Bias Lines. Chip Dimensions: $4 \times 8$ mm.	45
4-9	(Right) Monolithic Varactor Diode. Diode Terminals Are Integral Part of Embedding Circuit.	45
4-10	Junction Capacitance Vs. Reverse Bias Voltage of Monolithic Varactor Diode. Inset: Forward Diode Currents Vs. Bias Voltage in a Multiple-Exposure Photograph. Traces Correspond to Three Current Scales: 1, 10, and $100 \mu\text{A}/\text{div}$ .	46
4-11	Output Power Vs. Output Frequency Curve of Monolithic Varactor Frequency Doubler at Test Fixture Terminals	47
4-12	Measured Output Power and Conversion Efficiency of Monolithic Varactor Frequency Doubler as a Function of Input Power at Test Fixture Terminals	48
4-13	Electron Energy as a Function of Position in Quantum Well Structure. Parameters Are $N_{D1} = N_{D3} = 10^{18} \text{ cm}^{-3}$ , $N_{D2} = 10^{17} \text{ cm}^{-3}$ , and $W_1 = W_2 = W_3 = 52 \text{ \AA}$ . Doping Level in Well Center Is an Average Value Achieved by Placing a Layer of $10^{18} \text{ cm}^{-3}$ Material in the Central 10% of the Well. Energy Level $E_1$ Occurs Above the Bottom of the Bulk Conduction Band Because of Confinement in x-Direction.	50
4-14	Curves for (a) Current-Voltage and (b) Conductance ( $dI/dV$ )-Voltage at Several Temperatures. Resonant Tunneling Features Can be Seen Even at Room Temperature.	52
4-15	Current Response at 2.5 THz as a Function of dc Bias Voltage. Dashed Curve Is Calculated on the Basis of the dc I-V Curve. Zero dB Corresponds to $0.3 \mu\text{A/W}$ . The General Agreement Shows That I-V Curve at 2.5 THz Is Very Similar to dc Curve, and Thus the Charge Transport Is Fast.	53

Figure No.		Page
5-1	Proposed Fabrication of 25- $\mu$ m-Thick Silicon Wafers by Epitaxial Deposition and Preferential Etching: (a) Starting Material; (b) Assembly After Deposition of Nb Ground Plane and Bonding to Support Wafer; (c) Completed Structures After the Preferential Removal of the Original Substrate, Nb Deposition and Photolithographic Definition of Stripline Circuit	55
5-2	Test Structures to Evaluate Substrates: (a) Simple Resonator, (b) Multiple Resonator, (c) Resonator and Delay Line	56
5-3	I-V Characteristics of a Nb/Nb <sub>2</sub> O <sub>5</sub> /Pb Tunnel Junction Showing Significant Parameters	59
5-4	I-V Characteristics of a Nb/Nb <sub>2</sub> O <sub>5</sub> /Pb Junction at 4.2°K. Vertical Scales Are 1 and 0.1 mA/div; Horizontal Scale Is 1 mV div.	60
5-5	I-V Characteristics of a Series Array of 21 SIS Junctions at 4.2°K	61
5-6	Normal Junction Current at 4.2°K as a Function of Room-Temperature Storage Time	62
5-7	Relative Velocity Change of a Longitudinal Z-Propagating Bulk Acoustic Wave: (a) in LiNbO <sub>3</sub> , (b) in LiTaO <sub>3</sub>	64

## LIST OF TABLES

Table No.		Page
3-1	Growth Conditions and Electrical Properties of MBE GaAs Layers	33
5-1	Resonator Q for Different Substrate Materials	57
5-2	SIS Tunnel Junction Characteristics	59

## INTRODUCTION

### 1. SOLID STATE DEVICE RESEARCH

An electrooptic analog-to-digital converter system has been demonstrated at 1 Gsample/s with a range of 2 bits. This converter consists of a pulsed GaAlAs diode laser, a LiNbO<sub>3</sub> integrated optical modulator array, Si avalanche photodiodes, and the necessary wideband electronics. A 499-MHz sinusoid has been A/D converted, and a slowed version reconstructed.

A new type of optical frequency translator has been demonstrated which utilizes Bragg diffraction from a traveling index wave produced by an interdigitated electrode grating on a LiNbO<sub>3</sub> surface waveguide. Measurements at 10 and 100 MHz have yielded greater than 90-percent carrier-to-sideband conversion efficiency with over 100:1 suppression of the carrier and unwanted sideband.

### 2. QUANTUM ELECTRONICS

A single analytical framework for studying the combined effects of signal averaging and crosscorrelation in a dual-laser differential absorption LIDAR system has been developed. The analysis is being used in conjunction with experimental results to evaluate the error-reduction capabilities of this technique of laser remote sensing.

Optical heterodyne spectroscopy has been carried out using GaAlAs diode lasers, directly modulating the injection current at frequencies up to 2.6 GHz. When the modulated laser output probes a narrow absorption line, a characteristic heterodyne beat signal occurs which permits rapid, sensitive measurement of optical absorption and dispersion. Applications include laser remote sensing and frequency locking of diode lasers.

Al<sub>2</sub>O<sub>3</sub> films with useful dielectric properties have been deposited on Si substrates using UV laser-initiated deposition. UV irradiation of the surface during deposition has produced densification of the films.

### 3. MATERIALS RESEARCH

Intentionally doped crystals of InP grown by the liquid-encapsulated Czochralski method contain prominent dopant striations that are probably due to random convection currents caused by large temperature gradients in the melt. By increasing the rate of seed or crucible rotation, the longitudinal variations in dopant concentration have been reduced to a few percent, as determined by measurements of the free-carrier absorption with a scanning CO<sub>2</sub> laser.

A four-terminal device that can be operated either as a lateral npn bipolar transistor or as a conventional n-channel MOSFET has been fabricated in silicon-on-insulator (SOI) films prepared by graphite-strip-heater zone-melting recrystallization. Since bipolar devices have the potential for faster speed than MOSFETs, this initial demonstration that the films are bipolar-device-worthy is a significant step in the development of zone-melting-recrystallized SOI technology for very-large-scale integration (VLSI).

Shallow  $p^+n$  junctions have been formed in n-silicon substrates by implanting  $Si^+$  ions to produce an amorphous layer, implanting low-energy  $B^+$  ions into this layer, then thermally annealing to recrystallize the amorphous material by solid-phase epitaxy. Diodes with junctions only  $\sim 0.25 \mu m$  deep produced by this dual-implantation technique exhibit excellent I-V characteristics. The technique should be useful in the fabrication of short-channel PMOS devices for CMOS circuits.

The electronic structure of four sulfur centers in Si, which have binding energies from 0.109 to 0.612 eV, has been investigated by carrying out a detailed theoretical analysis of earlier data on the infrared absorption of S-doped Si as a function of uniaxial stress. The excited  $np_0$  and  $np_{\pm}$  levels of these centers are well described by the effective mass and deformation potential approximations, while the ground states and low-lying excited levels are considerably perturbed, as expected for moderately deep-lying levels.

The concentration of hole traps in GaAs films grown by molecular-beam epitaxy in the presence of a W flux has been determined by means of capacitance-vs-temperature measurements between 77 and 340°K. The measured trap concentrations, which are in the range from 1 to  $3 \times 10^{14} cm^{-3}$ , are consistent with carrier concentration and mobility data.

#### 4. MICROELECTRONICS

A new optical scheme is described for accurately measuring the gap between two planar surfaces over the range of  $\approx 20$  to  $500 \mu m$ . Although this scheme has general application, it is particularly well suited to the problem of establishing and maintaining the gap between a mask and a substrate in proximity printing lithography systems. The technique has been experimentally implemented, and  $\pm 0.25$ -percent accuracy has been demonstrated over a range of 25 to  $120 \mu m$ .

Monolithic frequency doublers have been fabricated and tested. Planar Schottky-barrier varactor diodes, RF matching circuits, and bias lines are integrated on a  $4 \times 8$ -mm GaAs substrate, demonstrating the feasibility of monolithic frequency multipliers for the first time.

Resonant tunneling has been observed through a single quantum well of GaAs between two barriers of GaAlAs. The current singularity and negative-resistance region are dramatically improved over previous results, and detecting and mixing have been carried out at frequencies as high as 2.5 THz.

#### 5. ANALOG DEVICE TECHNOLOGY

Techniques are being developed to produce very thin silicon substrates for superconductive signal-processing devices by bonding the substrate to a support and using selective etching to reduce its thickness. Other materials including calcium fluoride, quartz, alumina, and sapphire have been examined as possible substrates. Experimental results show that only sapphire and silicon are compatible with high-density superconductive microwave devices, and only silicon is compatible with large time-bandwidth-product devices.

Monitoring and control of fabrication processes have improved the reproducibility and quality of superconductor-insulator-superconductor tunnel junctions. High normal-current densities with uniformities of  $\pm 10$  percent across a wafer and low leakage currents are consistently achieved, which facilitates the production of multiple-junction arrays. The rugged nature of the Nb Nb<sub>2</sub>O<sub>5</sub> Pb structure results in current-density changes of less than 15 percent over a 2.5-year span.

Specific electroacoustic coefficients in LiNbO<sub>3</sub> and LiTaO<sub>3</sub> have been determined by measurement of the velocity change of Z-propagating longitudinal bulk acoustic waves due to a Z-directed electric field. Coefficients of  $4.93 \times 10^{-9}$  cm/V in LiNbO<sub>3</sub> and  $5.55 \times 10^{-9}$  cm/V in LiTaO<sub>3</sub> indicate the feasibility of holographically writing bulk gratings in those materials. A concept is being developed for using such gratings to form a class of acoustic filters similar to surface-wave-reflection-grating devices but operating at higher frequencies.

## REPORTS ON SOLID STATE RESEARCH

15 February through 15 May 1983

### PUBLISHED REPORTS

#### Journal Articles

##### JA No.

- |      |  |   |   |
|------|--|---|---|
| 5357 | A Two Stage Monolithic IF Amplifier Utilizing a Ta <sub>2</sub> O <sub>5</sub> Capacitor                   | A. Chu<br>L.J. Mahoney<br>M.E. Elta<br>W.E. Courtney<br>M.C. Finn<br>W.J. Piacentini<br>J.P. Donnelly | Joint special issue on Monolithic Microwave IC's: IEEE Trans. Microwave Theory Tech. <i>MTT-31</i> , 21 (1983); and IEEE Trans. Electron Devices <i>ED-30</i> , 21 (1983) |
| 5375 | Be-Implanted GaInAsP InP Double Heterojunction Laser Diodes  | J.P. Donnelly<br>J.N. Walpole<br>Z.L. Liao  | IEEE J. Quantum Electron. <i>QE-19</i> , 175 (1983)   |
| 5381 | Reflectometric Spectroscopy of Adsorbed Molecular Layers   | V. Daneu<br>D.J. Ehrlich<br>R.M. Osgood, Jr.*   | Opt. Lett. <i>8</i> , 151 (1983)  |
| 5383 | External Cavity Controlled Operation of a Semiconductor Diode Gain Element in Series with an Optical Fiber | R.H. Rediker<br>R.P. Schloss<br>D. Welford<br>A. Mooradian  | IEEE J. Quantum Electron. <i>QE-19</i> , 433 (1983)   |
| 5387 | Effects of Very Low Growth Rates on GaAs Grown by Molecular Beam Epitaxy at Low Substrate Temperatures     | G.M. Metzger<br>A.R. Calawa   | Appl. Phys. Lett. <i>42</i> , 818 (1983)  |

---

\*Author not at Lincoln Laboratory.



JA No.

- |      |   |   |  |
|------|---|---|--|
| 5391 | Signal Averaging Limitations in Heterodyne- and Direct-Detection Laser Remote Sensing Measurements                | N. Menyuk<br>D.K. Killinger<br>C.R. Menyuk*   | In <i>Optical and Laser Remote Sensing</i> , edited by D.K. Killinger and A. Mooradian (Springer-Verlag, New York, 1983), p. 185 |
| 5392 | Rate of Ethylene Hydrogenation on $\text{Ni}_{1-x}\text{Cu}_x$ Catalysts Effect of Magnetic Ordering              | H.J. Zeiger<br>B. Wasserman*<br>M.S. Dresselhaus*<br>G. Dresselhaus*                      | Surf. Sci. 124, 583 (1983)   |
| 5396 | High Resolution Ion Beam Lithography at Large Gaps Using Stencil Masks  | J.N. Randall<br>D.C. Flanders<br>N.P. Economou<br>J.P. Donnelly<br>E.I. Bromley           | Appl. Phys. Lett. 42, 457 (1983)   |
| 5403 | Experimental Comparison of Heterodyne and Direct Detection for Pulsed Differential Absorption $\text{CO}_2$ Lidar | D.K. Killinger<br>N. Menyuk<br>W.E. DeFeo   | Appl. Opt. 22, 682 (1983)  |
| 5406 | Thin-Film Transistors Fabricated in Solid-Phase-Recrystallized Si Films on Fused Silica Substrates                | B-Y. Tsaur<br>J.C.C. Fan<br>G.W. Turner<br>M.W. Geis<br>D.J. Silversmith<br>R.W. Mountain | J. Appl. Phys. 54, 1151 (1983)   |
| 5409 | Remote Sensing of Hydrazine Compounds Using a Dual Mini-TEA $\text{CO}_2$ Laser DIAL System                       | N. Menyuk<br>D.K. Killinger<br>W.E. DeFeo   | In <i>Optical and Laser Remote Sensing</i> , edited by D.K. Killinger and A. Mooradian (Springer-Verlag, New York, 1983), p. 17  |
| 5410 | Progress in Laser Sources for Remote Sensing  | A. Mooradian<br>P.F. Moulton<br>N. Menyuk   | In <i>Optical and Laser Remote Sensing</i> , edited by D.K. Killinger and A. Mooradian (Springer-Verlag, New York, 1983), p. 257 |

---

\*Author not at Lincoln Laboratory.

JA No.

- |      |   |   |  |
|------|---|---|--|
| 5411 | IR Detectors: Heterodyne and Direct   | D.L. Spears   | <i>In Optical and Laser Remote Sensing</i> , edited by D.K. Killinger and A. Mooradian (Springer-Verlag, New York, 1983), p. 278 |
| 5415 | Q-Switched Semiconductor Diode Lasers   | D.Z. Tsang<br>J.N. Walpole                                  | IEEE J. Quantum Electron. <i>QE-19</i> , 145 (1983)  |
| 5426 | Photodeposition of Ti and Application to Direct Writing of Ti:LiNbO <sub>3</sub> Waveguides   | J.Y. Tsao<br>R.A. Becker<br>D.J. Ehrlich<br>F.J. Leonberger | Appl. Phys. Lett. <i>42</i> , 559 (1983)   |
| 5431 | Broadband Guided-Wave Optical Frequency Translator Using an Electro-Optical Bragg Array       | R.H. Kingston<br>R.A. Becker<br>F.J. Leonberger             | Appl. Phys. Lett. <i>42</i> , 749 (1983)   |
| 5434 | Real-Time Monitoring of CW Mode-Locked Dye-Laser Pulses Using a Rapid-Scanning Autocorrelator | D. Welford<br>B.C. Johnson                                  | Opt. Commun. <i>45</i> , 101 (1983)  |
| 5436 | Diffusion Length of Holes in $\underline{n}$ -InP   | V. Diadiuk<br>S.H. Groves<br>C.A. Armiento<br>C.E. Hurwitz  | Appl. Phys. Lett. <i>42</i> , 892 (1983)   |
| 5439 | Integrated Optics Wave Front Measurement Sensor   | R.H. Rediker<br>T.A. Lind<br>F.J. Leonberger                | Appl. Phys. Lett. <i>42</i> , 647 (1983)   |
| 5443 | Submicrometer Periodicity Gratings as Artificial Anisotropic Dielectrics                      | D.C. Flanders   | Appl. Phys. Lett. <i>42</i> , 492 (1983)   |
| 5453 | 2-Bit 1-GSample/sec Electro-optic Guided-Wave Analog-to-Digital Converter System              | R.A. Becker<br>C.E. Woodward<br>F.J. Leonberger             | Electron. Lett. <i>19</i> , 332 (1983)   |
| 5463 | Integrated Optics: A New Textbook and Thoughts on Future Directions                           | F.J. Leonberger   | Laser Focus <i>19</i> , 98 (1983)  |

## Meeting Speeches

### MS No.

5837A	High Speed Charge-Coupled Device (CCD) Two-Dimensional Correlator	B.E. Burke A.M. Chiang W.H. McGonagle G.R. McCully J.F. Melia	<i>Real Time Signal Processing V</i> , J. Trimble, Ed., Proc. SPIE 341, 159-164 (1982)
5972	Growth and Characterization of Oriented GaAs Bicrystal Layers	J.P. Salerno R.W. McClelland J.C.C. Fan P. Vohl C.O. Bozler	Proc. Sixteenth IEEE Photovoltaic Specialists Conference - 1982, San Diego, California, 28 September - 1 October 1982, pp. 1299-1303
5999	Efficient GaAs Ge Si Solar Cells	B-Y. Tsaur J.C.C. Fan G.W. Turner F.M. Davis R.P. Gale	Proc. Sixteenth IEEE Photovoltaic Specialists Conference - 1982, San Diego, California, 28 September - 1 October 1982, pp. 1143-1148
6002	Junction Formation in GaAs Shallow-Homojunction Solar Cells by the Use of Spin-On Diffusion Sources	G.W. Turner B-Y. Tsaur J.C.C. Fan F.M. Davis R.P. Gale M.K. Connors	Proc. Sixteenth IEEE Photovoltaic Specialists Conference - 1982, San Diego, California, 28 September - 1 October 1982, pp. 1153-1156
6008	Optimal Design of High-Efficiency Tandem Cells	J.C.C. Fan B-Y. Tsaur B.J. Palm	Proc. Sixteenth IEEE Photovoltaic Specialists Conference - 1982, San Diego, California, 28 September - 1 October 1982, pp. 692-701
6012	Solar Photovoltaic Cells	J.C.C. Fan	Proc. First U.S.-China Conf. on Energy, Resources and Environment, Beijing, China, 7-12 November 1982, p. 480

**MS No.**

- |      |  |  |  |
|------|--|--|--|
| 6085 | Lateral Epitaxial Overgrowth of GaAs and GaAlAs by Organometallic Chemical Vapor Deposition  | R.P. Gale<br>R.W. McClelland<br>J.C.C. Fan<br>C.O. Bozler                        | <i>Institute of Physics Conference Series No. 65: Chapter 2</i> (The Institute of Physics, New York, 1983), pp. 101-108  |
| 6095 | RF Magnetron Sputtering of ZnO for SAW: Effects of Magnetic Field Strength and Configuration | A.C. Anderson<br>D.E. Oates  | <i>1982 Ultrasonics Symposium Proceedings</i> (IEEE, New York, 1982), pp. 329-333  |
| 6096 | Adaptive CW Filtering by Chirp Transformation Using Overlap Summation                        | D.R. Arsenault   | <i>1982 Ultrasonics Symposium Proceedings</i> (IEEE, New York, 1982), pp. 180-185  |
| 6097 | Wideband Analog Signal Processing with Superconductive Circuits                              | S.A. Reible  | <i>1982 Ultrasonics Symposium Proceedings</i> (IEEE, New York, 1982), pp. 190-201  |
| 6134 | A 10-MHz CCD Time-Integrating Correlator   | B.E. Burke<br>D.L. Smythe<br>D.J. Silversmith<br>W.H. McGonagle<br>R.W. Mountain | International Solid-State Circuits Conference, New York, NY, 23-25 February 1983, Digest of Technical Papers, p. 256   |
| 6195 | A High-Speed Digitally-Programmable CCD Transversal Filter                                   | A.M. Chiang  | 1983 International Symposium on VLSI Technology, Systems and Applications, Taipei, Taiwan ROC, 30 March - 1 April 1983, Proceedings of Technical Papers, p. 45 |

**UNPUBLISHED REPORTS****Journal Articles****JA No.**

- |      |  |   |                               |
|------|--|---|-------------------------------|
| 5397 | A 2-GHz-Bandwidth Linear-FM Filter Using Superconductive Stripline | J.T. Lynch<br>A.C. Anderson<br>R.S. Withers<br>P.V. Wright<br>S.A. Reible | Accepted by Appl. Phys. Lett. |
|------|--|---|-------------------------------|

JA No.

- |      |  |   |  |
|------|--|---|--|
| 5405 | Transmission Electron Microscopy of GaAs Permeable Base Transistor Structures Grown by Vapor Phase Epitaxy                   | B.A. Vojak<br>J.P. Salerno<br>D.C. Flanders<br>G.D. Alley<br>C.O. Bozler<br>K.B. Nichols<br>R.W. McClelland<br>N.P. Economou<br>R.A. Murphy<br>W.T. Lindley<br>G.D. Johnson | Accepted by J. Appl. Phys.               |
| 5417 | A Comparison of Etched-Geometry and Overgrown Silicon Permeable Base Transistors by Two-Dimensional Numerical Simulations    | B.A. Vojak<br>G.D. Alley  | Accepted by IEEE Trans. Electron Devices |
| 5423 | UV-Laser Photopolymerization of Volatile Surface-Adsorbed Methyl Methacrylate  | J.Y. Tsao<br>D.J. Ehrlich   | Accepted by Appl. Phys. Lett.            |
| 5435 | Developing a Technology Base for Advanced Devices and Circuits   | N.P. Economou   | Accepted by Proc. IEEE                   |
| 5437 | Three-Guide Optical Couplers in GaAs   | J.P. Donnelly<br>N.L. DeMeo<br>G.A. Ferrante  | Accepted by IEEE J. Lightwave Technology |
| 5445 | Fourier Transformation Using an Electroabsorptive CCD Spatial Light Modulator  | R.H. Kingston<br>F.J. Leonberger  | Accepted by IEEE J. Quantum Electron.    |
| 5469 | Comparison of Guided-Wave Interferometric Modulators Fabricated on LiNbO <sub>3</sub> via Ti Indiffusion and Proton Exchange | R.A. Becker   | Accepted by Appl. Phys. Lett.            |

**JA No.**

- |      |   |   |                                  |
|------|---|---|----------------------------------|
| 5473 | Impact Ionization in (100)-<br>and (111)-Oriented InP Ava-<br>lanche Photodiodes                        | C.A. Armiento<br>S.H. Groves  | Accepted by Appl. Phys.<br>Lett. |
| 5474 | Effect of Magnetic Transition<br>on the H-D Exchange Reaction<br>on $\text{Ni}_{1-x}\text{Cu}_x$ Alloys | H.J. Zeiger<br>B. Wasserman*<br>M.S. Dresselhaus*<br>G. Dresselhaus*                  | Accepted by Phys. Rev. B         |
| 5475 | Graphite-Heater Zone-Melting<br>Recrystallization of Si Films   | J.C.C. Fan<br>B-Y. Tsaur<br>M.W. Geis   | Accepted by J. Cryst.<br>Growth  |
| 5478 | Surface Photoacoustic Wave<br>Spectroscopy of Thin Films  | S.R.J. Brueck<br>T.F. Deutsch<br>D.E. Oates   | Accepted by Appl. Phys.<br>Lett. |
| 5479 | A Self-Developing Resist with<br>Submicrometer Resolution and<br>Processing Stability                   | M.W. Geis<br>J.N. Randall<br>T.F. Deutsch<br>P.D. DeGraff<br>K.E. Krohn<br>L.A. Stern | Accepted by Appl. Phys.<br>Lett. |
| 5481 | An Assessment of Relative Error<br>Sources on Infrared DIAL Mea-<br>surement Accuracy                   | N. Menyuk<br>D.K. Killinger   | Accepted by Appl. Opt.           |
| 5484 | Laser-Controlled Chemical<br>Etching of Aluminum  | J.Y. Tsao<br>D.J. Ehrlich   | Accepted by Appl. Phys.<br>Lett. |

**Meeting Speeches<sup>†</sup>****MS No.**

- |       |   |              |   |
|-------|---|--------------|---|
| 5264D | Recent Advances in Tunable<br>Lasers and Applications | A. Mooradian | Seminar, Raytheon Research<br>Laboratories, Lexington,<br>Massachusetts, 4 May 1983 |
|-------|---|--------------|---|

\*Author not at Lincoln Laboratory.

†Titles of Meeting Speeches are listed for information only. No copies are available for distribution.

**MS No.**

5960B	Liquid Phase Epitaxy	Z.L. Liao	Lecture, Northeastern University Continuing Education Program, Lexington, Massachusetts, 23 March 1983
6008B	Tandem Solar Cells	J.C.C. Fan B-Y. Tsaur	SPIE Technical Symposium East '83, Arlington, Virginia, 4-8 April 1983
6207	Limitations of Laser Transmission Measurements Due to Correlated Atmospheric Effects	N. Menyuk D.K. Killinger	
6221	Performance Criteria of Components Required for Electrooptic Analog-to-Digital Conversion	R.A. Becker F.J. Leonberger	
6330	Q-Switched Semiconductor Diode Lasers with Integrated Modulators	D.Z. Tsang J.N. Walpole	
6012A	Solar Photovoltaic Cells	J.C.C. Fan	Photovoltaics Seminar, M.I.T., 24-26 March 1983
6085	Lateral Epitaxial Overgrowth of GaAs by Organometallic Chemical Vapor Deposition	R.P. Gale	Seminar, Howard University, Washington, DC, 12 April 1983
6111A	Tunable Paramagnetic-Ion Lasers	P.F. Moulton	American Physical Society Mtg., Los Angeles, 21-25 March 1983
6222	Enhanced Raman Scattering from Crystalline Si Due to Submicrometer Roughness	D.V. Murphy S.R.J. Brueck	
6171B	High-Speed Optoelectronic Signal Processing Device	F.J. Leonberger	IEEE Electron. Device Society Mtg., College Park, Maryland, 10 March 1983
6192	Advances in LEC Growth of InP Crystals	G.W. Iseler	2nd NATO Workshop on Materials Aspects of InP, Lancaster, England, 28-30 March 1983
6206	LPE Growth and Characterization of InP-Based Photodiodes	S.H. Groves M.C. Plonko C.A. Armiento V. Diadiuk	

**MS No.**

6203	The Kinetics of Laser-Surface Microchemistry	J.Y. Tsao D.J. Ehrlich	American Chemical Society Mtg., Seattle, Washington, 20-25 March 1983
6213	Advances in Millimeter and Submillimeter Techniques	P.E. Tannenwald H.R. Fetterman	VIIth International Conference on IR and Millimeter Waves, Marseille, France, 14-18 February 1983
6230	Schottky Diode Mixer Technology for the Millimeter and Submillimeter Wave Regions	B.J. Clifton	
6214A	A Precision Wide-Range Optical Gap Measurement Technique	D.C. Flanders T.M. Lyszczarz	Seminar, Bell Laboratories, Holmdel, New Jersey, 18 February 1983
6284	Submicrometer Periodicity Gratings as Artificial Anisotropic Dielectrics	D.C. Flanders	
6224	Laser Photophysics of Surface-Adsorbed Molecules	D.J. Ehrlich J.Y. Tsao	European Physical Society Mtg., Mauterndorf, Austria, 9-11 March 1983
6244	Characterization of GaAs Permeable Base Transistor Structures by Transmission Electron Microscopy	B.A. Vojak J.P. Salerno A.R. Calawa C.O. Bozler	WOCSEMMAD '83, San Antonio, Texas, 20-22 February 1983
6250	Ultra-Low Temperature Growth of GaAs Using Chlorine Transport Vapor Phase Epitaxy	K.B. Nichols C.O. Bozler S. Rabe	
6249A	High Resolution Lithography for Integrated Circuit Fabrication	N.P. Economou	IEEE Boston Section Mtg., Boston, 16 March 1983
6249B	Developing a Technology Base for Advanced Devices and Circuits	N.P. Economou	Electrical Engineering Seminar, University of Rhode Island, Providence, 25 March 1983
6282	The Electron Beam as a Tool for Testing and Customizing Integrated Circuits	D.C. Shaver	Seminar, Digital Equipment Corporation, Hudson, Massachusetts, 17 March 1983



**MS No.**

6310	Permeable Base Transistor	W.T. Lindley	11th Annual Electronic Materials Symposium, Santa Clara, California, 21-23 March 1983
6315	Heterodyne and Superheterodyne: From Audio to Optical Frequencies	R.H. Kingston	Electrical Engineering Seminar, Washington University, St. Louis, Missouri, 15 March 1983
6320	Microfabrication Techniques: Impact of New Sources	N.P. Economou	Symposium on Novel Sources of Electromagnetic Radiation, Germantown, Pennsylvania, 21-22 April 1983

## ORGANIZATION

### SOLID STATE DIVISION

A.L. McWhorter, *Head*  
I. Melngailis, *Associate Head*  
J.F. Goodwin, *Assistant*  
P.E. Tannenwald, *Senior Staff*

### QUANTUM ELECTRONICS

A. Mooradian, *Leader*  
P.L. Kelley, *Associate Leader*

Barch, W.E.	Johnson, B.C.*
Belanger, L.J.	Killinger, D.K.
Brueck, S.R.J.	Lenth, W.
Burke, J.W.	Lovold, S.H.G.
Bushee, J.F., Jr.	Menyuk, N.
DeFeo, W.E.	Moulton, P.F.
Deutsch, T.F.	Murphy, D.V.
Ehrlich, D.J.	Sedlacek, J.H.C.
Feldman, B.	Sharpe, K.A.
Force, A.	Sullivan, D.J.
Hancock, R.C.	Tsao, J.Y.
Harrison, J.*	

### ELECTRONIC MATERIALS

A.J. Strauss, *Leader*  
J.C.C. Fan, *Assistant Leader*  
J.G. Mavroides, *Senior Staff*  
H.J. Zeiger, *Senior Staff*

Anderson, C.H., Jr.	Kolesar, D.F.
Branz, H.M.*	Krohn, L., Jr.
Button, M.J.	Mastromattei, E.L.
Chapman, R.L.	Metze, G.M.
Chen, C.K.	Nitishin, P.M.
Connors, M.K.	Palm, B.J.
Davis, F.M.	Pantano, J.V.
Delaney, E.J.	Tracy, D.M.
Fahey, R.E.	Tsaur, B-Y.
Finn, M.C.	Turner, G.W.
Gale, R.P.	Vohl, P.
Iseler, G.W.	Windhorn, T.H.
King, B.D.	

### APPLIED PHYSICS

R.C. Williamson, *Leader*  
F.J. Leonberger, *Assistant Leader*  
T.C. Harman, *Senior Staff*  
R.H. Kingston, *Senior Staff*  
R.H. Rediker, *Senior Staff*

Becker, R.A.	Hakimi, F.*	Plonko, M.C.
Carter, F.B.	Hovey, D.L.	Schloss, R.P.*
Chinnoek, C.B.	Johnson, L.M.	Spears, D.L.
Cox, C.H. III	Liau, Z.L.	Tsang, D.Z.
DeMeo, N.L., Jr.	Lind, T.A.	Walpole, J.N.
Diadiuk, V.	McBride, W.F.	Whitaker, N.*
Donnelly, J.P.	Molter-Orr, L.*	Woodhouse, J.D.
Ferrante, G.A.	O'Donnell, F.J.	Yap, D.*
Groves, S.H.	Paladino, A.E.	

---

\*Research Assistant

## ANALOG DEVICE TECHNOLOGY

E. Stern, *Leader*

J.H. Cafarella, *Assistant Leader*

R.W. Ralston, *Assistant Leader*

Anderson, A.C.  
Arsenault, D.R.  
Bouman, C.A.  
Brogan, W.L.  
Dolat, V.S.  
Fischer, J.H.  
Flynn, G.L.  
Gottschalk, P.G.\*

Green, J.B.  
Hauser, E.M.  
Holtham, J.H.  
Kernan, W.C.  
Lattes, A.L.  
Leung, I.<sup>+</sup>  
Macedo, E.M., Jr.  
Macropoulos, W.

Melngailis, J.<sup>+</sup>  
Oates, D.E.  
Reible, S.A.  
Sage, J.P.  
Slattery, R.L.  
Withers, R.S.  
Yao, I.

## MICROELECTRONICS

W.L. Lindley, *Leader*

F.J. Bachner, *Associate Leader*

N.P. Economou, *Assistant Leader*

R.A. Murphy, *Assistant Leader*

Bozler, C.O.  
Bromley, E.L.  
Burke, B.F.  
Cabral, S.M.  
Calawa, A.R.  
Chen, C.L.  
Chiang, A.M.  
Chu, A.  
Clifton, B.J.  
Daniels, P.J.  
Durant, G.L.  
Efremow, N.N., Jr.  
Felton, B.J.  
Flanders, D.C.  
Geis, M.W.

Goodhue, W.D.  
Gray, R.V.  
Hollis, M.A.  
Iax, B.<sup>+</sup>  
Lincoln, G.A., Jr.  
Lyszczarz, I.M.  
Mahoney, L.J.  
Manfra, M.J.  
McClelland, R.W.  
McGonagle, W.H.  
Mountain, R.W.  
Mroczkowski, I.H.  
Nichols, K.B.  
Pang, S.W.

Parker, C.D.  
Peck, D.D.  
Piacentini, W.J.  
Pichler, H.H.  
Rabe, S.  
Randall, J.N.  
Rathman, D.D.  
Shaver, D.C.  
Silversmith, D.J.  
Smythe, D.L., Jr.  
Sollner, I.C.I.G.  
Vera, A.  
Vojak, B.A.  
Wilde, R.F.

---

\*Research Assistant

<sup>+</sup>Part Time

# 1. SOLID STATE DEVICE RESEARCH

## 1.1 2-BIT 1-GSAMPLE/s ELECTROOPTIC GUIDED-WAVE ANALOG-TO-DIGITAL CONVERTER SYSTEM

Previously we reported testing a 2-bit 1-GS/s electrooptic A/D converter, one bit at a time.<sup>1</sup> Here we report on a 2-bit A/D converter operating at a 1-GS/s sampling rate (Fig. 1-1). It consists of a comb-generator-driven GaAlAs diode laser,<sup>2</sup> a LiNbO<sub>3</sub> Ti-indiffused waveguide interferometric modulator array, Si avalanche photodiodes (APDs), wideband dc-coupled amplifiers, and special 1-GHz Si integrated circuits consisting of comparators and 1-to-8 serial-to-parallel converters. The comb-generator-driven diode laser emits <120-ps-wide pulses at a 1000-MHz rate. The optical pulses are endfire coupled to the LiNbO<sub>3</sub> chip (also developed by us, Fig. 1-1), and the optical modulator outputs are imaged on the Si APDs. The Si integrated circuits<sup>3,4</sup> provide the function of comparison and serial-to-parallel conversion so that the data can be slowed to an ECL-compatible rate.

Two interferometric modulators and a reference channel are fed in parallel from a common input via two branching circuits. A dc bias electrode is included for each modulator to allow for adjustment of any imbalance in the interferometers and to allow for the application of a static  $\pi/2$  phase shift to one of the modulators to obtain a Gray-code output. The measured voltage for a  $\pi$ -radian phase shift,  $V_\pi$ , was 3 V. Thus voltages up to  $\pm 3$  V can be converted into a 2-bit digital code.

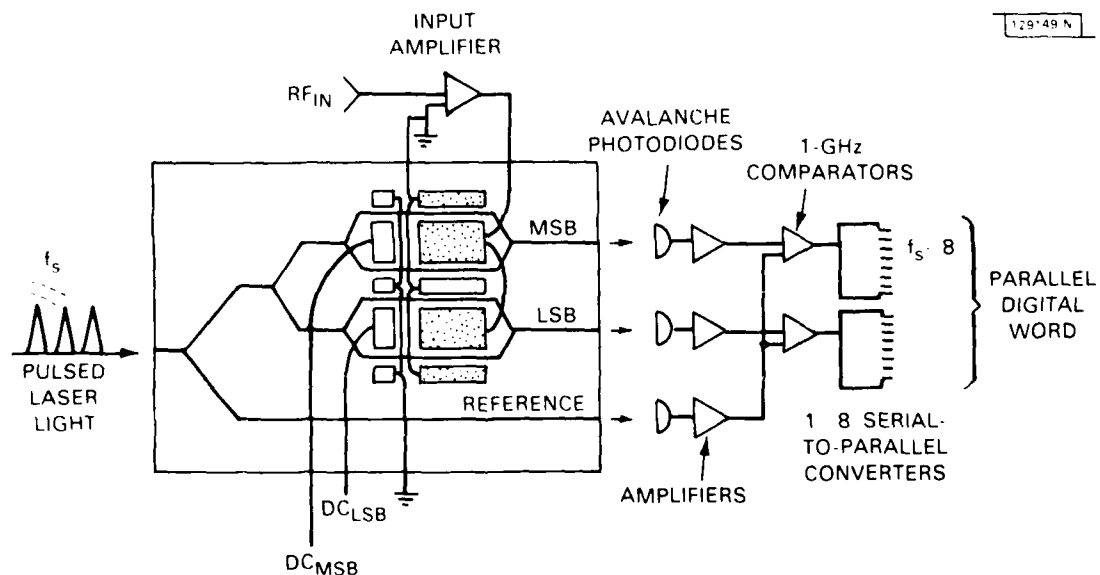


Fig. 1-1. Schematic diagram of guided-wave electrooptic A/D converter.

Outputs of the three detectors (Fig. 1-1) are fed to two 1-GHz comparators. After comparison of the two modulator outputs with that of the reference channel, the outputs are slowed from the 1-GHz rate to a 125-MHz rate using the two 1-to-8 serial-to-parallel converters. The digital outputs, available in a Gray-code format, are next converted to a binary-code format using 125-MHz exclusive-OR circuits. Finally, all 16 outputs and a data-ready signal are available for further digital processing.

In a setup (Fig. 1-2) to test this A/D converter system, selected samples of the A/D converted signal are fed into two 125-MHz D/A converters. This permits reconstruction of slowed A/D converted signals from two different switch-selectable A/D samples simultaneously.

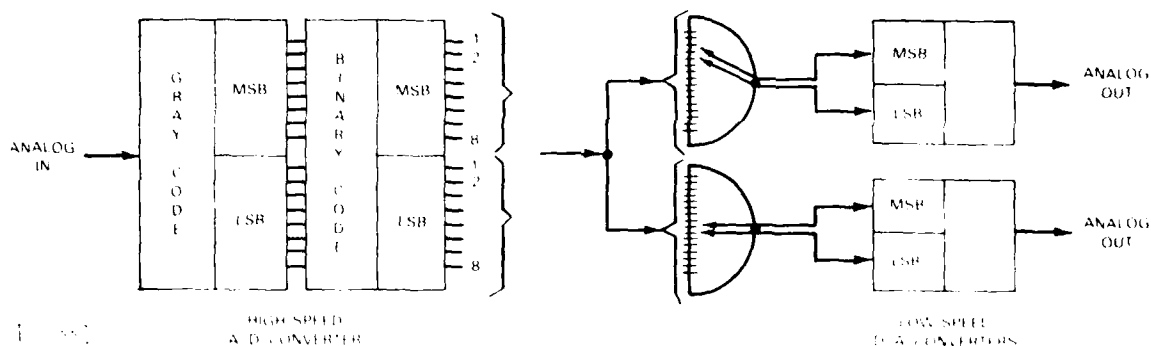


Fig 1-2. Schematic test system for A/D converter. Switches permit simultaneous D/A reconstructions derived from any two samples.

A beat-frequency test was performed to fully test high-frequency capabilities of the A/D converter. This is a standard test used on conventional high-speed A/Ds that permits application of maximum frequency input signals while the device's output is monitored at relatively low frequency.<sup>5</sup> A sinusoidal test signal whose frequency was slightly less than one-half the diode-laser sampling pulse rate was applied. The sampling points step slowly through the sinusoid as a function of time with a rate determined by the beat frequency, and successive sampling points see opposite polarity portions of the sinusoid. Thus, D/A reconstructions from two adjacent sample outputs of the serial-to-parallel converters should be 180 degrees out of phase.

The upper trace (Fig. 1-3) is a 1-MHz signal derived by mixing part of the 6-V peak-to-peak 499-MHz test signal with one-half the 1000-MHz drive signal of the laser. The 1-MHz test signal triggered the oscilloscope. The second and third traces are reconstructed signals derived from two adjacent samples. The two reconstructed signals are 180 degrees out of phase with each other, as expected.

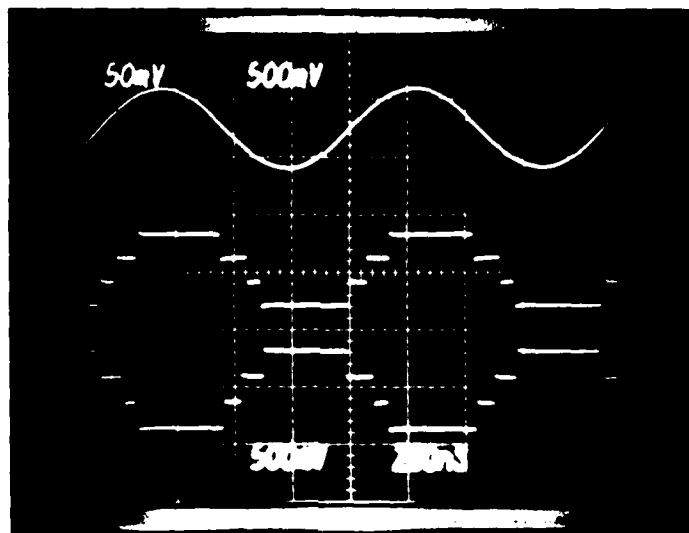


Fig. 1-3. Beat-frequency test of electrooptic A/D converter. The frequency of the input RF test signal is 499 MHz and the sampling rate is 1 GHz. Shown are a derived beat signal (top trace) and reconstructed beat signal from adjacent samples (middle and bottom traces).

Beat-frequency tests were also made using 6-V peak-to-peak sinusoids of 249- and 415-MHz frequencies with sampling rates of 500 and 832 MS s, respectively. The results were identical to those shown in Fig. 1-3. Tests using other adjacent samples produced identical results. The system maintained the same level of performance for all sampling rates. Signal reconstruction demonstrates also that the electrooptic A/D converter system is compatible with other digital processors.

Future work includes increasing the number of bits to four and the sampling rate to 2 GS s.

R.A. Becker  
C.E. Woodward (Group 23)  
E.J. Leonberger

## 1.2 BROADBAND GUIDED-WAVE OPTICAL FREQUENCY TRANSLATOR USING AN ELECTROOPTICAL BRAGG ARRAY

A new type of optical frequency translator has been demonstrated which utilizes Bragg diffraction from a traveling index wave produced by an interdigitated electrode grating on a  $\text{LiNbO}_3$  surface waveguide. The grating is driven by a three-phase electrical signal that results in a unidirectional wave with a fixed Bragg angle determined by the electrode spacing. The diffraction thus produces a single-sideband suppressed carrier optical output. Measurements at 10 and 100 MHz have yielded greater than 90% carrier-to-sideband conversion efficiency with over 100:1 suppression of the carrier and unwanted sideband. The device should be operable from arbitrarily low frequencies up to several gigahertz.<sup>6</sup>

R.H. Kingston  
R.A. Becker  
F.J. Leonberger

## REFERENCES

1. Solid State Research Report, Lincoln Laboratory, M.I.T. (1982:4).
2. C.T. Lin, P.L. Liu, T.C. Damen, D.J. Eilenberger, and R.L. Hartman, *Electron. Lett.* **16**, 600 (1980).
3. J.I. Raffel and S.E. Bernacki, Tech. Dig. IEEE Int. Electron. Dev. Mtg., Washington, DC 601 (1976).
4. K.H. Konkle, S.E. Bernacki, C.E. Woodward, and J.I. Raffel, 1st Gigabit Logic Conf., Orlando, FL (1979).
5. J.R. Naylor, *IEEE Trans. Circuits Syst.* **CAS-25**, 526 (1978).
6. R.H. Kingston, R.A. Becker, and F.J. Leonberger, *Appl. Phys. Lett.* **42**, 759 (1983).

## 2. QUANTUM ELECTRONICS

### 2.1 COMBINED SIGNAL AVERAGING AND CROSS-CORRELATION EFFECTS IN LASER REMOTE SENSING

Previous analyses and experimental results have involved separate investigations of two techniques to reduce the effect of atmospherically induced temporal changes on the accuracy of differential-absorption LIDAR (DIAL) measurements. These studies explored the signal averaging process of the LIDAR returns from each laser individually<sup>1</sup> and the effect of using a dual-laser DIAL system to obtain increased accuracy by exploiting the pulse-pair cross-correlation of the returns from two lasers.<sup>2</sup>

We have now extended the analysis to incorporate both techniques within a single analytical framework which effectively combines the influence of both temporal cross-correlation and signal averaging.

This extended analysis yields a value for the standard deviation of the mean of the LIDAR returns,  $\sigma_{n\xi}$ , given to first order by

$$\sigma_{n\xi}^2 = \sigma_{nx}^2 + \sigma_{ny}^2 - 2\rho_{nc} \sigma_{nx} \sigma_{ny} \quad (1)$$

where  $n$  in the subscript indicates averaging over  $n$  signals;  $\sigma_{nx}$  and  $\sigma_{ny}$  are the standard deviations of the mean of the return LIDAR signals from the two lasers labeled  $x$  and  $y$ , respectively;  $\xi = x/y$  corresponds to the ratio of the returns from the two lasers, and  $\rho_{nc}$  is the temporal cross-correlation coefficient of blocks of  $n$  pulses from lasers  $x$  and  $y$  for a delay time,  $\Delta t$ , equal to the time interval between corresponding pulses of the two lasers. The values of  $\sigma_{nx}$  and  $\sigma_{ny}$  are given by

$$\sigma_{ni} = \frac{\sigma_i}{\sqrt{n}} \left[ 1 + 2 \sum_{j=1}^{n-1} (1 - j/n) \rho_{ji} \right]^{1/2} \quad (i=x,y) \quad (2)$$

where  $\sigma_i$  is the standard deviation for a single pulse of laser  $i$ , and  $\rho_{ji}$  is the temporal autocorrelation coefficient of laser  $i$  for a delay time  $j\tau$ , with  $\tau$  the time interval between pulses.<sup>1</sup> The relationship between  $\rho_{nc}$  and individual pulse-pairs from the same data set is:

$$\rho_{nc} = \frac{\sigma_x \sigma_y}{n \sigma_{nx} \sigma_{ny}} \left[ \rho_c + 2 \sum_{j=1}^{n-1} (1 - j/n) \rho_{jxy} \right] \quad (3)$$

Here  $\rho_{jxy}$  and  $\rho_c$  are the temporal cross-correlation coefficients between pulses separated by a time interval,  $j\tau + \Delta t$  and  $\Delta t$ , respectively. We have set  $\rho_{jxy} = \rho_{-jxy}$  since in our experiments  $\Delta t$  is much shorter than the coherence time of atmospheric turbulence (i.e., the atmosphere may be considered "frozen" during the interval,  $\Delta t$ ). The foregoing equations relate the temporal autocorrelation values,  $\rho_{jx}$  and  $\rho_{jy}$ , and the temporal cross-correlation,  $\rho_{jxy}$ , with the uncertainty in DIAL measurements,  $\sigma_{n\xi}$ .



A preliminary comparison between the above analysis and experimental data has been made using various experimental LIDAR configurations involving both specular and diffusely reflecting targets and both heterodyne- and direct-detection modes. In general, good agreement has been obtained. The results have also pointed up the extreme importance of first averaging the LIDAR returns from each of the lasers individually over the  $n$  pulses prior to taking the ratio of these values. Using the converse approach of ratioing first and then averaging is incorrect and, in some instances, will introduce a large bias in the evaluation of  $\sigma_{ng}$ . Further experimental work is being carried out to establish the limits of validity of the analysis.

N. Menyuk  
D.K. Killinger  
C.R. Menyuk\*

## 2.2 OPTICAL HETERODYNE SPECTROSCOPY WITH FREQUENCY AND AMPLITUDE MODULATED GaAlAs DIODE LASERS

Optical heterodyne spectroscopy using frequency-modulated laser light is a powerful and versatile detection scheme in high-resolution laser spectroscopy.<sup>3,4</sup> In contrast to conventional wavelength modulation spectroscopy this new type of frequency modulation (FM) spectroscopy<sup>3</sup> is characterized by modulation frequencies that are larger than the spectral width of the absorption line being investigated. This results in a large differential absorption experienced by the FM light and, consequently, in a strong heterodyne beat signal that can be detected very rapidly and with very high sensitivity.<sup>4</sup> So far narrowband dye lasers have been used for FM-spectroscopy experiments and the necessary FM had to be produced with the help of external electrooptical phase modulators requiring usually about 1 W of RF drive power. Here we introduce a modified FM measurement technique where the FM spectrum is created by directly modulating the injection current of a single-mode diode laser at frequencies up to several gigahertz.

The above scheme provides a convenient modulation method, but the desired FM is accompanied by an additional amplitude modulation (AM) of the laser output power. However, our investigations demonstrate that GaAlAs diode lasers, which are frequency and amplitude modulated simultaneously, can be very useful light sources for optical heterodyne spectroscopy, and most of the advantages of pure FM spectroscopy are maintained. A RF synthesizer was used to modulate a small fraction of the injection current of a single-mode TJS diode laser at RF frequencies up to 2.6 GHz (Fig. 2-1). The laser frequency,  $\omega_0$ , could be tuned by a current ramp that was controlled by the sawtooth output of an oscilloscope. Figure 2-2 shows Fabry-Perot scans of the laser output when the injection current was modulated at  $\nu_m = 750$  MHz and  $\nu_m = 2.6$  GHz, respectively.

Since only weak current modulation was employed, the light spectrum consists of a strong carrier at  $\omega_0$  and two weak sidebands at  $\omega_0 \pm \omega_m$ ; higher order sidebands were

---

\*University of Maryland, College Park, Maryland.

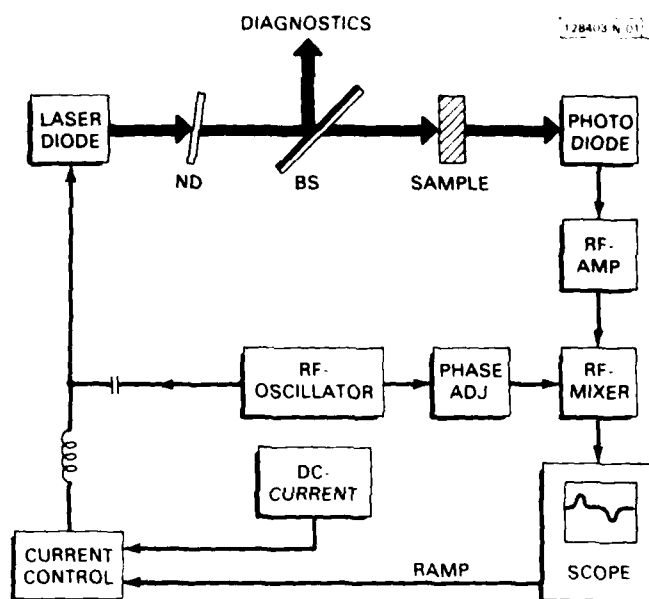


Fig. 2-1. Experimental setup for optical heterodyne spectroscopy with diode lasers.

negligible. The asymmetrical power spectrum observed for  $\nu_m = 750$  MHz is typical for simultaneous FM and AM modulation. The electrical field of the current modulated diode laser can be described by

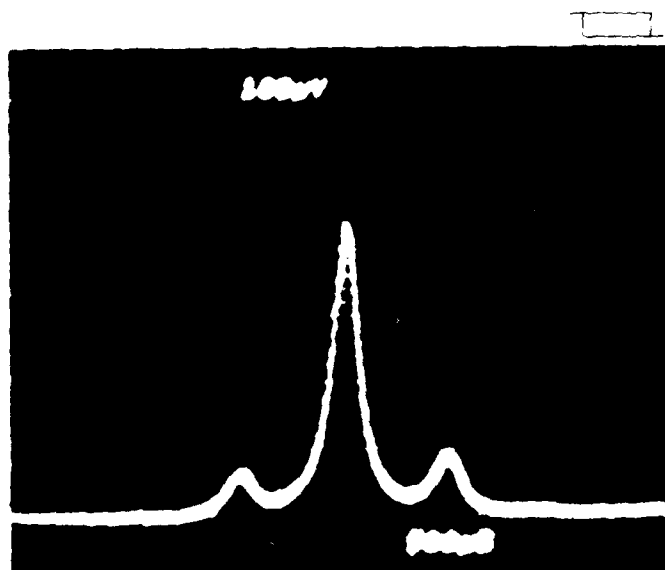
$$E(t) = E_0[1 + M\cos(\omega_m t + \psi)] \exp [i(\omega_0 t + \beta \sin \omega_m t)] \quad (4)$$

where  $\omega_m$  is the modulation frequency,  $M$  is the amplitude modulation index,  $\beta$  is the frequency modulation index, and  $\psi$  defines the phase difference between amplitude and frequency modulation. By expanding Eq. (4) into a series of  $n$ th-order Bessel functions the individual intensities of the carrier and sidebands can be calculated. For  $\beta, M \ll 1$  the following expression for the intensity difference of the two sidebands at  $\omega_0 \pm \omega_m$  is obtained:

$$E^2(\omega_0 + \omega_m) - E^2(\omega_0 - \omega_m) = M\beta \cos \psi \quad (5)$$

The asymmetrical power spectrum in Fig. 2-2a indicates a phase difference of  $0 < |\psi| < \pi/2$  for  $\nu_m = 750$  MHz, whereas at  $\nu_m = 2.6$  GHz (Fig. 2-2b) the sidebands at  $\omega_0 \pm \omega_m$  have equal amplitude, corresponding to  $\psi = \pm\pi/2$ . The phase difference,  $\psi$ , depends critically on the laser operating conditions, which needs further investigation. For  $\nu_m \leq 2$  GHz we have always observed  $|\psi| < \pi/2$ .

(a)



(b)

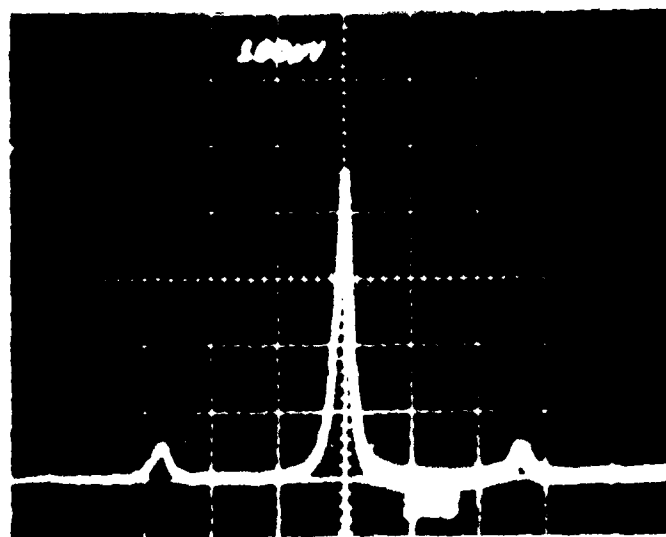


Fig. 2-2. Power spectrum of current-modulated TJS diode laser: (a)  $\nu_m = 750$  MHz; (b)  $\nu_m = 2.6$  GHz.

The heterodyne absorption spectroscopy with the current modulated diode laser was performed with phase-sensitive detection electronics (Fig. 2-1). The laser light probing an absorption line was detected with an avalanche photodiode of at least 3-GHz bandwidth. The photodiode output was amplified with a RF amplifier and then homodyne-detected with a double-balanced mixer. A variable-length air line permitted adjustment of the phase of the local oscillator signal relative to the photodiode signal. The dc output of the mixer was displayed directly on an oscilloscope which through its sawtooth output was synchronized with the laser frequency scan.

In a first set of experiments a Fabry-Perot resonator was used in the reflection mode to simulate an absorption line of 230-MHz width. While the laser frequency was tuned through the resonance, the carrier at  $\omega_0$  and the two sidebands at  $\omega_{\pm 1} = \omega_0 \pm \omega_m$  experienced absorption losses,  $\delta_{0,\pm 1}$ , and phase shifts,  $\phi_{0,\pm 1}$ , which gave rise to a characteristic heterodyne beat signal; i.e., the effect of the sample converts FM into additional AM. We have developed a complete theory for optical heterodyne spectroscopy with frequency- and amplitude-modulated laser light. For  $\beta$ ,  $M \ll 1$  and only weak absorption and dispersion induced by the sample, the final result for the relative laser intensity impinging on the photodetector is

$$I(t) \approx e^{2\delta_0} \left\{ 1 + \cos\omega_m t [\beta(\delta_{-1} - \delta_1) + M(2 + 2\delta_0 - \delta_{-1} - \delta_1)\cos\psi - M(\phi_{-1} - \phi_1)\sin\psi] \right. \\ \left. + \sin\omega_m t [\beta(-2\phi_0 + \phi_{-1} + \phi_1) - M(2 + 2\delta_0 - \delta_{-1} - \delta_1)\sin\psi - M(\phi_{-1} - \phi_1)\cos\psi] \right\} \quad (6)$$

For  $M = 0$ , Eq. (6) reduces to the expression that has been derived for the heterodyne beat signal in the pure FM case.<sup>3</sup> In the special case of  $M = 0$  and  $\omega_m$  small compared with the spectral width of the resonance line, the in-phase part of the spectrum becomes proportional to the first derivative of the absorption, whereas the quadrature part becomes proportional to the second derivative of the dispersion. Additional AM modulation ( $M \neq 0$ ) causes a modification of the line shape of the heterodyne spectrum. Depending on the FM-AM phase difference,  $\psi$ , it also produces a nonvanishing background for either the in-phase ( $\sim \cos\omega_m t$ ) or the quadrature ( $\sim \sin\omega_m t$ ) component of the beat signal. If  $\beta$  and  $M$  are known, a straightforward analysis of the measured heterodyne spectrum permits a determination of the optical absorption and dispersion induced by the sample.

Figure 2-3 shows heterodyne beat signals which were recorded when the AM-FM modulated laser light was tuned through the Fabry-Perot resonance. Appropriate phase adjustment with the variable-length air line permitted selection of either the in-phase or the quadrature part of the signal. Note the characteristic differences in the spectra obtained for  $\nu_m = 750$  MHz and  $\nu_m = 2.6$  GHz. These differences originate from different values,  $\psi$ , for the FM-AM phase relation (compare Fig. 2-2) and are correctly predicted by Eq. (6). The in-phase part of the signal exhibits two dominant structures of opposite polarity (Fig. 2-3a and c) which occur when first the lower frequency sideband and then the higher frequency sideband probes the resonance. Thus, these two spectral features are separated by  $2\nu_m$ . For  $\nu_m = 750$  MHz,  $\psi \neq \pm\pi/2$ , and the in-phase part of the heterodyne signal in Fig. 2-3a shows an additional structure in the center which occurs when the carrier frequency,  $\omega_0$ , sweeps through the resonance. The relative amplitude of this structure is proportional to

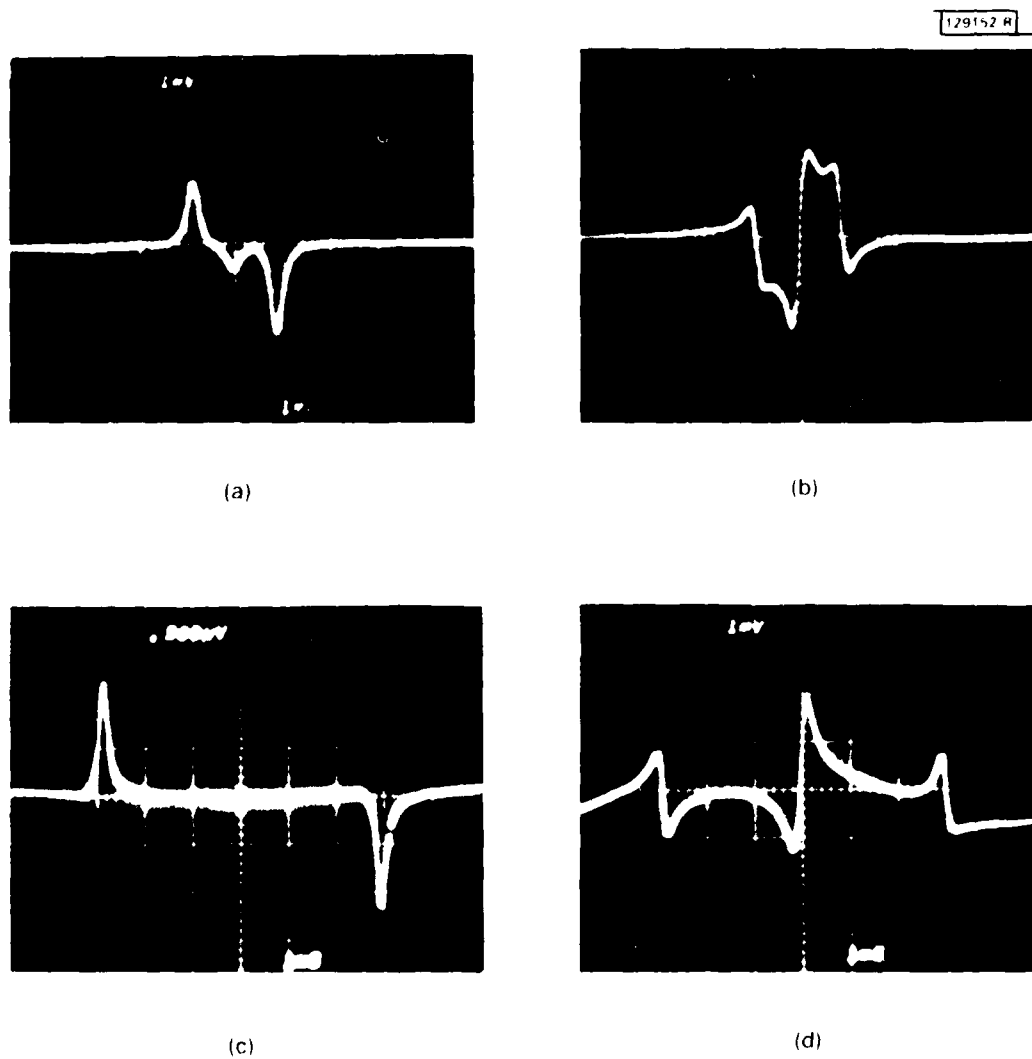


Fig. 2-3. Heterodyne spectrum of Fabry-Perot resonance: (a) in-phase signal,  $\nu_m = 750$  MHz; (b) quadrature signal,  $\nu_m = 750$  MHz; (c) in-phase signal,  $\nu_m = 2.6$  GHz; (d) quadrature signal,  $\nu_m = 2.6$  GHz.

$M\cos\psi$  and is furthermore a function of the absorption,  $\delta$ , of the sample. Since the absorption coefficient and the AM-modulation index  $M$  can be measured independently, the heterodyne spectrum offers the possibility of determining the AM-FM phase relation,  $\psi$ .

We have used the AM-FM modulated TJS diode laser to detect water vapor absorption lines at  $\lambda = 8160\text{-}8180 \text{ \AA}$  by passing the modulated laser light through a 1-m-long absorption cell containing pure water vapor. The measurements benefited from the use of high-modulation frequencies of up to 2.6 GHz exceeding the spectral width of the 1.5-GHz-wide water vapor lines. Therefore, the absorption difference experienced by the individual frequency components of the probing FM-light spectrum was large and, consequently, a strong heterodyne beat signal was generated. In this context it is important to mention that GaAlAs diode lasers have very little frequency and amplitude noise at RF frequencies.<sup>5</sup> Thus, RF heterodyne beat notes can be detected with high sensitivity and in a very short time interval, ultimately limited by the modulation frequency. The quadrature part of the heterodyne signal can be used to lock the carrier frequency to a Fabry-Perot resonance or an atomic absorption line, following a concept which was employed successfully to stabilize the output frequency of ring dye lasers with an accuracy of better than 1 kHz. Important applications of optical heterodyne spectroscopy with AM-FM modulated diode lasers include high-resolution laser spectroscopy, frequency locking of diode lasers and laser remote sensing.

W. Lenth  
W.E. Barch

### 2.3 UV LASER-INITIATED DEPOSITION OF $\text{Al}_2\text{O}_3$

Low-temperature deposition of insulating films is of interest as a technique for semiconductor processing that can reduce wafer warpage and undesired chemical reactions in Si technology and allow greater processing flexibility. The method has potential applications in III-V semiconductor technology, where processing temperatures must be kept low to avoid material dissociation. We have discussed previously the properties of UV-laser-deposited  $\text{Si}_3\text{N}_4$ , whose physical properties were comparable to those of material deposited by low-temperature chemical vapor deposition, but whose dielectric properties were suitable only for passivation applications.<sup>6</sup>

We have now deposited films of  $\text{Al}_2\text{O}_3$ , a material of interest as a dielectric for use with InP as well as with Si, and evaluated its properties. In addition, the effect of UV irradiation of the surface during deposition has been examined.

In the deposition system (Fig. 2-4) a pulsed ArF excimer laser was used to dissociate the reagent gases, trimethyl aluminum (TMA), and  $\text{N}_2\text{O}$ . A 1:50 mix of TMA: $\text{N}_2\text{O}$  was used at a total pressure of 0.5 Torr. Typical laser conditions were average powers of 2 W at a 20-Hz pulse repetition rate. The substrates were heated to temperatures of 200-500°C. Under normal conditions, the laser beam, collimated by a beam-reducing telescope to a slit image about  $3 \times 25 \text{ mm}$ , passed about 1 mm above the substrate. In some experiments, the beam exiting from the deposition chamber was folded back by mirrors and used to irradiate a portion of the substrate. An aperture was used to produce a defined irradiated region, and various attenuators were used to vary the energy striking the surface.

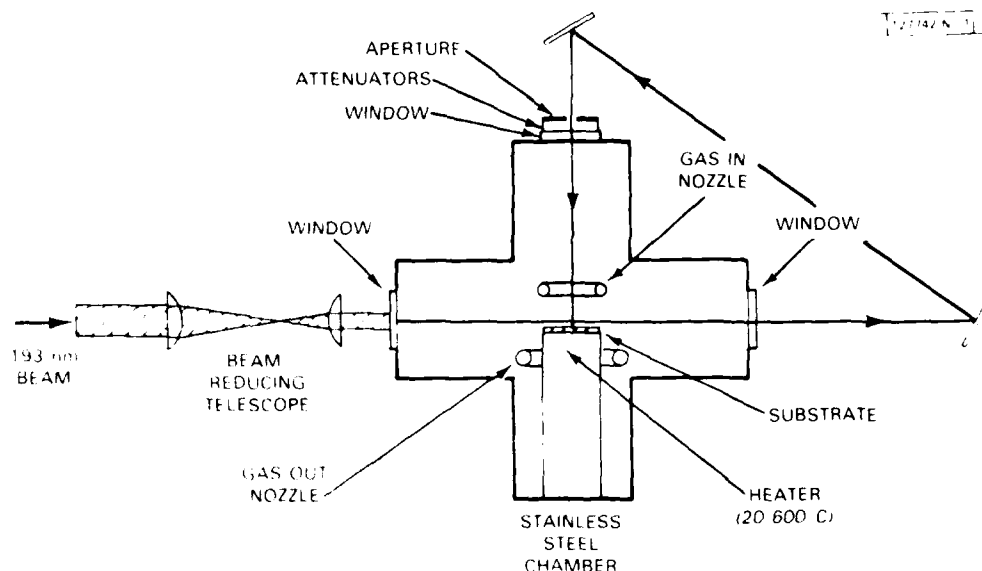


Fig. 2-4. UV laser-induced film deposition system.

The deposited films were examined by ellipsometry, Auger electron spectroscopy (AES), and by capacitance-voltage (C-V) measurements made on films contacted by indium dots. The refractive index of the deposited films, which were 100-200 nm thick, ranged from 1.5-1.7; single crystal  $\text{Al}_2\text{O}_3$  has an index of 1.76, and values of 1.64 are typical of films deposited by other techniques. Composition profiles obtained by AES indicated that the films were stoichiometric to within the accuracy of the technique and uniform in composition; no impurities were detected within the sensitivity of the measurement, approximately 0.1%. C-V measurements on a number of films deposited on Si showed that a number of the films had good dielectric properties, as indicated by small ( $< 1$  V) flat band shifts. By contrast, our earlier  $\text{Si}_3\text{N}_4$  films showed flat band voltage shifts as large as 25 V, indicating a large amount of fixed charge in the dielectric. However, the electrical properties of the films are not yet fully reproducible.

The effect of surface irradiation on the refractive index and thickness of the deposited material is shown in Fig. 2-5. These data were obtained by taking a series of ellipsometer measurements on the deposited film along a line that crosses the irradiated region, which is located approximately at the center of the scan. Even at an energy level of  $0.7 \text{ mJ cm}^{-2}$  [Fig. 2-5 (top)] an increase in the index and a decrease in thickness are found. At  $1.6 \text{ mJ cm}^{-2}$  [Fig. 2-5 (bottom)] the effect is even more dramatic. The energy levels involved here are insufficient to produce a significant heating of the surface; the calculated temperature rise is less than  $10^\circ\text{C}$ . The change in the thickness and index of the deposited material indicates a laser-induced densification of the material. UV irradiation also produced a decrease in the etch rate of the material in  $\text{H}_3\text{PO}_4$  ( $67^\circ\text{C}$ ) by as much as a factor of three

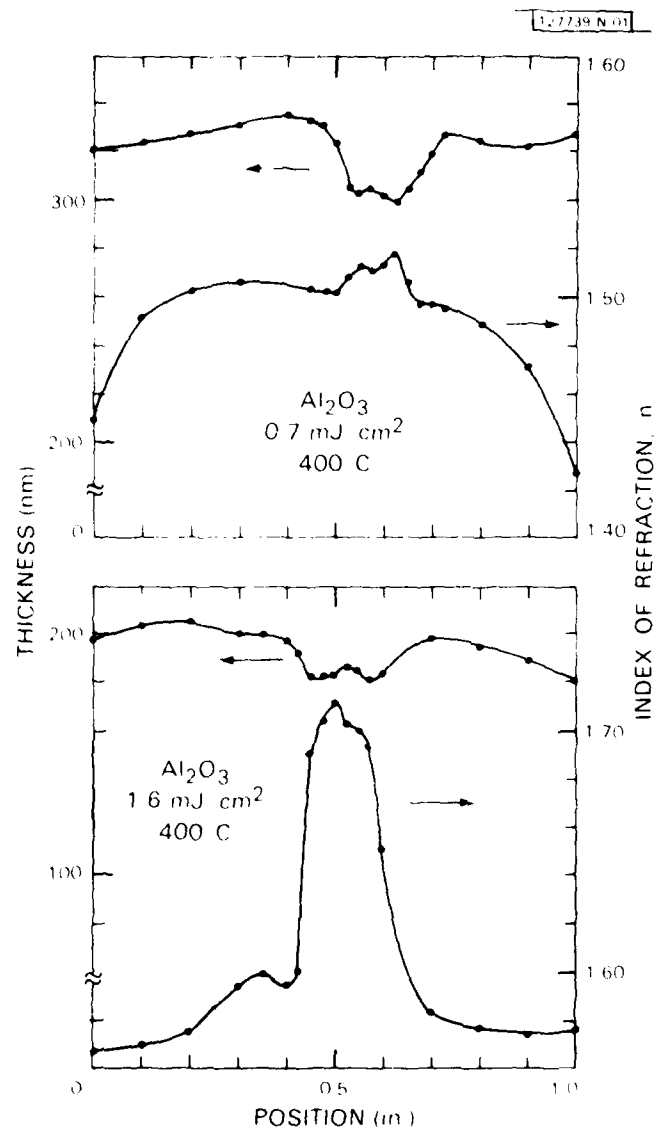


Fig. 2-5. Refractive index and thickness of laser-deposited  $\text{Al}_2\text{O}_3$  films as function of position across film. The central region was irradiated at a 193-nm energy fluence of  $0.7 \text{ mJ} \cdot \text{cm}^{-2}$  (top) and  $1.6 \text{ mJ} \cdot \text{cm}^{-2}$  (bottom). The substrate temperature was  $400^\circ\text{C}$ .



for 400°C material irradiated at 1.6 mJ cm<sup>-2</sup>, also indicating densification. We believe this densification is due to UV-enhanced surface mobility of atoms and molecules on the surface. Such enhancements of surface mobility have a more general and practical significance, since they should make it possible to deposit films at lower temperatures in a variety of deposition systems, including conventional chemical vapor deposition ones.

T.F. Deutsch  
D.J. Silversmith

#### REFERENCES

1. N. Menyuk, D.K. Killinger, and C.R. Menyuk, Appl. Opt. **21**, 3377 (1982); and Solid State Research Report, Lincoln Laboratory, M.I.T. (1982:2), pp. 21-27, DTIC AD-A122252.
2. D.K. Killinger and N. Menyuk, Appl. Phys. Lett. **38**, 968 (1981), DTIC AD-A105374 3; and Solid State Research Report, Lincoln Laboratory, M.I.T. (1981:1), pp. 13-15, DTIC AD-A103887 6.
3. G.C. Bjorklund, Opt. Lett. **5**, 15 (1980).
4. G.C. Bjorklund, W. Lenth, M.D. Levenson, and C. Ortiz, SPIE **298**, 107 (1981).
5. F.G. Walther and J.E. Kaufmann, Optical Fiber Cont., New Orleans, 1983.
6. T.F. Deutsch, D.J. Silversmith, and R.W. Mountain, in *Laser Diagnostics and Photochemical Processing for Semiconductor Devices* (Mat. Res. Soc. Symp. Proc. Vol. 17) R.M. Osgood, S.R.J. Brueck, and H.R. Schlossberg, Eds. (North-Holland, New York, 1983), p. 129.

### 3. MATERIALS RESEARCH

#### 3.1 REDUCTION IN IMPURITY STRIATIONS IN InP CRYSTALS GROWN BY THE LIQUID-ENCAPSULATED CZOCHRALSKI METHOD

The growth of InP crystals by the liquid-encapsulated Czochralski (LEC) method has been described in an earlier report.<sup>1</sup> For most applications the crystals are doped with impurities intentionally, and a uniform distribution of these impurities is desirable. However, by X-ray topography (Fig. 3-1) we have found that crystals grown under our usual experimental conditions contain random striations that are due to abrupt variations in the dopant concentration. These variations probably result from convection currents caused by large temperature gradients in the melt. Many workers have reported dopant striations in Czochralski crystals of various materials.

We are working to reduce the effect of random convection currents by stirring the melt more vigorously to decrease the thickness of the boundary layer at the crystal-melt interface. In initial experiments on n-type crystals heavily doped with Sn, we have reduced the short-range longitudinal variations in dopant concentration to a few percent by increasing the rates of seed or crucible rotation,  $\omega_s$  and  $\omega_c$ , respectively. The magnitude of these variations is found by scanning a focused CO<sub>2</sub> laser along the length of a longitudinal section cut from the crystal and measuring the intensity of the transmitted radiation to determine the optical density. The local dopant concentration is obtained by calculating the absorption coefficient,  $\alpha$ , from the measured optical density, since the absorption at the CO<sub>2</sub> laser wavelength is determined by the room-temperature carrier concentration,  $n_{300}$ , which is essentially equal to the dopant concentration.

In an experiment to investigate the effect of changes in  $\omega_s$ , a crystal of essentially uniform diameter was grown from a Sn-doped melt with  $\omega_c$  fixed at 5 rpm. With the crucible and seed rotations always in the same sense, the value of  $\omega_s$  was initially set at 15 rpm, then increased successively to 25, 40, and 60 rpm. Figure 3-2a is a recorder trace of the optical density of a longitudinal section of the crystal as a function of distance from the seed end. The ordinate scale at the left side of the figure gives the values of  $\alpha$  corresponding to the measured optical densities, while the ordinate scale at the right side gives the values of  $n_{300}$  obtained by using the  $\alpha$  vs.  $n_{300}$  data of Walukiewicz *et al.*<sup>2</sup> In Sec. I the maximum and minimum values of  $n_{300}$  differed by more than a factor of two. In Sec. II, where  $\omega_s$  was increased to 25 rpm, the fluctuations in  $n_{300}$  decreased dramatically. (This change is shown in more detail in Fig. 3-2b, which shows the results for adjacent portions of Secs. I and II on an expanded distance scale.) Increasing  $\omega_s$  to 40 rpm (Sec. III) caused a further improvement in uniformity. The variation in  $n_{300}$  remained about the same when  $\omega_s$  was increased to 60 rpm (Sec. IV). The short-range variations in  $n_{300}$  were only a few percent in Secs. III and IV, making it possible to observe the systematic increase in  $n_{300}$  due to the segregation of Sn, which has a distribution coefficient of less than one in InP.

Figure 3-3 is a recorder trace showing the results of another rotation experiment. In this plot the range of  $n_{300}$  is about 1-1.2 times that in Fig. 3-2. In Sec. I, where  $\omega_s$  and  $\omega_c$  were, respectively, 15 and 5 rpm in the same sense, the fluctuations in  $n_{300}$  gradually decreased with time. When  $\omega_s$  was increased to 80 rpm (Sec. II), the fluctuations decreased

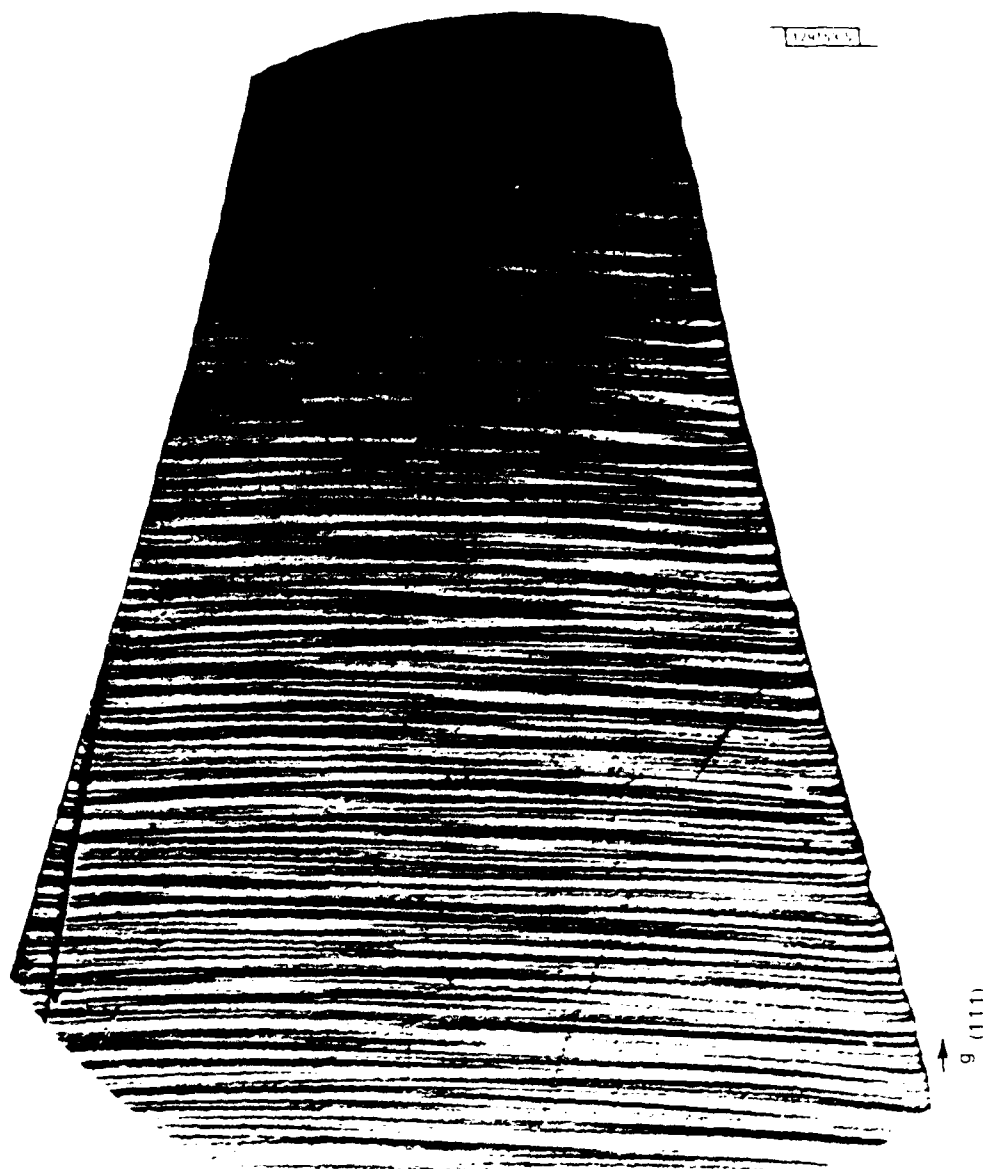


Fig. 3-1. X-ray topograph of (110) longitudinal section from Sn-doped LEC InP crystal.

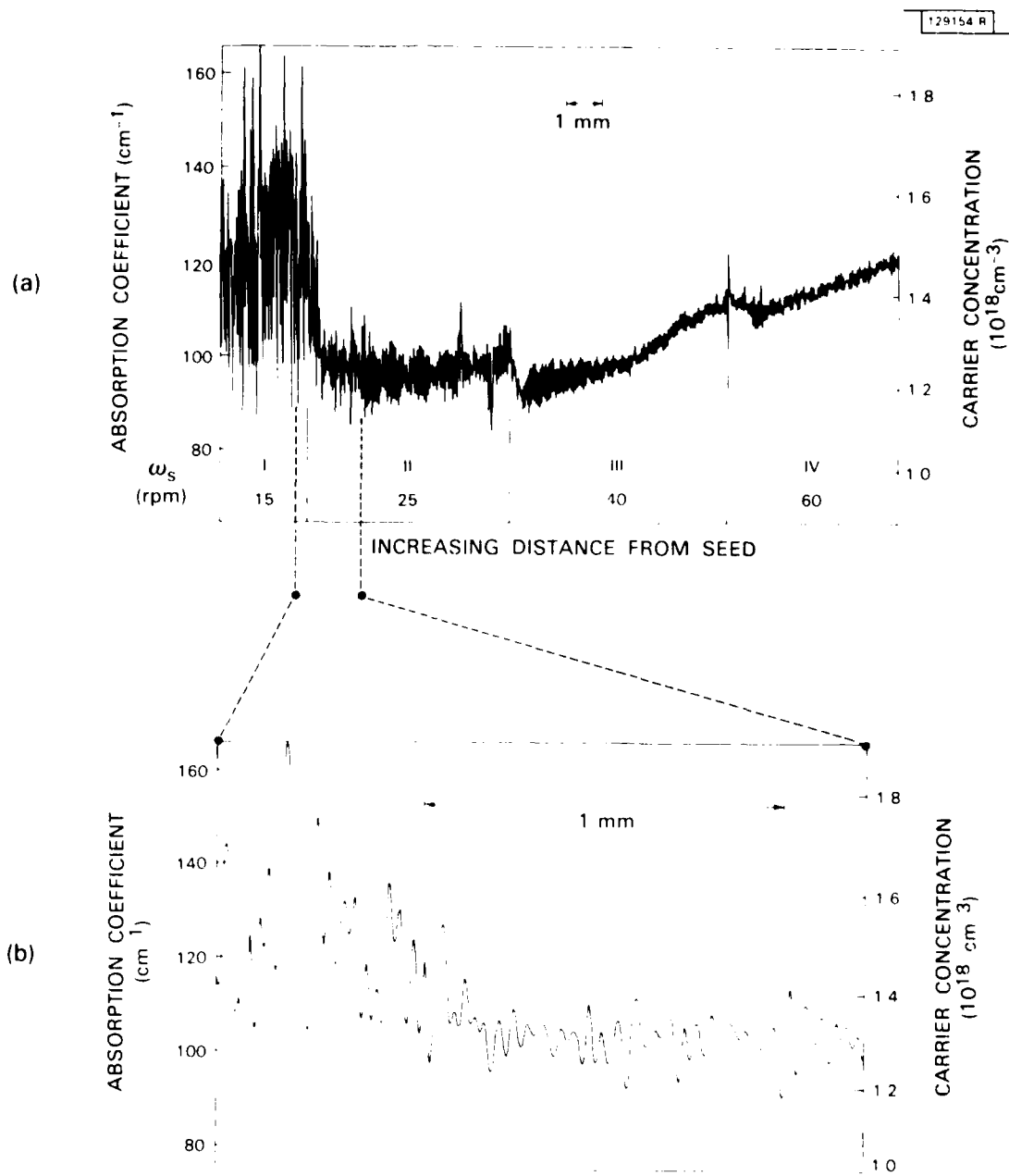


Fig. 3-2. Absorption coefficient at  $10.6 \mu\text{m}$  and carrier concentration vs. distance from seed end of Sn-doped LEC InP crystal.

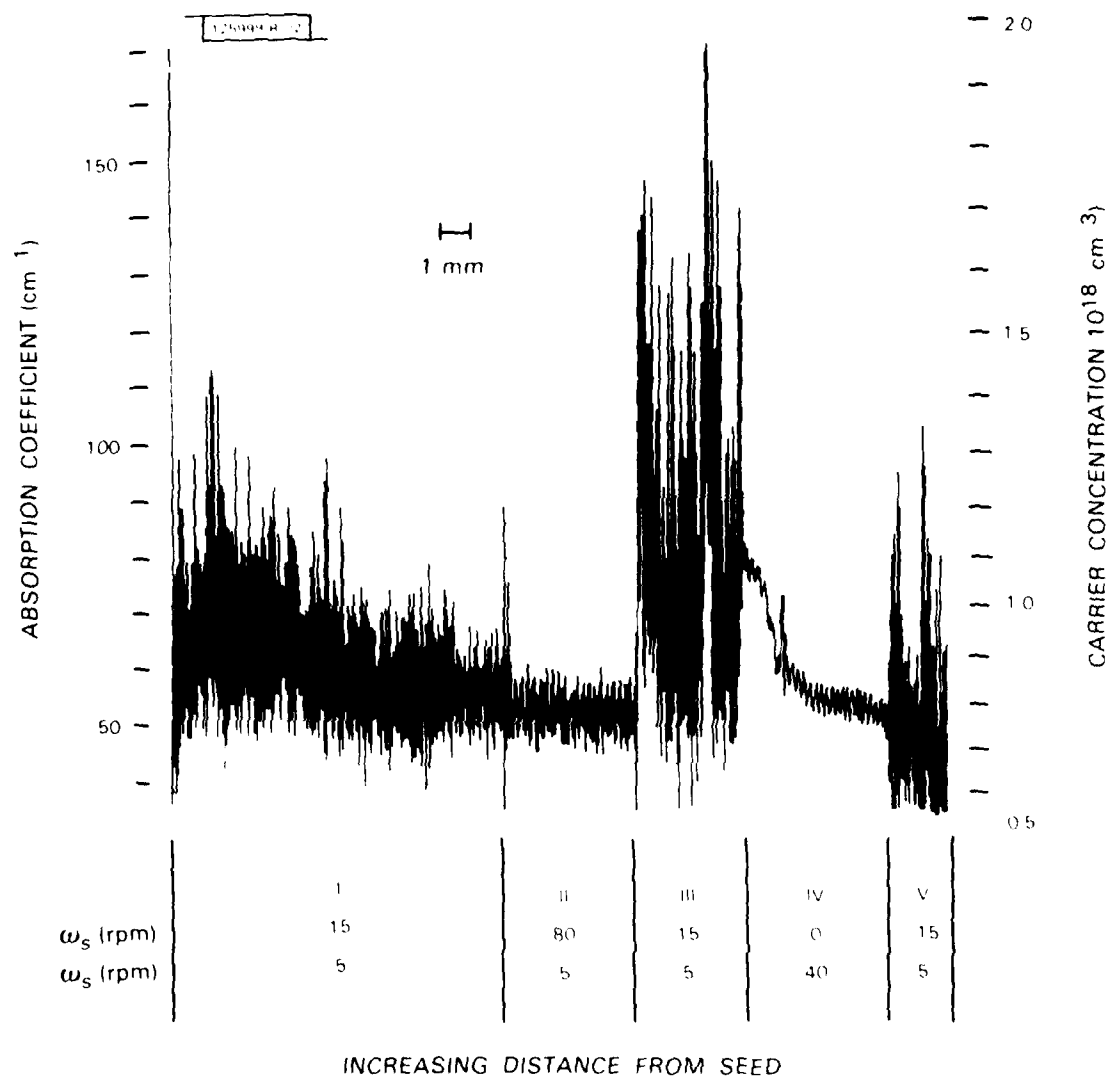


Fig. 3-3. Absorption coefficient at 10.6  $\mu$ m and carrier concentration vs. distance from seed end of Sn-doped LEC crystal.

somewhat, but when  $\omega_s$  was reduced to its initial value of 15 rpm (Sec. III) they became even larger than in Sec. I. Increasing  $\omega_c$  from 5 to 40 rpm while stopping the seed rotation (Sec. IV) caused the fluctuations to decrease strongly. Finally, when  $\omega_c$  was returned to its initial value of 5 rpm and the seed was rotated at 15 rpm in the opposite sense (Sec. V), the magnitude of the fluctuations in  $n_{300}$  became about the same as in Sec. I.

In several other experiments utilizing scanning laser absorption, we have confirmed that the magnitude of random fluctuations in  $n_{300}$  is significantly reduced by increasing  $\omega_s$  above about 25 rpm while keeping  $\omega_c$  at 5 rpm. Furthermore, a crystal grown with  $\omega_c$  of 40 rpm but without seed rotation exhibited short-range variations in  $n_{300}$  of only a few percent over its whole length. Increasing the rate of seed and/or crucible rotation is thus a promising technique to improve the dopant uniformity in LEC crystals of InP.

G.W. Iseler  
M.S. Taylor  
E.J. Delaney

### 3.2 LATERAL BIPOLAR/MOS TRANSISTORS FABRICATED IN ZONE-MELTING-RECRYSTALLIZED Si FILMS ON SiO<sub>2</sub>

In earlier studies<sup>3,4</sup> we have shown that silicon-on-insulator (SOI) films prepared by zone-melting recrystallization using the graphite strip-heater technique<sup>5</sup> are of sufficiently high quality for the fabrication of majority-carrier devices. In addition, pulsed MOS capacitor measurements have indicated<sup>6</sup> that the minority carrier lifetimes in zone-melting-recrystallized films are in the microsecond range, suggesting the possibility of employing these films for bipolar devices. We now report the development of a novel four-terminal device, fabricated in the SOI films by a minor modification of the MOS processing procedure, that can be operated either as a lateral npn bipolar transistor or as a conventional MOSFET. Since bipolar devices have the potential for faster speed than MOSFETs, this initial demonstration that the films are bipolar-device-worthy is a significant step in the development of zone-melting-recrystallized SOI technology for VLSI circuit applications. The performance of the lateral bipolar devices indicates that bipolar transistors with the vertical structure used for conventional bulk bipolar devices could also be fabricated in the SOI films. Utilization of such vertical SOI transistors would be advantageous because they could be fabricated by the techniques that are already well established for the commercial production of bulk devices.

The SOI structures used for device fabrication consist of a 0.5- $\mu$ m-thick recrystallized Si film on a 1- $\mu$ m-thick layer of thermal SiO<sub>2</sub> on a single-crystal Si substrate. Figure 3-4a is a schematic cross section of the device structure. The active area was first defined by LOCOS isolation and doped with B by ion implantation. Gate oxide, 100 nm thick, was grown and a poly-Si film was then deposited and defined to form the gate. A low-dose As<sup>+</sup> implant was performed for collector doping. The emitter and collector contact regions were doped by a high-dose As<sup>+</sup> implant with photoresist used as a mask to protect the collector area. The contact window to the base was then opened and doped with B by ion implantation to reduce contact resistance. After CVD SiO<sub>2</sub> passivation and high-temperature drive-in,

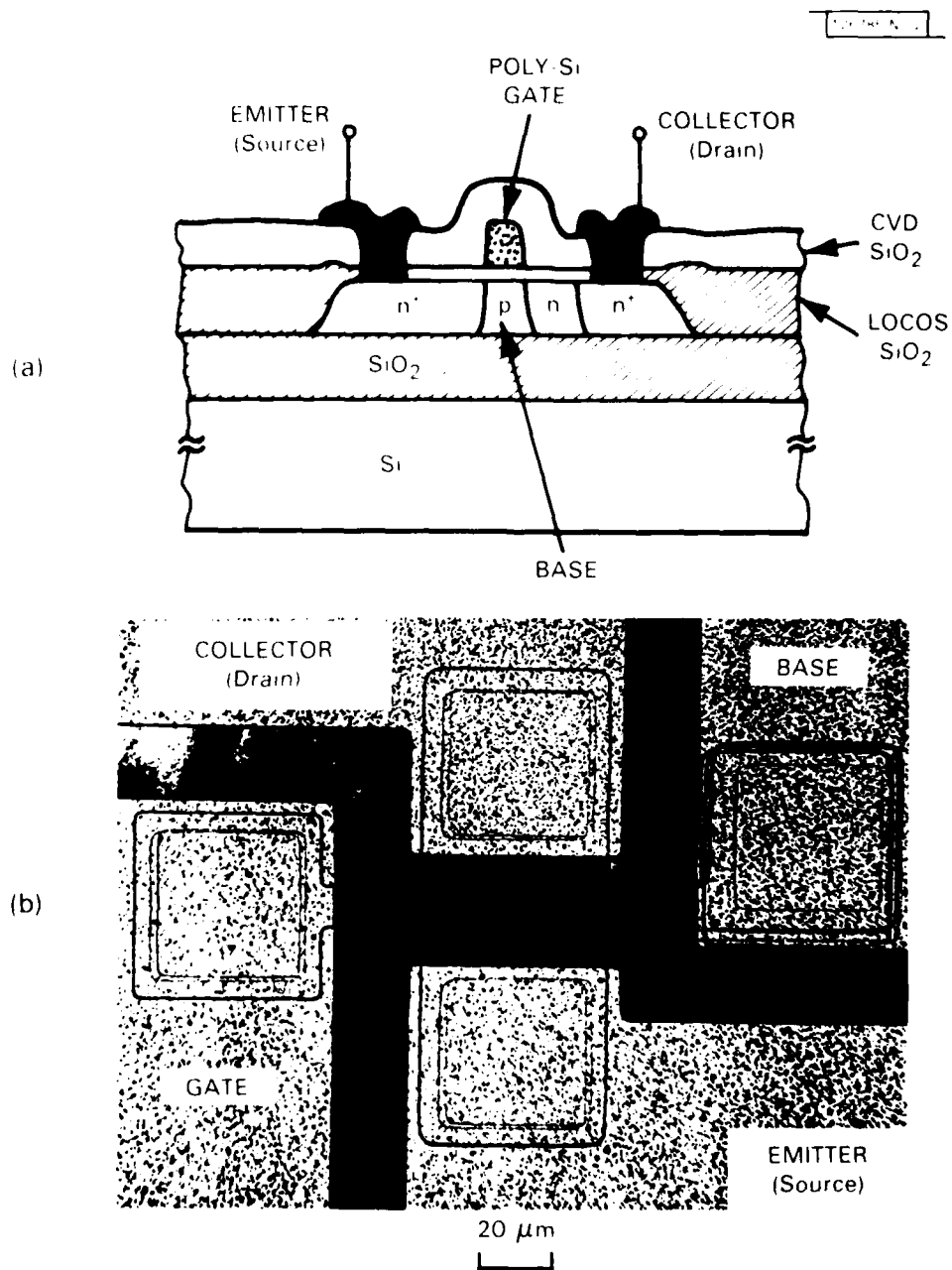


Fig. 3-4. (a) Cross section of lateral bipolar/MOS transistor fabricated in zone-melting-recrystallized Si film, and photomicrograph (top view) (b) of a finished device.

contacts to the emitter (source), base, collector (drain), and gate were opened and metallized with Al. The device was completed by using H<sub>2</sub> sintering to reduce the density of SiO<sub>2</sub>-Si interface states. Figure 3-4b is a photomicrograph of a finished device, which has a nominal gate width (emitter length) of 50  $\mu\text{m}$  and gate length (base width) of 3  $\mu\text{m}$ . The individual devices are fully isolated, making it possible to achieve complete integration of bipolar and MOS devices with minimum interaction between them. This capability could be useful for many digital and analog integrated circuit applications.<sup>7</sup>

Figure 3-5 shows drain-source I-V curves for a typical device operated as an n-channel MOSFET with the base floating and the Si substrate grounded. The device exhibits well-behaved enhancement-mode characteristics with a threshold voltage of +1.3 V. The channel doping concentration ( $\sim 1 \times 10^{17} \text{ cm}^{-3}$ ) is high enough for long-channel characteristics to be retained in spite of the relatively large gate-oxide thickness. In the subthreshold region the drain current is nearly independent of drain voltage with a slope of  $\sim 90 \text{ mV}$  gate voltage per decade of drain current.

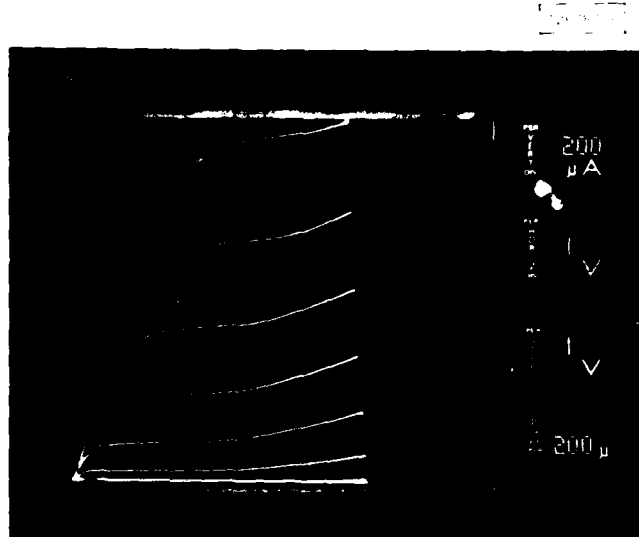


Fig. 3-5. Drain-source I-V characteristics of device operated as n-channel MOSFET with gate voltages of 0-7 V.

The I-V curves in Fig. 3-5 each exhibit a kink in the saturation region, a common property of floating-channel SOI MOSFETs. Kinks may be undesirable for some applications, such as analog circuits, but their effect can be reduced by either connecting the base (or channel) to the source<sup>8</sup> or applying a positive bias to the Si substrate.<sup>9</sup>



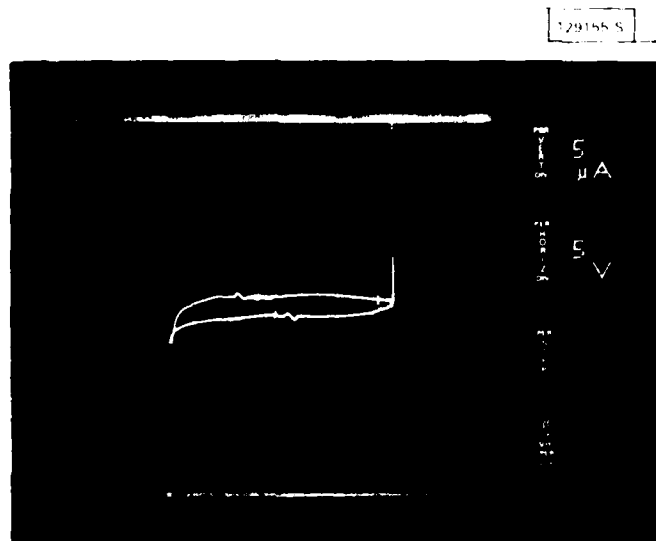


Fig. 3-6. Source-drain (emitter-collector) I-V characteristics of device operated with base and gate contacts floating.

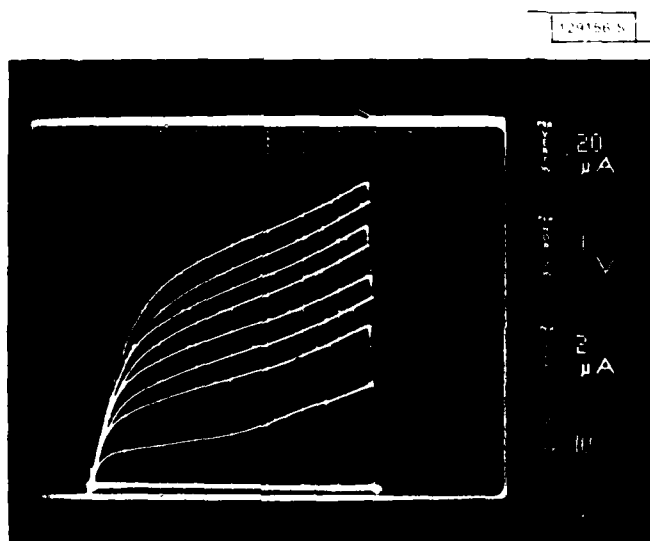


Fig. 3-7. Common-emitter characteristics of device operated as lateral npn bipolar transistor.

Figure 3-6 shows the source-drain (emitter-collector) I-V characteristics obtained for a device with base and gate contacts floating. The drain (collector) junction exhibits sharp breakdown, with the breakdown voltage  $V_B$  exceeding 15 V, compared to 10-15 V for the SOI MOSFETs we have previously fabricated in zone-melting-recrystallized films. The increase in drain  $V_B$  is presumably due to a reduction in impact ionization, which is expected because of the decreased drain doping concentration ( $\sim 1 \times 10^{17} \text{ cm}^{-3}$ ) in the new device. As shown in Fig. 3-6, the source (emitter) junction of the new device exhibits soft breakdown with  $V_B$  exceeding 10 V. The asymmetry in breakdown properties between the emitter and collector junctions is due to the difference in their doping profiles. The emitter-base junction has well-behaved forward I-V characteristics (not shown), which follow the usual linear-log relation with an ideality factor of  $\sim 1.2$ .

Figure 3-7 shows the transistor characteristics obtained for lateral bipolar operation. The common-emitter current gain is  $\sim 18$  at low collector current but falls off rapidly at high current because of current crowding. The gain is relatively high compared to that of conventional bulk lateral bipolar transistors, probably because the complete isolation in the SOI structure eliminates the vertical emitter current that is present in bulk devices, where it is injected into the substrate without contributing to transistor action. The high current gain of the SOI device indicates a good minority-carrier diffusion length in the zone-melting-recrystallized film. The diffusion length calculated<sup>10</sup> for electrons in the base is  $\sim 10 \mu\text{m}$  for the measured current gain of 18 and for a nominal base width of  $3 \mu\text{m}$ . This should be considered as a lower limit since the current gain is reduced by surface recombination at the top and bottom  $\text{SiO}_2$ -Si film interfaces. An increase in current gain should be achieved by reducing the base width and optimizing the base doping.

The fully isolated SOI bipolar transistor, unlike its bulk counterpart, has no parasitic emitter-base and collector-base diodes. Furthermore, the vertical junction arrangement makes it possible to reduce the junction area and therefore the collector depletion capacitance. (For the present device this capacitance is  $0.5 \text{ fF } \mu\text{m}$  emitter length.) Consequently the SOI bipolar transistor should be suitable for high-frequency operation. Its major disadvantage is the high base resistance resulting from the geometric configuration (see Fig. 3-4). Because of current crowding<sup>10</sup> this resistance will limit the current capability, although the problem should be less severe for smaller devices.

B-Y. Tsaur  
D.J. Silversmith

J.C.C. Fan  
R.W. Mountain

### 3.3 DUAL-ION IMPLANTATION TECHNIQUE FOR FORMATION OF SHALLOW $p^+/n$ JUNCTIONS IN SILICON

Complementary metal-oxide-semiconductor (CMOS) technology has recently emerged as an important area for VLSI development, since the low quiescent power dissipation of CMOS devices permits substantially higher packing density. As the lateral dimensions of these devices are reduced to the micrometer or submicrometer range, shallow source and drain p-n junctions must be used to decrease short-channel effects.

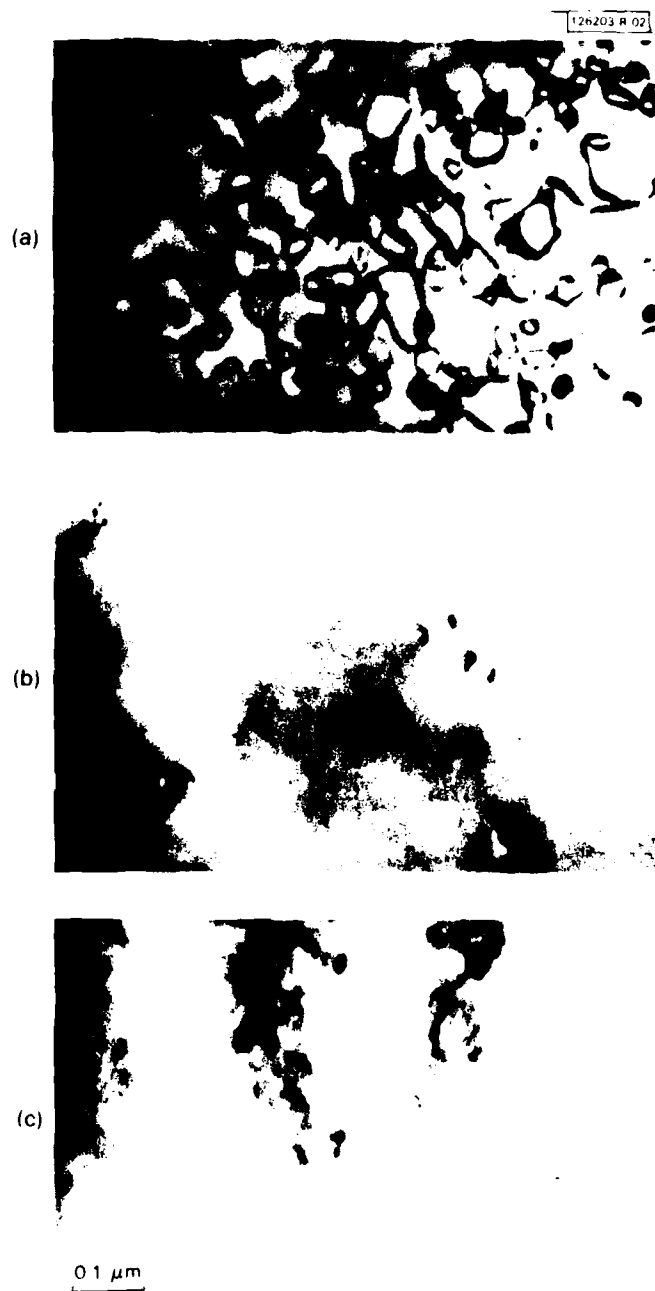


Fig. 3-8. TEM micrographs for annealed Si samples with (a) single  $\text{B}^+$  implant, (b)  $\text{Si}^+$  implant at room temperature followed by  $\text{B}^+$  implant, (c)  $\text{Si}^+$  implant at  $\text{LN}_2$  temperature followed by  $\text{B}^+$  implant.

Shallow  $n^+p$  junctions for n-channel MOS devices are formed conveniently in Si by  $As^+$  ion implantation and subsequent thermal annealing. It is considerably more difficult to form the shallow  $p^+n$  junctions required for the p-channel MOS devices in CMOS circuits. Boron is the acceptor of choice because of its high solid solubility. Because of their small mass, however,  $B^+$  ions with conventional energies penetrate too deeply into Si. The use of low-energy ions to reduce the penetration depth is ineffective since the combination of low mass and energy results in significant ion channeling. Furthermore, because of the high diffusivity of B, in order to prevent a diffusion-induced increase in junction depth it is necessary to limit post-implantation annealing to temperatures and times that are not adequate for complete electrical activation or for fully removing implantation damage.

In several studies<sup>11-13</sup> thin  $p^+$  layers have been formed in Si by the implantation of molecular ions such as  $BF_2^+$ , followed by annealing. Because of their higher mass, these ions have a shorter intrinsic range than  $B^+$  ions, and their penetration is further reduced because implantation produces an amorphous layer. In one of these studies<sup>13</sup> shallow  $p^+n$  junctions with good electrical properties were obtained by post-implantation annealing, but high densities of residual defects were still present.

An alternate approach is to introduce B into Si by the implantation of low-energy  $B^+$  ions, but only after an amorphous layer has been produced by the implantation of  $Si^+$  ions to prevent  $B^+$  channeling. By employing this dual-implantation technique, Tsai and Streetman<sup>4</sup> were able to obtain a  $p^+$  layer with complete B activation, but they did not characterize the junction obtained.

In this investigation we have demonstrated that shallow  $p^+n$  junctions with excellent electrical properties can be produced by the dual-Si B implantation technique, and we have shown by transmission electron microscopy (TEM) that little damage remains after annealing.

Single-implant control samples were prepared by room-temperature implantation of 25-keV  $B^+$  ions to a dose of  $2 \times 10^{15} \text{ cm}^{-2}$  into 1- $\Omega$  cm, As-doped n-Si substrates. To prepare the dual-implant samples, prior to  $B^+$  implantation similar Si substrates were implanted at either room temperature or LN<sub>2</sub> temperature with 100-keV  $Si^+$  ions to a dose of  $10^{15} \text{ cm}^{-2}$ , then with 60-keV  $Si^+$  ions to a dose of  $6 \times 10^{14} \text{ cm}^{-2}$ . All implantations were performed at 7° off normal incidence to minimize channeling. After  $B^+$  implantation all the samples were annealed at  $\sim 600^\circ\text{C}$  for 1 hour and then at  $\sim 900^\circ\text{C}$  for 10 minutes in a quartz tube furnace with flowing Ar H<sub>2</sub> ambient.

For the single-implant control samples, crystal damage due to implantation is relatively light. The implanted layer remains monocrystalline, although it contains isolated defect clusters. In contrast, for dual-implant samples an amorphous layer is present before annealing. The thickness of this layer was found to be  $\sim 0.22 \mu\text{m}$  by etching test samples with dilute HF to selectively remove the amorphous Si and then measuring the height of the etched step with a Dektak.

Because of the difference between the as-implanted structures of the single- and dual-implant samples, there is a great difference in the crystal quality of these samples after annealing, as illustrated by the representative TEM micrographs (Fig. 3-8). Like the single-implant samples, the dual-implant samples are monocrystalline, since annealing results in the

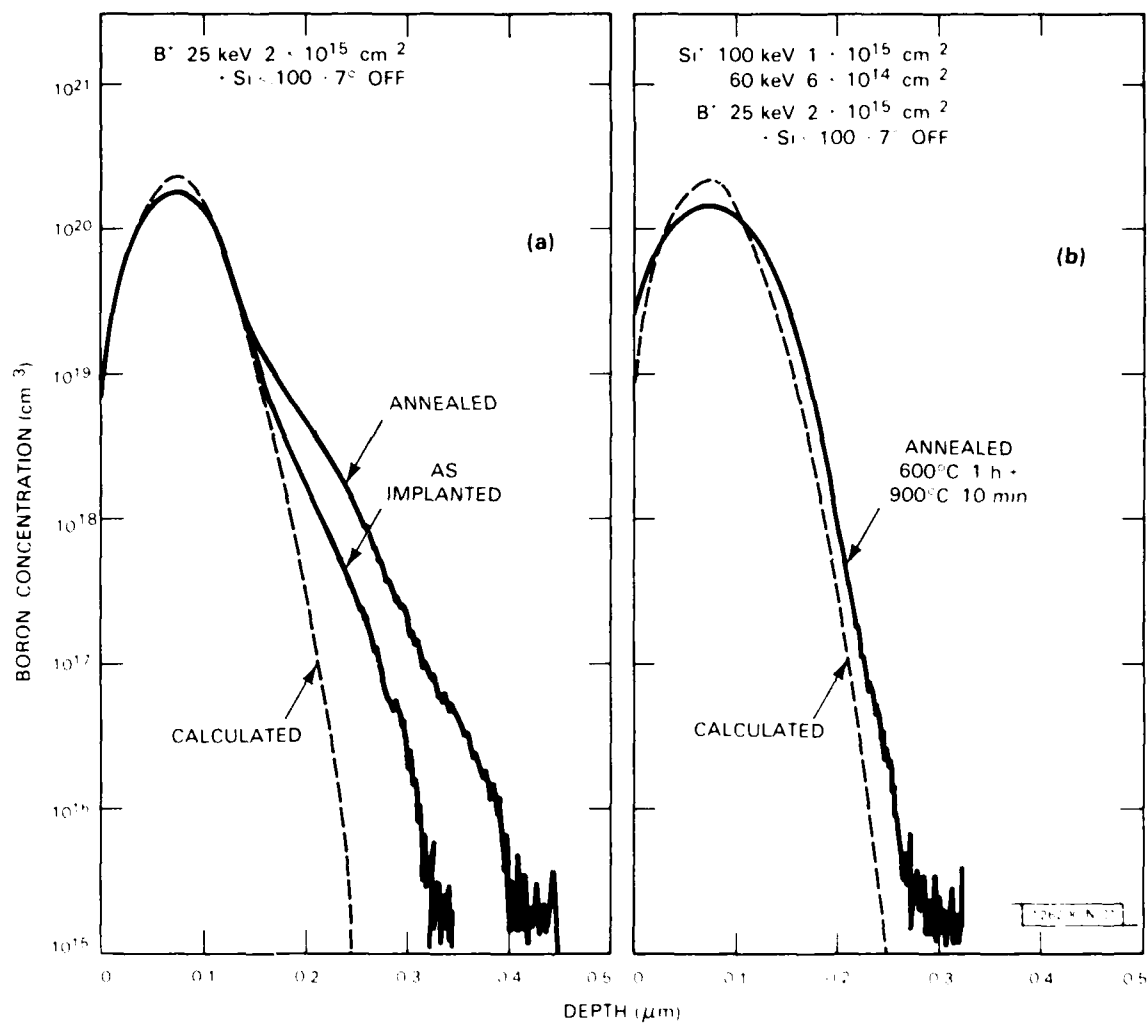


Fig. 3-9. Boron depth profiles obtained by SIMS analysis for samples with (a) single B<sup>+</sup> implant and (b) successive Si<sup>+</sup> and B<sup>+</sup> implants.

recrystallization of the amorphous layers by solid-phase epitaxy nucleated by the underlying crystalline material. However, while the single-implant samples contain a high density of dislocation loops (Fig. 3-8a) the dual-implant samples implanted with Si at room temperature contain only a few dislocation pairs (Fig. 3-8b), and those implanted with Si at LN<sub>2</sub> temperature contain even fewer dislocations (Fig. 3-8c). The crystal quality observed for the dual-implant samples after annealing is typical of Si layers recrystallized by solid-phase epitaxy.

Due to the difference in as-implanted structure between the single- and dual-implant samples, there is a marked difference between their B depth profiles. Profiles determined by secondary ion mass spectrometry (SIMS) for single-implant samples before and after annealing are shown in Fig. 3-9a. From the surface to a depth of 0.15  $\mu\text{m}$ , the as-implanted profile agrees quite well with the profile calculated from published range data.<sup>14</sup> Beyond this depth, however, there is significant tailing due to channeling, which occurred with relatively little interference because the implanted layer was so lightly damaged. Annealing produced an appreciable increase in tailing, so that after annealing the B concentration is equal to the As donor concentration at a depth of  $\sim 0.38 \mu\text{m}$ . The surface concentration of B is  $\sim 1 \times 10^{19} \text{ cm}^{-3}$  both before and after annealing.

The B depth profile measured for a dual-implant sample after annealing is shown in Fig. 3-9b. Since the B<sup>+</sup> ions were implanted into an amorphous layer, tailing is considerably less severe in this case, with the B concentration becoming equal to the As concentration at a depth of only  $\sim 0.25 \mu\text{m}$ . The surface concentration is  $\sim 3 \times 10^{19} \text{ cm}^{-3}$ .

The sheet resistance values measured for the single- and dual-implant samples after annealing differ by a factor of about two. For the latter samples, the sheet resistance is  $\sim 60 \Omega/\square$ , corresponding to nearly complete electrical activation of the implanted B. For the single-implant samples, the value is  $\sim 120 \Omega/\square$ . The increase in resistance is due to incomplete activation and/or a reduction in carrier mobility resulting from scattering by the lattice defects remaining after annealing.

Figure 3-10 shows the I-V characteristics of a typical unpassivated mesa diode, 380  $\mu\text{m}$  in diameter, that was fabricated from a dual-implant sample for which the Si implant was performed at room temperature. Over the current range from  $10^{-11}$  to  $10^{-5} \text{ A}$  the forward characteristic fits the expression  $I = I_0 [\exp(qV/nkT) - 1]$  with  $n = 1.1$ . The near-unity value of  $n$  indicates that the junction is of good quality with current transport dominated by diffusion. The reverse current density is  $\sim 5 \text{ nA cm}^{-2}$  at  $-1 \text{ V}$  and  $\sim 16 \text{ nA cm}^{-2}$  at  $-5 \text{ V}$ . The leakage current is comparable to that of shallow n<sup>+</sup> p junctions formed by As<sup>+</sup> ion implantation.<sup>8</sup>

B-Y. Tsaur  
C.H. Anderson, Jr.

### 3.4 ELECTRONIC STRUCTURE OF DEEP-LYING SULFUR CENTERS IN SI

The understanding and control of impurities that introduce deep-lying states in semiconductors is a matter of great interest because such states can have an important influence on the performance of semiconductor devices. We have investigated the electronic structure of

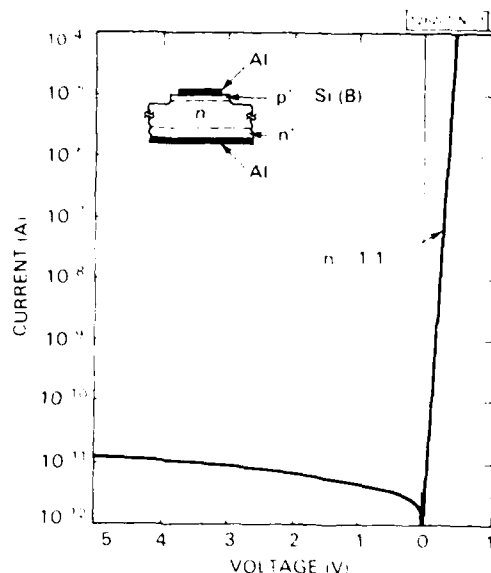


Fig. 3-10. Current-voltage characteristic of diode with shallow  $p^+/n$  junction produced by dual-ion implantation technique.

four deep-lying S centers in Si by carrying out a detailed analysis of earlier data<sup>15</sup> on the infrared absorption of S-doped Si measured at 4 K as a function of uniaxial stress.

The properties of shallow donors and acceptors in Si under uniaxial stress are well described by the effective mass approximation (EMA) and the deformation potential approximation (DPA).<sup>16</sup> The shallow donors have s-like ground states lying about 0.03 eV below the conduction band edge. On the other hand, the four S centers, which we designate as A, B, C, and D, have ground states lying, respectively, 0.1090, 0.1872, 0.3683, and 0.6116 eV below the conduction band edge. Their excited  $np_0$  and  $np_+$  levels are well described by EMA and DPA. Their ground states and low-lying excited states are derived from 1s-like states, but are considerably perturbed, as expected for moderately deep-lying levels. We have used group theoretical arguments to derive expressions giving the energies of these levels as functions of the magnitude and orientation of applied stress. The adjustable parameters in these expressions have been evaluated by fitting the measured infrared spectra. The symmetries inferred for the levels are consistent with the observed selection rules and relative spectral intensities.

The energy levels of the four S centers are shown in Fig. 3-11. The centers are discussed in the order of our decreasing understanding of their electronic structure.

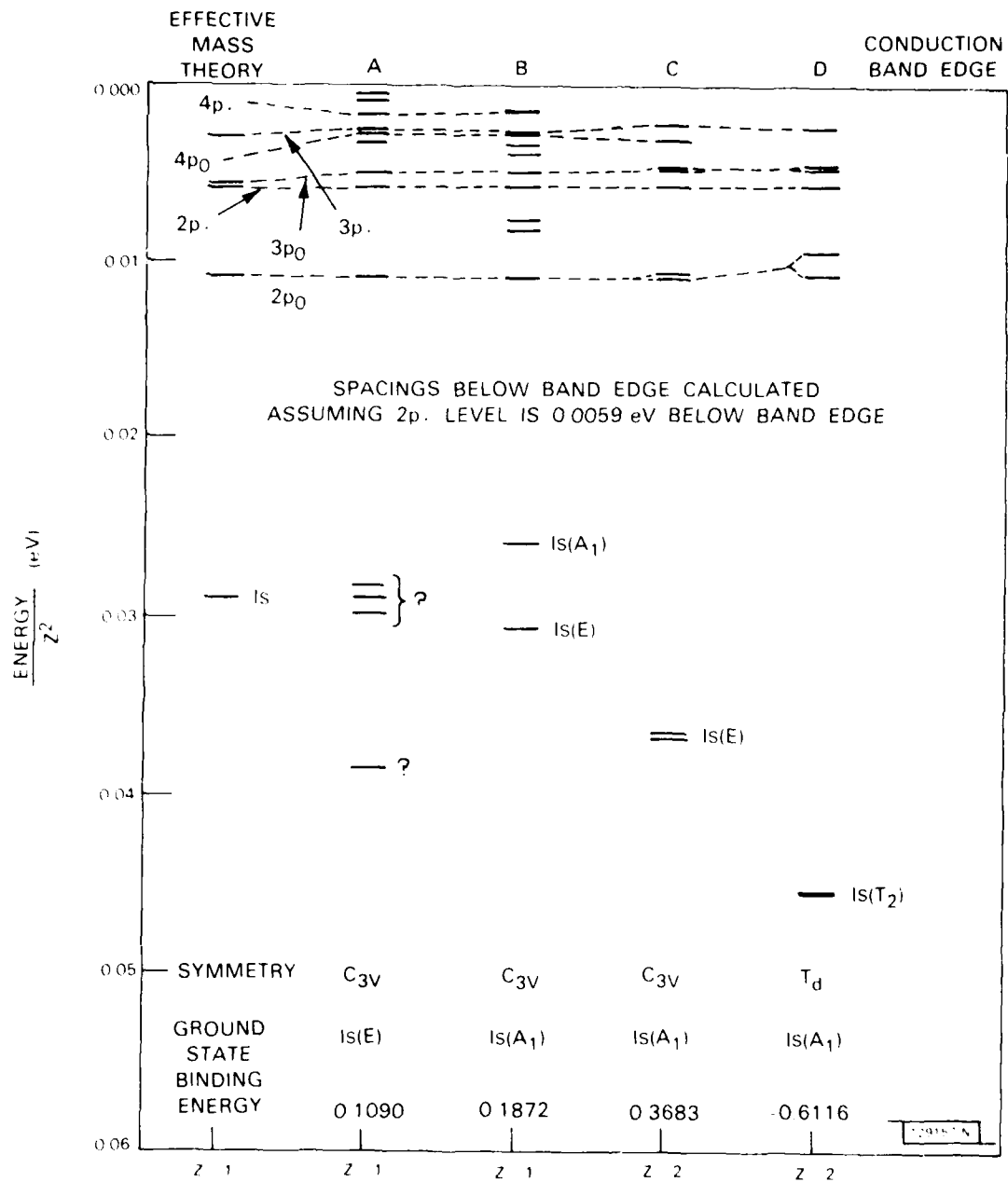


Fig. 3-11. Energy levels of S centers in Si.



**D Center (binding energy 0.6116 eV).** This center has been identified from the infrared spectra<sup>15</sup> and spin-resonance studies<sup>17</sup> as an isolated, probably substitutional, singly ionized sulfur atom ( $S^+$ ) in a site of  $T_d$  symmetry. Because the center is singly ionized, an electron in an excited  $np_0$  or  $np_{\pm}$  state sees an effective core charge of two units. Therefore these levels form a series which is very similar to that for a neutral shallow donor, but their energy spacings below the conduction band edge are four times those of the corresponding levels for the shallow donor. The splitting and polarizations of the  $np_0$  and  $np_{\pm}$  levels under uniaxial stress are consistent with DPA with a pure shear deformation potential,  $E_2 = 8.1$  eV.

The  $np_0$  and  $np_{\pm}$  spectra are consistent with transitions from a  $1s$ -like ground state of  $A_1$  symmetry, designated as  $1s_g(A_1)$ . There is also a spectrum due to weak  $1s_g(A_1) \rightarrow 1s(T_2)$  transitions, where  $1s(T_2)$  is an excited level of  $T_2$  symmetry with threefold orbital degeneracy that is split by spin-orbit interaction. By using the expression derived for the energy of  $1s(T_2)$  level we obtain an excellent description of the stress dependence of the polarization and position of the spectral lines.

**B Center (binding energy 0.1872 eV).** This center has been identified from deep-level transient spectroscopy (DLTS) measurements as a neutral (S-S) pair.<sup>18</sup> The spectra under uniaxial stress are consistent with centers of  $C_{3v}$  (or  $D_{3d}$ ) symmetry with symmetry axes randomly aligned along  $[111]$  crystal axes. The ground state is a  $1s_g(A_1)$  state. The  $np$  levels are EMA-like with DPA stress dependence. The  $1s_g(A_1) \rightarrow np$  spectra yield  $E_2 = 7.8$  eV.

In addition to the  $1s_g(A_1) \rightarrow np$  transitions, we also have identified  $1s_g(A_1) \rightarrow 1s(A_1)$  and  $1s_g(A_1) \rightarrow 1s(E)$  spectra. These are obtained because in  $C_{3v}$  or  $D_{3d}$  symmetry a  $T_2$  state splits into a state of  $A_1$  symmetry and a twofold degenerate state of  $E$  symmetry. For these spectra we obtain a good description of the stress dependence of the polarization as well as a fairly good fit to the stress dependence of the line positions. The fit might be improved by taking into account the interaction between the excited  $A_1$  and  $E$  levels, which are close in energy.

**C Center (binding energy 0.3683 eV).** This center has been identified from combined optical and spin-resonance experiments as the singly ionized B center,  $(S-S)^+$ .<sup>19</sup> The presence of a fair concentration of neighboring charged centers makes the center susceptible to perturbations that produce line broadening and limit the accuracy of the analysis. Like the B center, the C center has  $C_{3v}$  (or  $D_{3d}$ ) symmetry axes aligned randomly along  $[111]$  crystal axes. The ground state has  $A_1$  symmetry, and the  $1s_g(A_1) \rightarrow np$  spectra are helium-like and consistent with transitions to excited  $np$  states, which are EMA-like with DPA stress dependence. The  $1s_g(A_1) \rightarrow np$  spectra again yield  $E_2 = 7.8$  eV.

A number of  $1s_g(A_1) \rightarrow 1s$  lines are observed, most of which are quite weak and may be due to a distribution of local environments produced by clustering of nearby charge centers. The two strongest transitions can be reasonably explained as due to  $1s_g(A_1) \rightarrow 1s(E)$  transitions.

**A Center (binding energy 0.1090 eV).** There is little independent information on the A center in the literature. The ground state  $\rightarrow np$  spectrum at zero stress indicates that the

center is neutral with np levels well described by EMA. The behavior of the ground state — np spectrum is consistent with a center of  $C_{3v}$  (or  $D_{3d}$ ) symmetry, again with a random distribution of [111] symmetry axes. Surprisingly, the stress dependence of the polarization and position of the spectral lines can be explained extremely well on the assumption of a  $1s(E)$  ground state.

A weak spectrum apparently due to  $1s \rightarrow 1s$  is also observed for the A center. However, the behavior of these transitions is unexplained, since the spectrum is not consistent with a  $1s(E)$  ground state, nor is the dependence of the spectrum on stress orientation consistent with an  $A_1$  ground state in  $C_{3v}$  or  $D_{3d}$  symmetry.

H.J. Zeiger

### 3.5 HOLE TRAPS IN TUNGSTEN-DOPED GaAs GROWN BY MOLECULAR BEAM EPITAXY

As a first step in determining whether permeable base transistor (PBT) performance is being degraded by W doping of the GaAs epilayer grown over the W base grid, we are investigating the trapping centers present in Si-doped, n-type GaAs layers grown by molecular beam epitaxy (MBE) in the presence of a W flux from a heated filament. As reported previously,<sup>20</sup> we initially performed DLTS and optical deep-level transient spectroscopy (ODLTS) measurements on Schottky diodes formed by evaporating Au on three such layers. The DLTS technique yields accurate values for both the densities and activation energies of majority carrier traps, but in Schottky diode experiments it does not detect minority carrier traps. Minority traps can be detected by ODLTS, which gives accurate activation energies but generally does not yield reliable density values.

Our DLTS measurements showed no substantial difference in the density of electron traps between the three test layers and a control layer grown without a W flux. In contrast, the ODLTS measurements showed that the test layers contain higher densities than the control layer of hole traps with activation energies of 0.44 and 0.52 eV. However, in calculating the hole trap densities from the ODLTS data it was necessary to make the probably unrealistic assumption that the rate of hole emission from the traps is negligible compared to the rate of electron emission. In order to obtain more accurate density values, we have now measured the small-signal static capacitance of the Schottky barriers as a function of temperature between 77 and 350 K. As the temperature is increased, carriers trapped initially in the depletion region are released, producing a change in the space-charge density. The resulting change in junction capacitance can be used to determine the trap concentration. This technique has the advantage of being applicable to device structures whose geometry makes it difficult to illuminate the barrier region for ODLTS measurements.

Figure 3-12 shows the temperature dependence of the static capacitance measured for sample 3-58 at a dc bias voltage of -0.5 V. With increasing temperature the capacitance decreases, showing that there is a decrease in the positive space charge of the depletion region, as expected from the thermal release of trapped holes. The ODLTS data indicate that this sample, for which the W filament temperature was highest during MBE growth, contains the highest density of hole traps. A representative ODLTS trace for the sample,

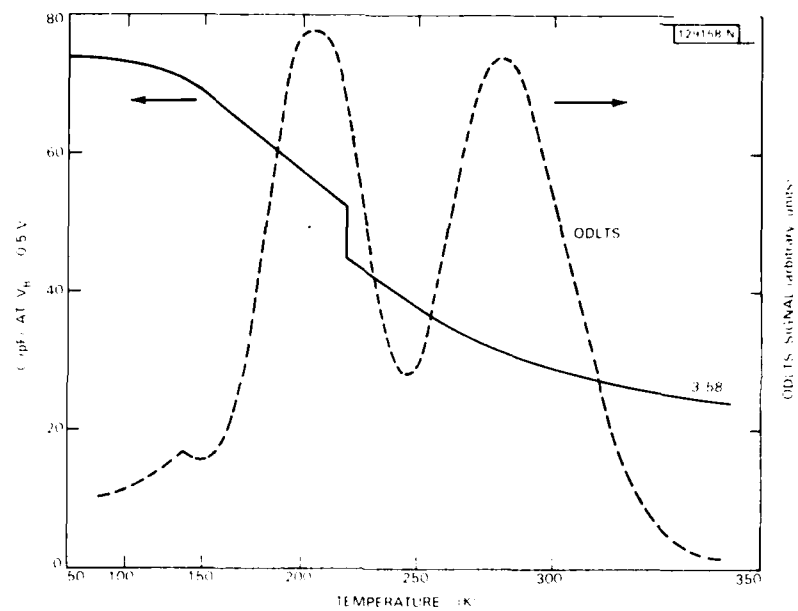


Fig. 3-12. Results of capacitance vs. temperature and ODLTS measurements on a GaAs layer (3-58) grown by MBE in the presence of a W flux.

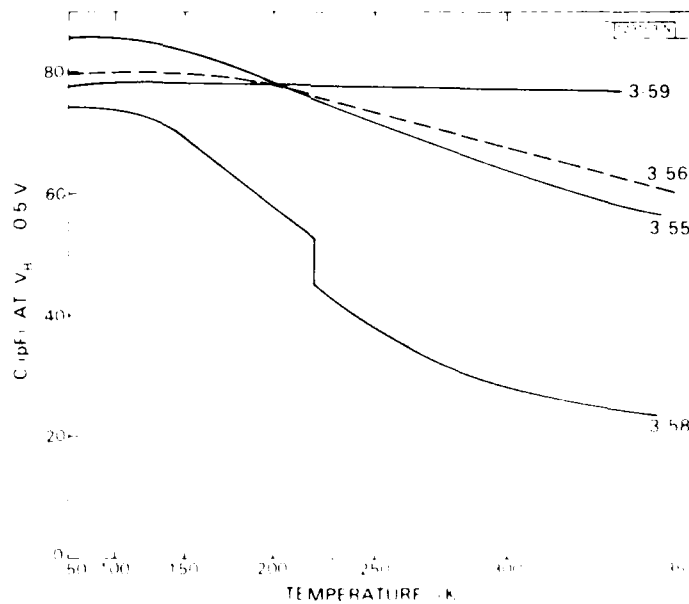


Fig. 3-13. Results of capacitance vs. temperature measurements on GaAs layers (3-55, 3-56, 3-58) grown by MBE in the presence of a W flux and on a control layer (3-59) grown without a W flux.

obtained for an emission time of 100 ms, is also plotted in Fig. 3-12. This trace contains separate peaks due to the two different hole traps. These traps are not resolved by the static capacitance technique; however, there is an abrupt drop in the capacitance curve at about 220 K that may be associated with the temperature dependence of the hole emission rate for the trap responsible for the lower temperature ODLTS peak.

Figure 3-13 shows the capacitance vs. temperature curves for all four samples characterized previously by ODLTS. For the control sample, 3-59, there is no significant change in capacitance between 77 and 350 K. For the three test samples the change in capacitance is correlated with the total area under the two ODLTS peaks. If it is assumed that the capacitance change is due entirely to the release of trapped holes, that the hole traps are filled at 77 K and empty at 350 K, and that the traps are neutral when filled, the density of these traps is given by

$$N_t = (N_D - N_A) \left[ 1 - \left( \frac{C_{350}}{C_{77}} \right)^2 \right] \quad (3-1)$$

where  $C_{77}$  and  $C_{350}$  are the capacitances at the two temperatures. Table 3-1 lists the values of  $N_t$  determined from this expression, as well as the W filament temperature and corresponding W vapor pressure and the values of  $(N_D - N_A)$  and the carrier mobilities measured at 77 K. For the three test samples the  $N_t$  values are in the low  $10^{14} \text{ cm}^{-3}$  range. These values, which are comparable to the values of  $(N_D - N_A)$ , are over an order of magnitude higher than those determined previously from the ODLTS data.

J.G. Mavroides

B.A. Vojak

A.R. Calawa

D.J. Kolesar

TABLE 3-1 GROWTH CONDITIONS AND ELECTRICAL PROPERTIES OF MBE GaAs LAYERS					
Sample	W Filament Temperature (°C)	W Vapor Pressure (Torr)	$(N_D - N_A)$ 77 K ( $\text{cm}^{-3}$ )	$N_t$ ( $\text{cm}^{-3}$ )	$\mu$ at 77 K ( $\text{cm}^2/\text{V-s}$ )
3-55	1800	$1 \times 10^{-11}$	$3.91 \times 10^{14}$	$2.27 \times 10^{14}$	$5.4 \times 10^4$
3-56	2000	$7 \times 10^{-10}$	$3.36 \times 10^{14}$	$1.48 \times 10^{14}$	$6.6 \times 10^4$
3-58	2200	$4 \times 10^{-8}$	$2.83 \times 10^{14}$	$2.58 \times 10^{14}$	$4.4 \times 10^4$
3-59	—	—	$3.66 \times 10^{14}$	—	$5.8 \times 10^4$

## REFERENCES

1. G.W. Iseler, J. Cryst. Growth **54**, 16 (1981), DTIC AD-A107051/5; Solid State Research Report, Lincoln Laboratory, M.I.T. (1980:3), p. 21, DTIC AD-A094075/9.
2. W.D. Walukiewicz, J. Lagowski, L. Jastrzebski, P. Rava, M. Lichtensteiger, C.H. Gatos, and H.C. Gatos, J. Appl. Phys. **51**, 2659 (1980).
3. B-Y. Tsaur, J.C.C. Fan, M.W. Geis, D.J. Silversmith, and R.W. Mountain, IEEE Electron Device Lett. **EDL-3**, 79 (1982).
4. B-Y. Tsaur, J.C.C. Fan, R.L. Chapman, M.W. Geis, D.J. Silversmith, and R.W. Mountain, IEEE Electron Device Lett. **EDL-3**, 398 (1982).
5. M.W. Geis, H.I. Smith, B-Y. Tsaur, J.C.C. Fan, D.J. Silversmith, and R.W. Mountain, J. Electrochem. Soc. **129**, 2812 (1982).
6. B-Y. Tsaur, J.C.C. Fan, and M.W. Geis, Appl. Phys. Lett. **41**, 83 (1982).
7. G. Zimmer, B. Hoefflinger, and J. Schneider, IEEE Trans. Electron Devices **ED-26**, 390 (1979).
8. S.N. Lee, R.A. Kjar, and G. Kinoshita, IEEE Trans. Electron Devices **ED-25**, 971 (1978).
9. M. Akiya and T. Kimura, Electron. Lett. **19**, 36 (1983).
10. A.S. Grove, *Physics and Technology of Semiconductor Devices*, Chap. 7 (Wiley, New York, 1967).
11. D.G. Beanland, Solid-State Electron. **21**, 537 (1978).
12. M.Y. Tsai and B.G. Streetman, J. Appl. Phys. **50**, 183 (1979).
13. W. Fichtner, R.M. Levin, T.T. Sheng, and R.B. Marcus, Electrochemical Society Mtg., Montreal, Canada, May 1982, Extended Abstracts, **82-1**, p. 286.
14. J.F. Gibbons, W.S. Johnson, and S.W. Mylroi, *Projected Range Statistics*, 2nd Edition (Dowden, Hutchinson and Ross, Stroudeborg, PA, 1975).

15. W.E. Krag, W.H. Kleiner, H.J. Zeiger, and S. Fischler, *J. Phys. Soc. Jpn.* **21** (Supp.), 230 (1966), DDC 646490; W.E. Krag, unpublished.
16. W. Kohn, *Solid State Physics*, Vol. 5, F. Seitz and D. Turnbull, Eds. (Academic Press, New York, 1957), p. 257.
17. G.W. Ludwig, *Phys. Rev.* **137**, A1520 (1965).
18. S.D. Brotherton, M.J. King, and G.J. Parker, *J. Appl. Phys.* **52**, 4649 (1981).
19. L. Kravitz and W. Paul, unpublished.
20. Solid State Research Report, Lincoln Laboratory, M.I.T. (1983:1), p. 23.

## 4. MICROELECTRONICS

### 4.1 A PRECISE WIDE-RANGE OPTICAL SCHEME FOR GAP MEASUREMENTS

A new optical scheme to accurately measure the gap between two planar surfaces over the range of  $\approx 20$  to  $500\ \mu\text{m}$  is described. Although this scheme has general application, it is particularly well suited to the problem of establishing and maintaining the gap between a mask and a substrate in proximity printing lithography systems.<sup>1,2</sup> The control of the mask-to-substrate gap is critically important to the feature size and overlay performance of such systems. Furthermore, high-resolution optical techniques to achieve level-to-level pattern registration have demonstrated a sensitivity to gap variations.<sup>3,4</sup>

In the gap measurement scheme (Fig. 4-1) a collimated laser beam with a uniform intensity is focused onto plane 1. Since plane 1 is partially transparent, a portion of the focused beam is reflected and a portion is transmitted. Plane 2 is at least partially reflective. The multiple reflections which occur between planes 1 and 2 produce a multitude of overlapping beams (Fig. 4-2). These beams interfere and produce a characteristic intensity pattern which is converted to an electronic signal by a linear imaging array. The spatial frequency,  $f$ , of this pattern is linearly dependent on the gap between the planes (i.e.,  $d = \alpha f$ , where  $\alpha$  is a system constant determined by the geometry of the configuration).

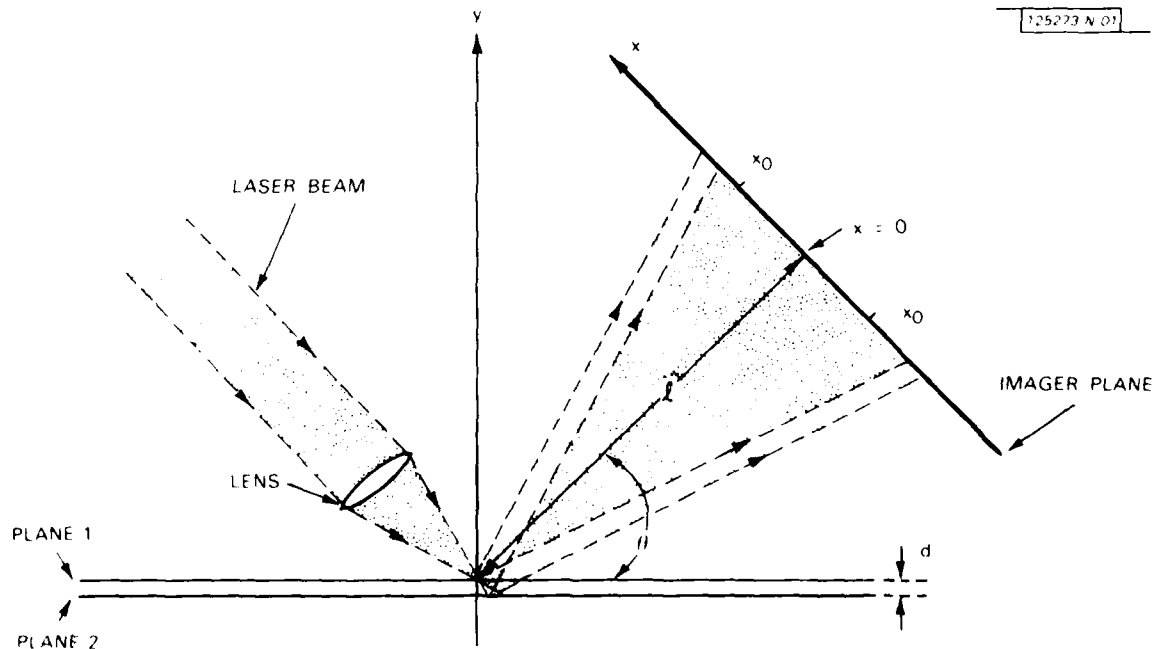


Fig. 4-1. Optical scheme to measure gap between two plane surfaces.

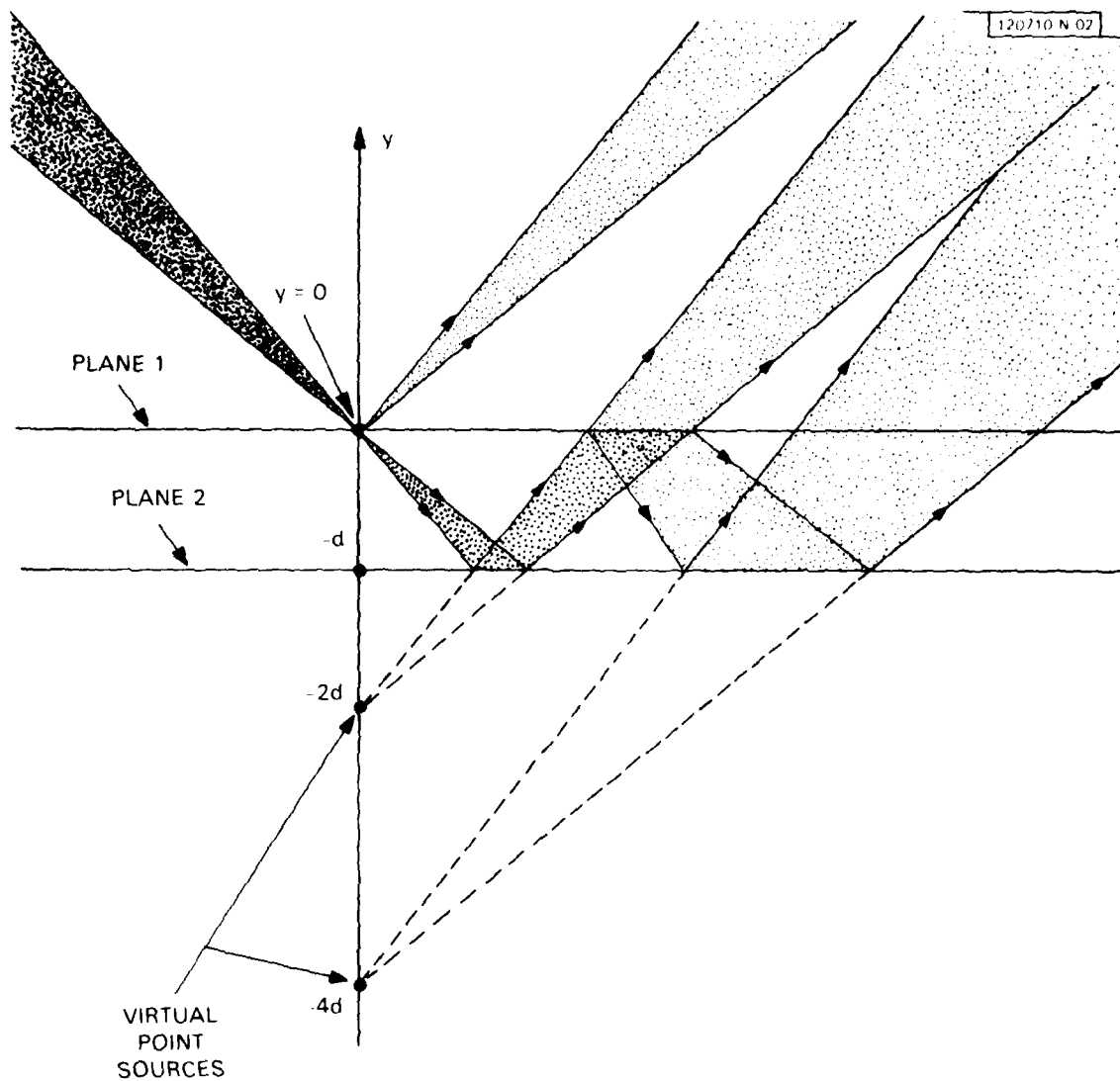


Fig. 4-2. Illustration of the position of virtual point sources which result from multiple reflections between planes 1 and 2.



A very thin (40-nm-thick)  $\text{Si}_3\text{N}_4$ -membrane mask with 5 nm of chromium on the lower surface was used in an experimental test of the gap measurement scheme (Fig. 4-3). This mask structure approximates the zero thickness mask shown as plane 1 in Fig. 4-1. In a practical lithographic system where a thicker and more durable mask is often desirable, an antireflection coating may be required to reduce the effect of reflections from the top surface of the mask. The substrate corresponding to plane 2 consisted of a 1.5-mm-thick glass plate with a highly reflective aluminum layer on the surface facing the mask. Parallelism between mask and substrate was established by observing the pattern of interference fringes in a wide-area laser beam normally incident from the backside of the substrate. Relative displacement between mask and substrate was measured with an accuracy of  $\approx 20$  nm by counting interference fringes using a diode detector (Fig. 4-3). The distance from the focal point on the mask to the center of the imaging array was 50.8 mm, and the angle between the normal to the imaging array and the membrane mask was  $45^\circ$ . A 256-element linear imaging array with a pixel spacing of  $25\ \mu\text{m}$  was used. Imager data were digitized and recorded at a series of gaps spaced at 316.4 nm, as determined from the fringe counting over a gap range of 25 to  $120\ \mu\text{m}$ . Since the laser illumination and imager response vary somewhat with  $x$ , it was found to be necessary to multiply the imager data by a "correction function." The function used was simply the inverse of the imager response with plane 2 removed. Then the "corrected" data were multiplied by a triangular window to reduce the effects of finite array length on the computation. The spatial frequency for each signal was determined by correlating the signals with a sine wave and determining the frequency of the sine wave at which the peak correlation occurred. These data were then fitted to a straight line. The system constant,  $\alpha$ , was determined from the slope of the line, and the deviation of the points from the line was used to compute the system error. In a plot of the absolute gap error vs. gap (Fig. 4-4) it appears that part of the error is due to system noise and that the linear relationship is only approximate.

The accuracy of this gap measurement technique depends on the accuracy with which the system constant is known. The system constant can be determined by the procedure described previously, by measuring a known gap with the system, or by accurately measuring the system geometry and calculating the constant. Calculation of the constant to an accuracy of  $\pm 0.1\%$  would require that the system be assembled or measured with an accuracy of  $\pm 50\ \mu\text{m}$ . This accuracy can be easily obtained by standard machining practice.

D.C. Flanders  
T.M. Lyszczarz

## 4.2 MONOLITHIC FREQUENCY DOUBLERS

We report here fabrication and RF performance data obtained from the first monolithic frequency doubler in which a planar Schottky barrier varactor diode and microstrip circuits are integrated on a GaAs substrate. The intended uses of this monolithic frequency doubler are for integration into a heterodyne receiver to provide local oscillator power, and as the output stage of a transmitter.

The monolithic frequency doubler was designed with the assistance of scaled models. In a 0.63- to 1.26-GHz hybrid prototype (Fig. 4-5) a packaged varactor diode is attached to the input and output matching networks near the center of the circuit. The circuit elements in

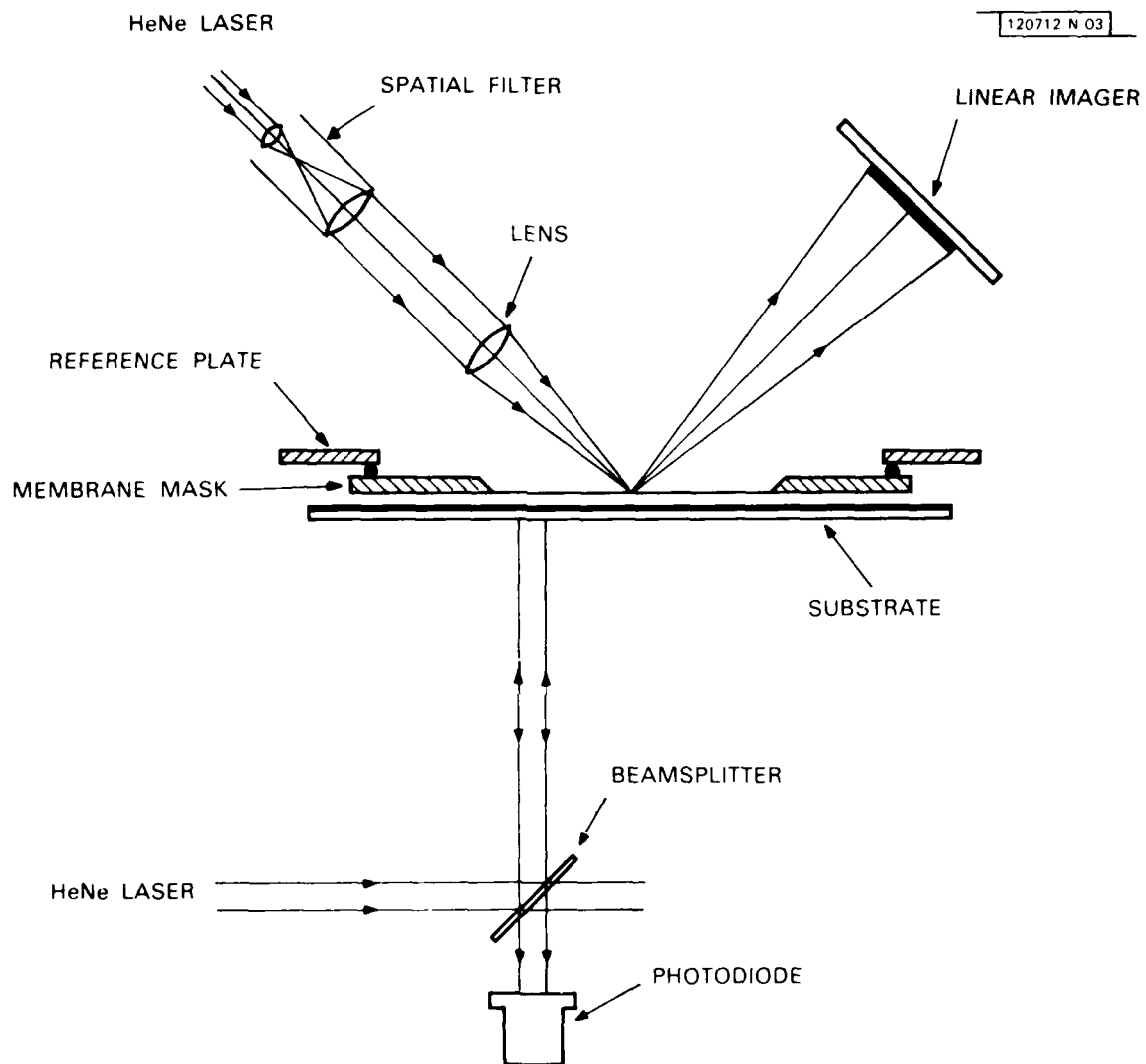


Fig. 4-3. Experimental system to determine accuracy of gap measurement scheme. Auxiliary interferometer measures relative motion of mask and substrate with high accuracy.

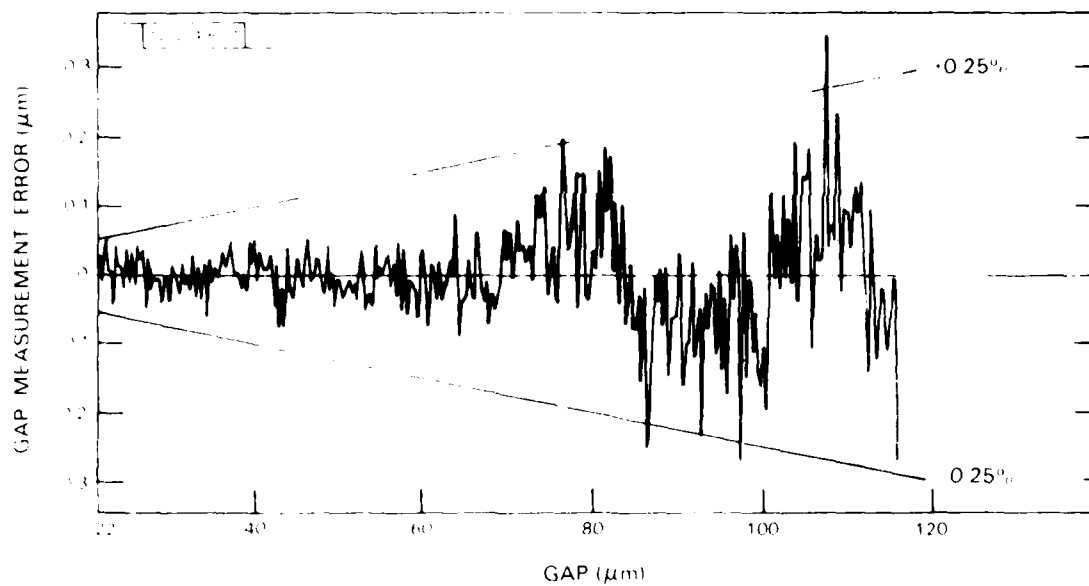


Fig. 4-4. Plot of gap measurement error vs. gap. Lines bounding  $\pm 0.25\%$  error are shown.

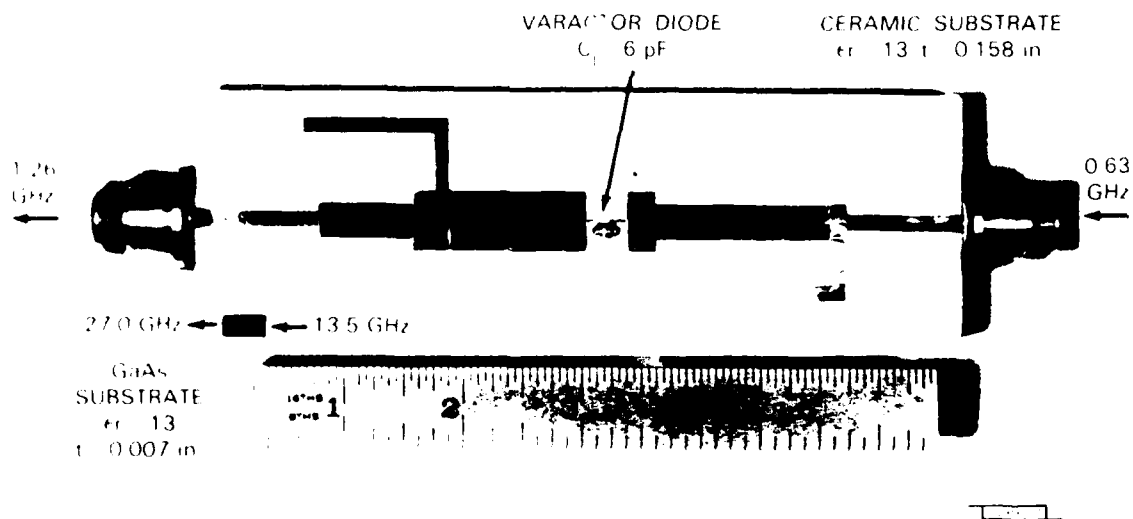


Fig. 4-5. Scaled model for design of monolithic frequency doublers. Scaling factor is 22.57 to 1.

this prototype can be modified conveniently because the parasitic effects of diode packages and wires are negligible at low frequencies. This is in contrast to modifications in the actual monolithic circuit, which would require the generation of new masks and the processing of new devices and circuits. Such operations are both expensive and time consuming.

Figure 4-5 also shows the GaAs monolithic frequency doubler which was designed by scaling down the dimensions from the lower frequency prototype by a factor of 22.57. The scaled values for the thickness of the GaAs substrate and zero-bias junction capacitance are 0.175 mm and 0.25 pF, respectively. Calculated values of scaled input and output frequencies are 14.22 and 28.44 GHz. These calculated values proved somewhat higher than the measured operating frequencies of the monolithic circuit because the junction capacitance of the integrated varactor diode was higher than the design value.

The microstrip implementation (Fig. 4-5) was chosen for its simplicity. The series connection of the diode was selected because planar varactor diodes can be fabricated with anode and cathode contacts as integral parts of the transmission lines. Input and output matching networks consist of quarter-wave transformer sections with open-circuited shunt stubs that are resonant at output and input frequencies. Their positions were selected to reflect the appropriate impedances at the plane of the diode.

The anode of the planar varactor diode (Fig. 4-6) is formed by a metal-semiconductor Schottky barrier on an  $\sim 1\text{-}\mu\text{m}$ -thick  $n$ -type layer of GaAs doped to a concentration of  $\sim 2 \times 10^{16} \text{ cm}^{-3}$ . The area of the anode is  $\sim 560 \mu\text{m}^2$ . The cathode is formed on a 3.5- to 4.0- $\mu\text{m}$ -thick,  $n^+$  layer doped to an impurity concentration in the range of  $2$  to  $3 \times 10^{18} \text{ cm}^{-3}$ . The crosshatched areas in Fig. 4-6 represent regions of GaAs that are rendered semi-insulating by the bombardment of protons. These regions permit the connection of circuit elements to the anode over the etched step of the mesa.

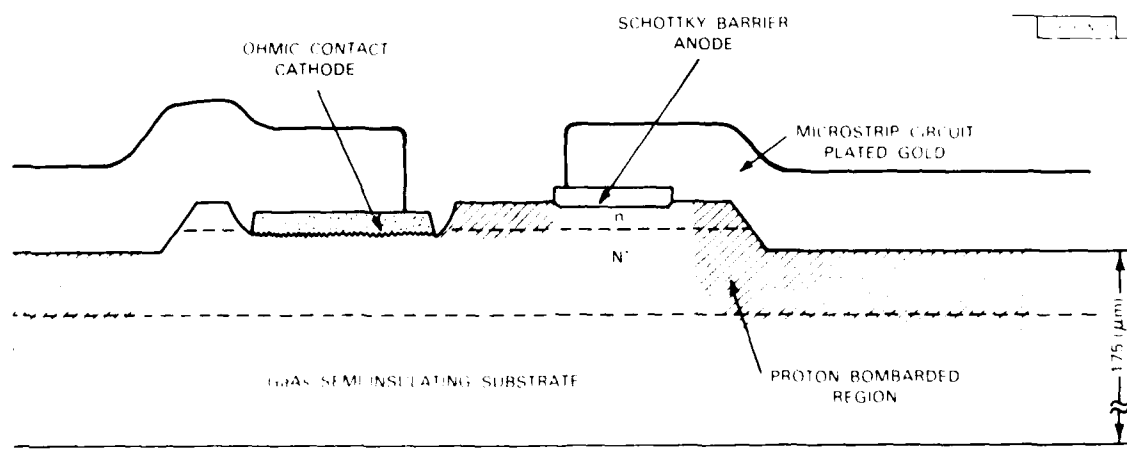


Fig. 4-6. Planar monolithic varactor diode with  $n$  and  $n^+$  epitaxial layers for anode and cathode contacts, respectively. Transmission lines are formed over proton bombarded regions.

Major operations in the fabrication sequence of the varactor diode doubler are the formation of ohmic contacts, electrical isolation of devices, formation of a Schottky barrier anode junction, and plating of circuit elements as illustrated in Fig. 4-7. Fabrication begins with the definition of windows in the photoresist layer for the ohmic contacts. The n layer is etched away from these areas, after which the ohmic contact metals are evaporated and the contacts are formed by photoresist lift-off. The contacts are alloyed at 460°C. Specific contact resistances below  $10^{-6} \Omega \text{ cm}^2$  are usually obtained. The ohmic contact alloyed into the n<sup>+</sup> layer is illustrated in Fig. 4-7a. The electrical isolation of devices is accomplished in two steps, mesa etching followed by proton bombardment (Fig. 4-7b). The two-step isolation process is used because the combined thickness of the n and n<sup>+</sup> layers is approximately 5.0  $\mu\text{m}$ , which exceeds the layer thickness that the 400-keV proton beam can render insulating. The bombardment mask is designed to expose the etched mesa step of the anode to the proton bombardment, allowing fabrication of the transmission line over the mesa step adjacent to the anode (Fig. 4-7c). The node is formed by an evaporated platinum layer on n-type GaAs. The microstrip and bias lines are then electroplated with gold to multiple skin depths. The process is completed with a low-energy proton implant which passivates the GaAs region between the anode and cathode contacts. A monolithic circuit produced by this process is shown in Fig. 4-8. The die measures 4 by 8 mm. The planar varactor diode is shown at a higher magnification in Fig. 4-9.

Devices produced by the above process exhibit ideality factors of 1.05 and breakdown voltages of 18 V. The junction capacitance of the diode is plotted as a function of the reverse bias voltage in Fig. 4-10. The zero-bias junction capacitance of 0.35 pF is approximately 0.1 pF higher than the design value. As previously mentioned, the consequence of this higher capacitance is a decrease in the operating frequency of the doubler. The varactor frequency doubler is mounted in a test fixture between two short sections of 50-ohm microstrip lines fabricated on 0.010-in. alumina substrates. The microstrip lines are connected to OSSM launchers. The combined RF losses of the launchers and microstrip lines are estimated conservatively as ~0.3 dB at the input and ~0.5 dB at the output. RF test results for the monolithic frequency doubler (Figs. 4-11, -12) relate to power levels measured at test fixture connectors. Performance at the chip level is obtained by accounting for RF losses in the test fixture. The output power as a function of output frequency is plotted in Fig. 4-11. In this measurement the input power is kept constant at 182.4 mW. Output power is in excess of 17.5 mW between 25.6 and 27.4 GHz, and the 3-dB output bandwidth is approximately 2 GHz. Output power exceeds 20 mW over this frequency range at the chip level. The relationship of output power and conversion efficiency to input power is shown in Fig. 4-12. In this measurement the frequency is kept constant at 25.8 GHz. The maximum output power is 38.6 mW at 15.5% efficiency. At the chip level the corresponding maximum output power and conversion efficiency are 43 mW and 20%, respectively. A maximum conversion efficiency of 24% is obtained at a reduced output power of 25 mW at the chip level.

A. Chu  
W.E. Courtney  
(Group 33)

L.J. Mahoney  
R.A. Murphy  
R.W. McClelland

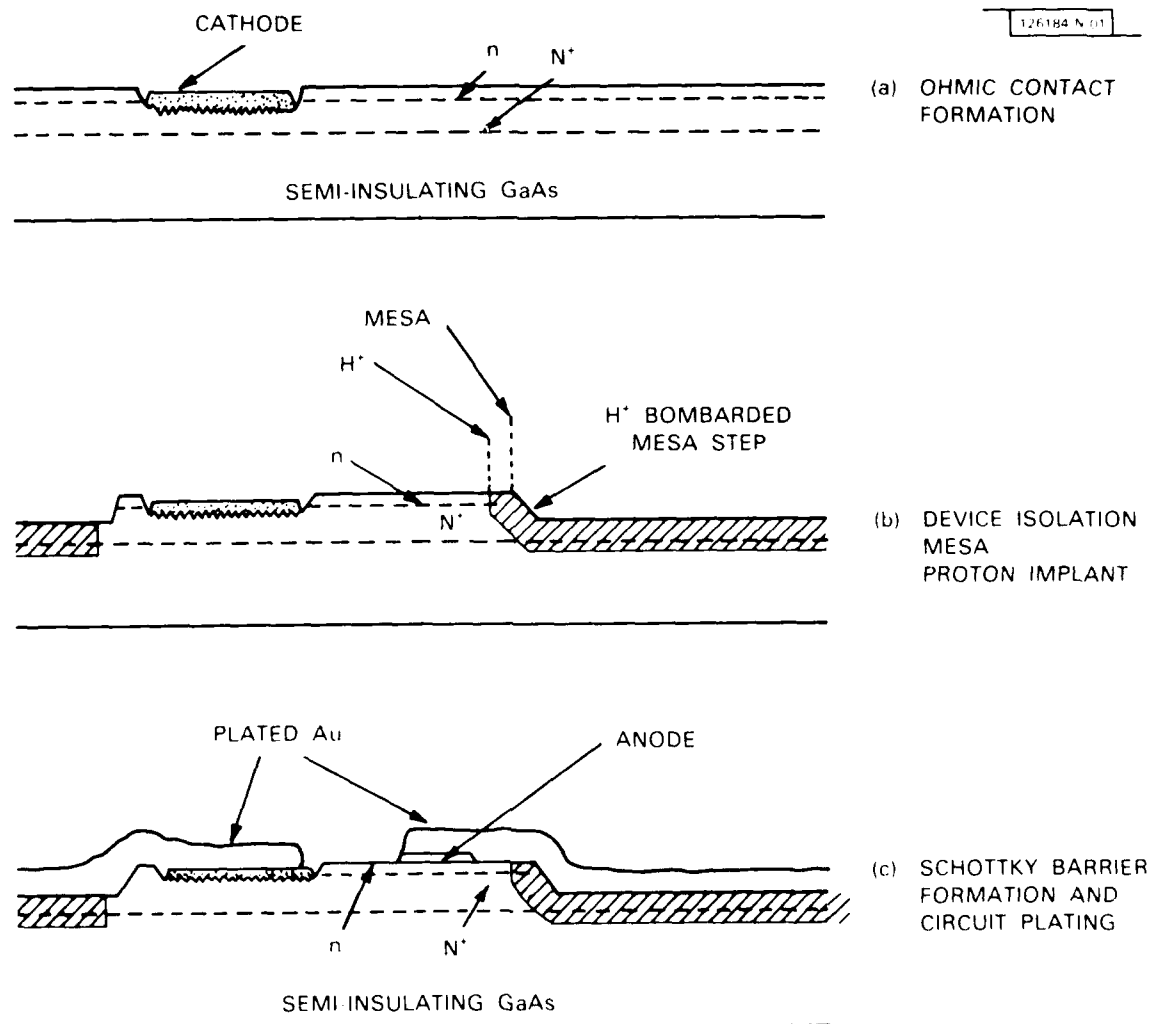


Fig. 4-7. Highlights of fabrication sequence: (a) ohmic contact formation; (b) device isolation: mesa and proton bombardment; (c) Schottky barrier formation and circuit plating.

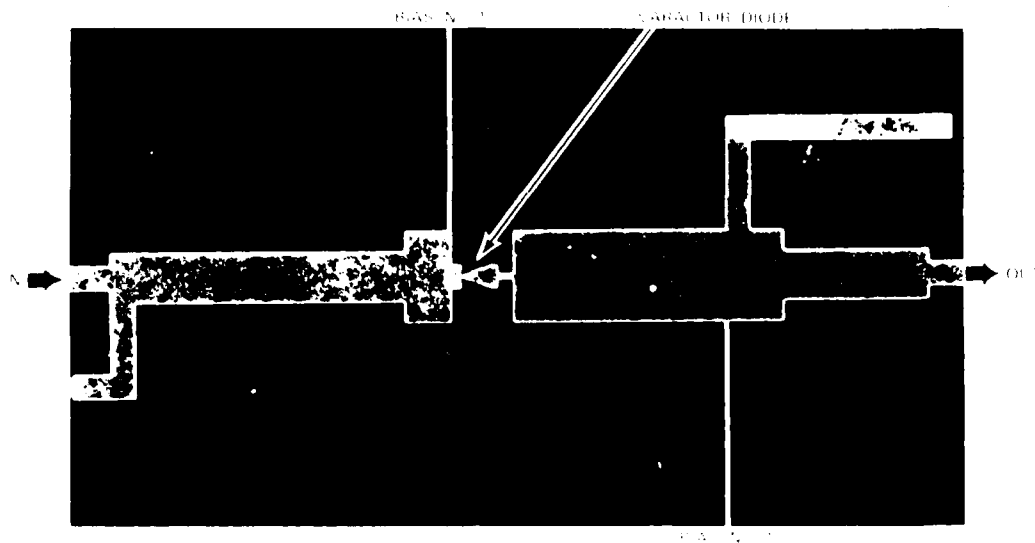


Fig. 4-8. Monolithic frequency doubler. Varactor diode is integrated with microstrip circuits and bias lines. Chip dimensions:  $4 \times 8$  mm.

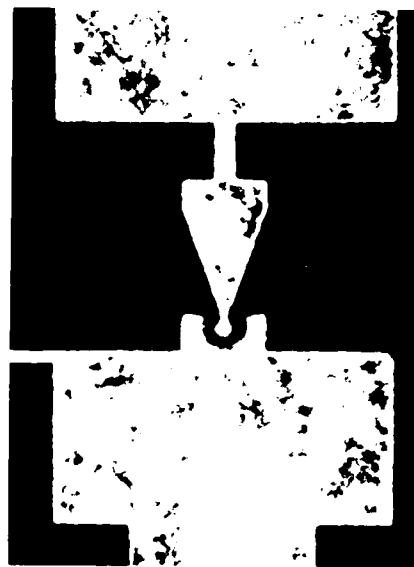


Fig. 4-9. (Right) Monolithic varactor diode. Diode terminals are integral part of embedding circuit.

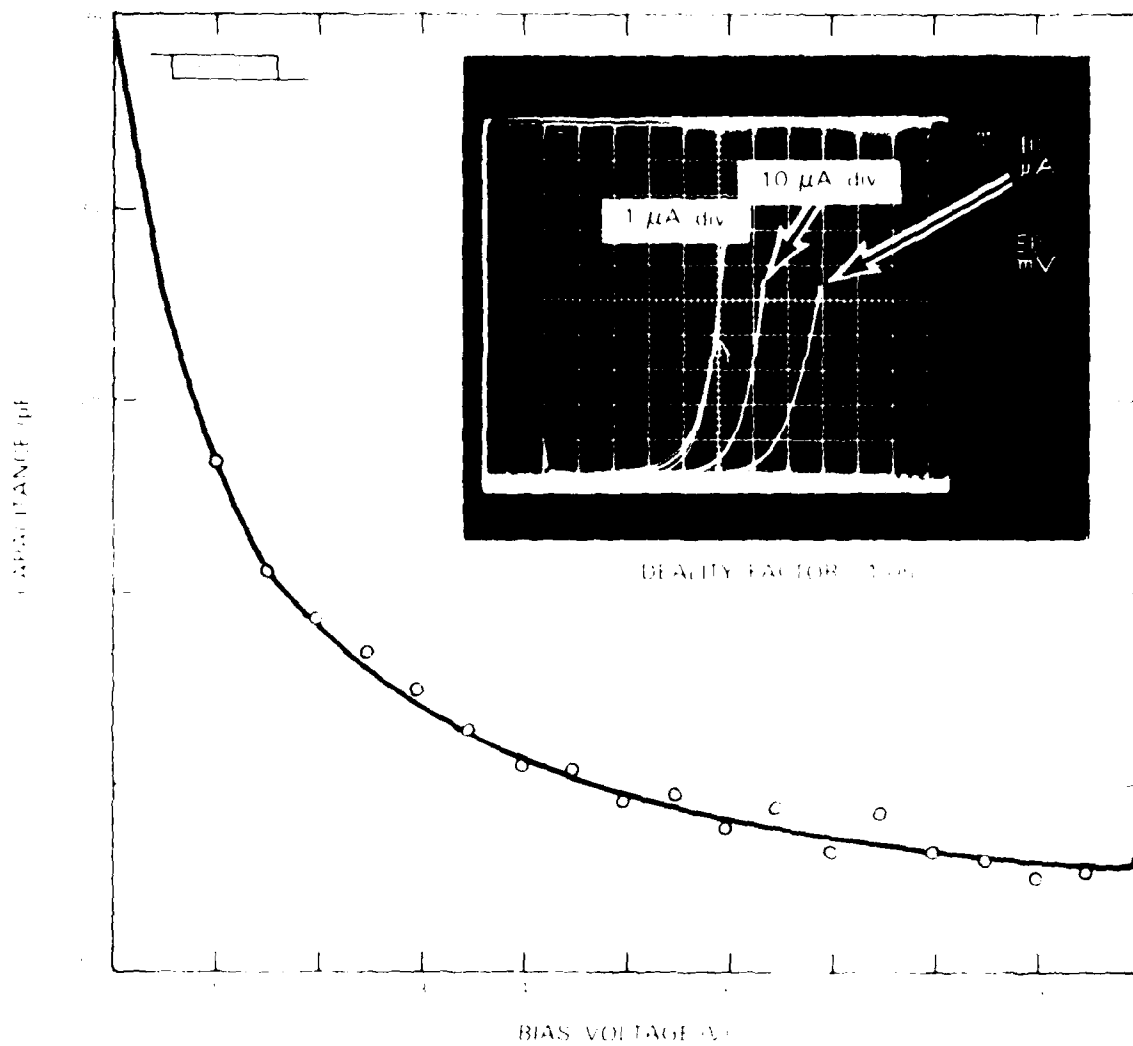


Fig. 4-10. Junction capacitance vs. reverse bias voltage of monolithic varactor diode. Inset: forward diode currents vs. bias voltage in a multiple-exposure photograph. Traces correspond to three current scales: 1, 10, and 100  $\mu\text{A/div}$ .



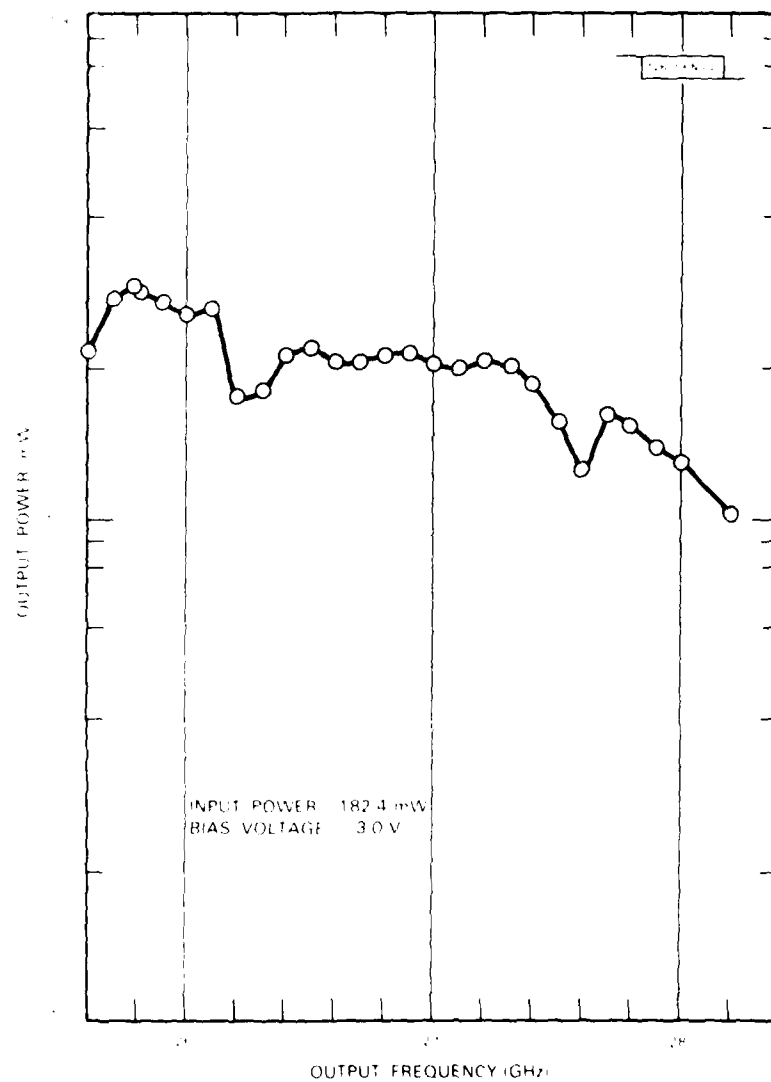


Fig. 4-11. Output power vs. output frequency curve of monolithic varactor frequency doubler at test fixture terminals.

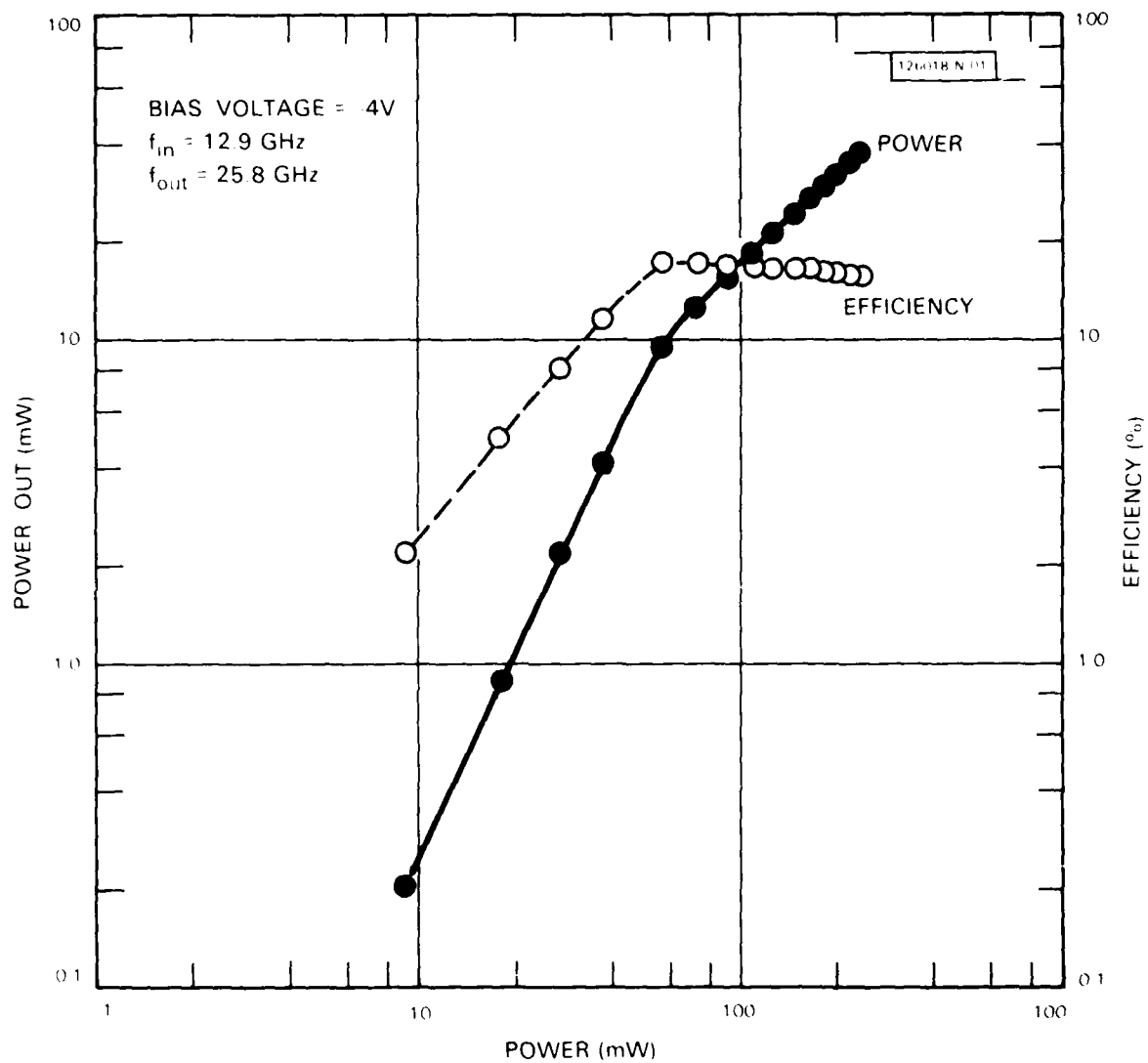


Fig. 4-12. Measured output power and conversion efficiency of monolithic varactor frequency doubler as a function of input power at test fixture terminals.

### 4.3 RESONANT TUNNELING THROUGH QUANTUM WELLS AT FREQUENCIES UP TO 2.5 THz

Quantum wells are the subject of considerable theoretical and experimental study. They consist of thin ( $<100$  Å) layers of material, usually a semiconductor confined between two layers of a different material with a larger bandgap. In this way, carriers are confined to the lower bandgap material. If the barriers are sufficiently thin, then carriers can tunnel through them, and it becomes possible to probe the quantum wells with carriers.

We have observed resonant tunneling through a single quantum well of GaAs between two barriers of GaAlAs. Resonant tunneling features are visible at room temperature, and a broad region of negative resistance is observable at 200°K. At 25°K we have observed the largest peak-to-valley ratio yet reported (6:1). By comparing high-frequency current response measurements with the observed dc characteristics, we have established that response times are less than  $10^{-13}$  sec and are thus consistent with tunneling. In addition, we have carried out mixing experiments in these devices at various millimeter and submillimeter wavelengths down to 119  $\mu$ m.

Tsu and Esaki<sup>5</sup> have shown that a large peak in the tunneling current should occur when the injected carriers have certain resonant energies. Figure 4-13 shows schematically how resonance occurs with applied dc bias. The electrons originate near the Fermi level to the left of the first barrier of height,  $\Delta E$ , tunnel into the well, and finally, tunnel through the second barrier into unoccupied states. Resonance occurs when the electron-wave function reflected at the first barrier is cancelled by the wave which leaks from the well in the same direction, or, equivalently, when the energy of the injected carrier becomes approximately equal to the energy level of the electrons confined in the well.

Previous measurements of heterojunction quantum well structures have shown evidence of resonant tunneling.<sup>6,7</sup> These measurements, however, have shown only small regions of negative resistance, if any, and near unity peak-to-valley ratios. No resonant tunneling features were observed at room temperature. Also, no measurements of response time were reported.

The structure, shown schematically in Fig. 4-13, was prepared by molecular beam epitaxy on an n-type wafer of GaAs. The net donor (Si) concentration in the GaAs outside the barriers is  $10^{18}$  cm<sup>-3</sup>, and the GaAs well was doped to an average concentration of  $10^{17}$  cm<sup>-3</sup> by placing a layer of  $10^{18}$  cm<sup>-3</sup> material in the central 10% of the well. The resulting band bending within the well is negligible compared to  $kT$ . The top layer of GaAs is about 5000 Å thick. The barriers of Ga<sub>1-x</sub>Al<sub>x</sub>As were not doped intentionally and are presumed to be semi-insulating due to defect compensation. The substrate growth temperature was 680°C, and the flux ratio of As to Ga as measured from an ion gauge placed at the substrate growth position was 19:1. The Al concentration was measured by STEM X-ray analysis of the barriers and from thicker films grown under similar conditions. Both methods gave  $x = 25$ -30%. The barrier and well dimensions of 50 Å were determined by TEM.

Arrays of mesas 5  $\mu$ m square were etched into the completed wafer with ohmic contacts top and bottom. The wafers were then diced into 10-mil-square chips and mounted in

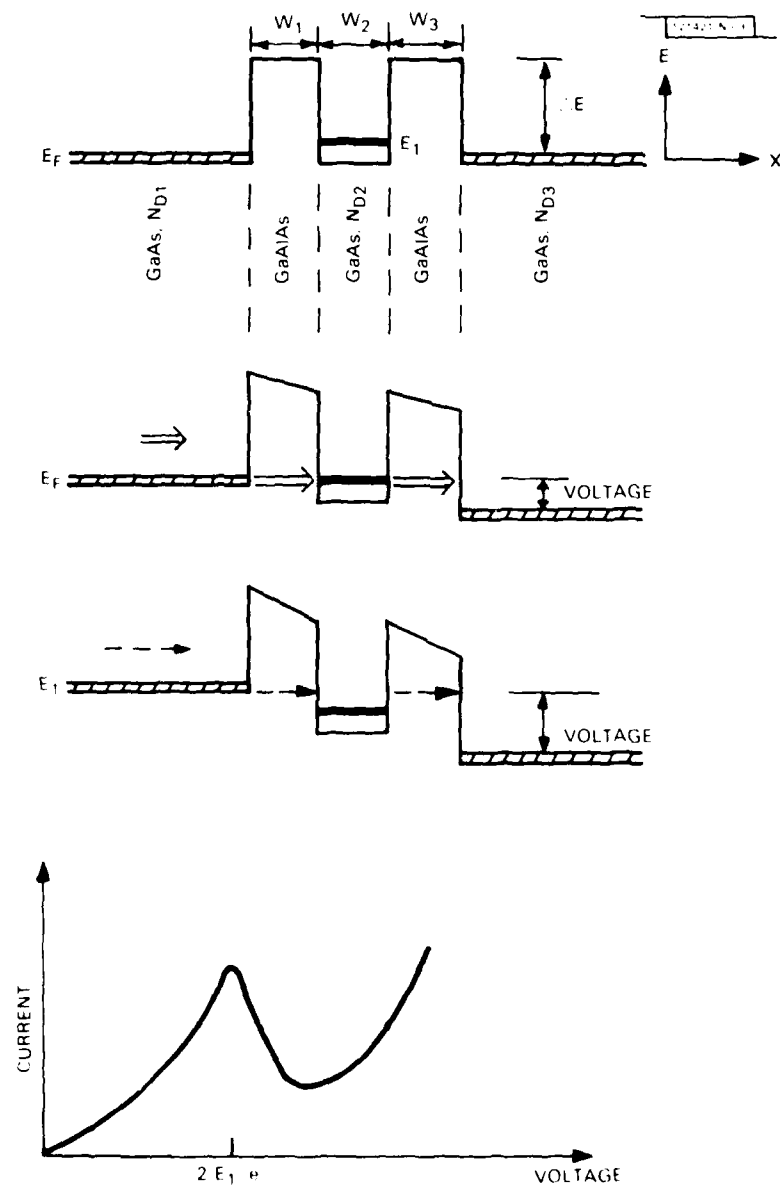


Fig. 4-13. Electron energy as a function of position in quantum well structure. Parameters are  $N_{D1} = N_{D3} = 10^{18} \text{ cm}^{-3}$ ,  $N_{D2} = 10^{17} \text{ cm}^{-3}$ , and  $W_1 = W_2 = W_3 = 52 \text{ \AA}$ . Doping level in well center is an average value achieved by placing a layer of  $10^{18} \text{ cm}^{-3}$  material in the central 10% of the well. Energy level  $E_1$  occurs above the bottom of the bulk conduction band because of confinement in x-direction.

a corner cube detector mount with a whisker contacting the mesa. The corner cube structure has been used routinely in our laboratory to mount Schottky diodes to be used as detectors and mixers and is well characterized at submillimeter wavelengths.<sup>8</sup>

The observed dc current-voltage and conductance-voltage curves are shown in Fig. 4-14 for several temperatures. Submillimeter measurements were made at 138 GHz, 761 GHz, and 2.5 THz with a carcinotron and far-IR lasers, respectively. We measured the current response as a function of dc bias voltage, and calculated the current responsivity following Torrey and Whitmer,<sup>9</sup> but accounting for the mismatch between the antenna impedance of the corner cube and the device impedance.

At all three frequencies the measured current response agrees with the calculated value within a few dB. In Fig. 4-15, expanding on an approach used first by Small *et al.*,<sup>10</sup> we show the measured and calculated current response at 2.5 THz. Since the general shape of the two curves is the same, it follows that the I-V curve at 2.5 THz must be very similar to the dc I-V curve. In addition, the magnitude of the calculated current response agrees rather well with the measured curve considering the uncertainties in the parameters. The somewhat greater discrepancy between measured and calculated values at large voltages may arise from quantum effects of photon-assisted tunneling. The agreement is sufficient to show that the charge transport mechanism is at least as fast as the angular period of 2.5 THz (i.e.,  $\tau = 6 \times 10^{-14}$  sec). Further verification has been obtained by mixing two sources near 140 GHz in the device, as well as by the observation of far-infrared laser mode beats at 434 and 119  $\mu\text{m}$ .

The time required for electrons to transit both barriers and the well can be estimated by assuming that tunneling times are approximately given by the uncertainty relation,  $\tau \leq \hbar/E$ , and that the saturation velocity of  $10^7$  cm/sec is achieved in the well. This yields an estimate of order  $10^{-13}$  sec.

The existence of a large negative resistance at very high frequencies suggests applying these devices to millimeter and submillimeter amplifiers and oscillators by designing appropriate resonance circuits and matching the device to the resonator. Since these devices can be fabricated with planar technology, feedback and antenna elements could be placed very near the active area, thereby reducing losses. Also, arrays of elements could be used in distributed circuits.

T.C.L.G. Sollner  
W.D. Goodhue  
P.E. Tannenwald

C.D. Parker  
D.D. Peck

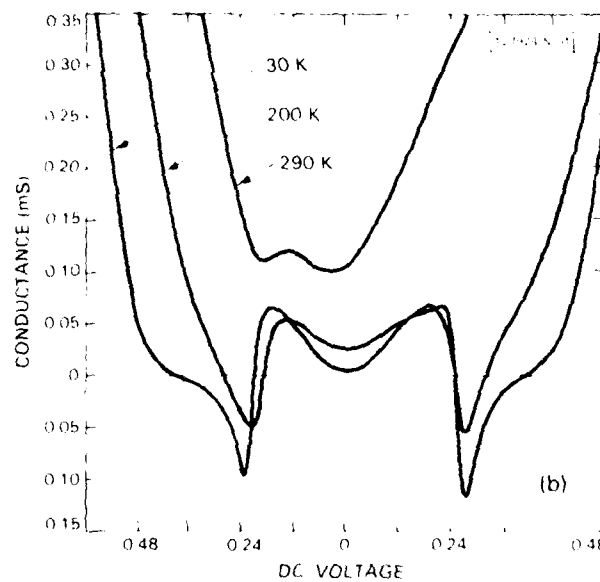
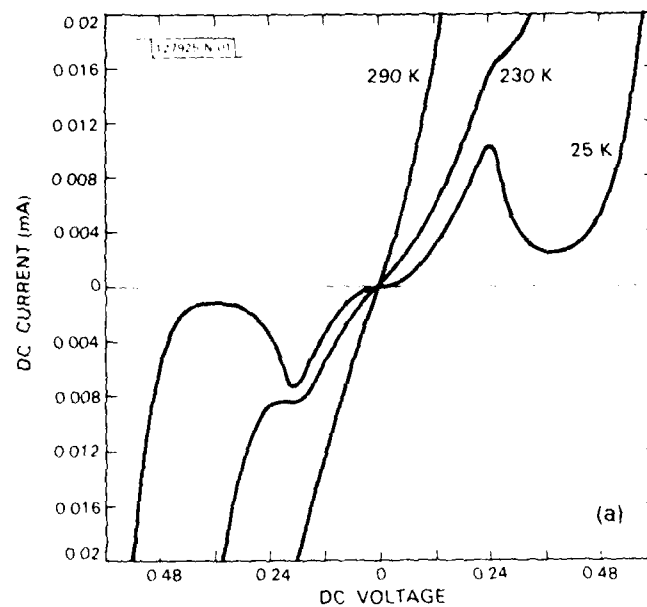


Fig. 4-14. Curves for (a) current-voltage and (b) conductance ( $di/dV$ )-voltage at several temperatures. Resonant tunneling features can be seen even at room temperature.

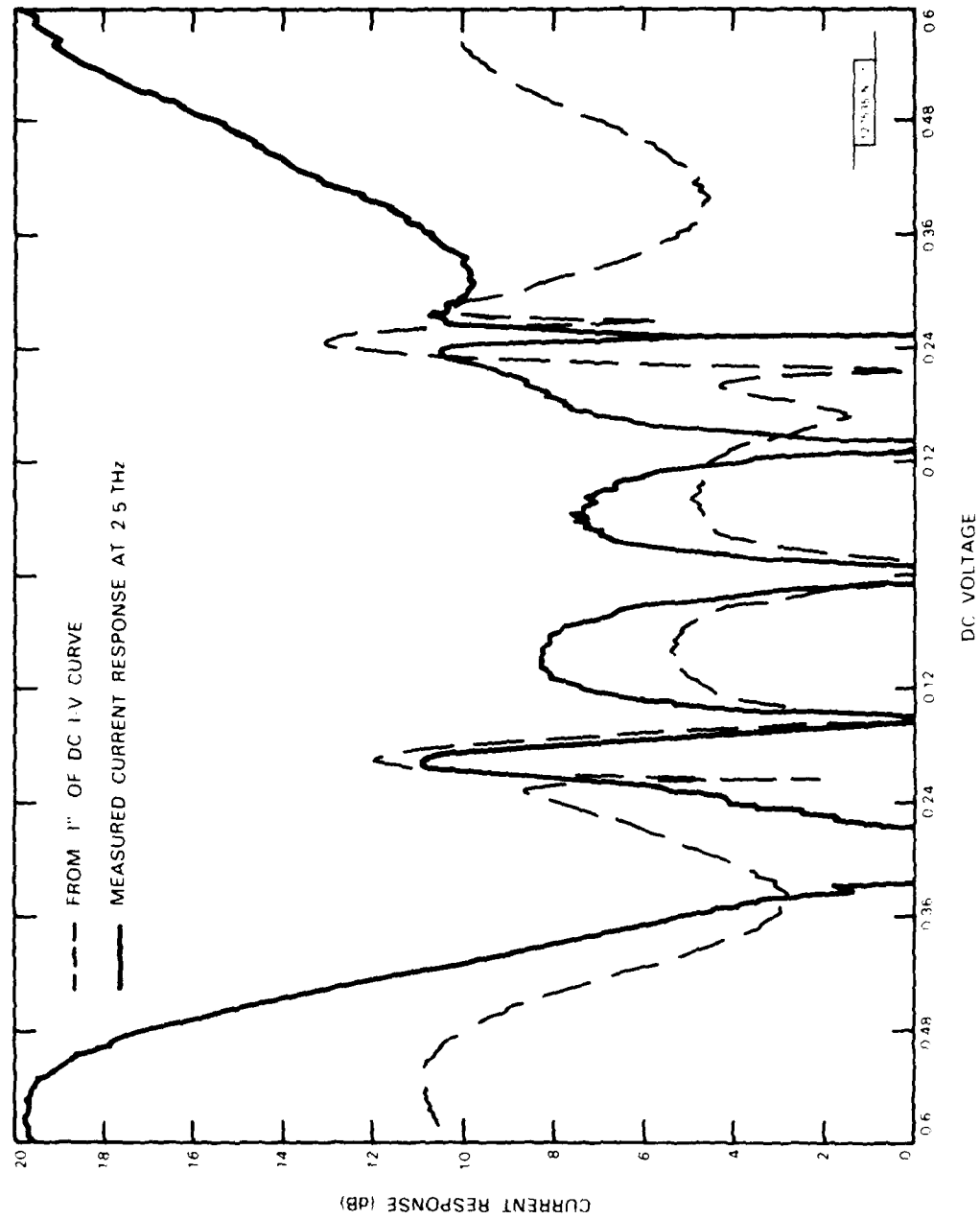


Fig. 4-15. Current response at 2.5 THz as a function of dc bias voltage. Dashed curve is calculated on the basis of the dc I-V curve. Zero dB corresponds to  $0.3 \mu\text{A/W}$ . The general agreement shows that I-V curve at 2.5 THz is very similar to dc curve, and thus the charge transport is fast.

## REFERENCES

1. B. Fay, A. Cornette, and J.P. Nivoliens, *1982 International Electron Devices Technical Digest* (IEEE, Piscataway, New Jersey), p. 411.
2. J.L. Bartelt, C.W. Slayman, J.E. Wood, J.Y. Chen, C.M. McKenna, C.P. Minning, J.E. Coakley, R.E. Holman, and C.M. Perrygo, *J. Vac. Sci. Technol.* **19**, 1166 (1981).
3. B. Fay, J. Trostel, and A. Frichet, *J. Vac. Sci. Technol.* **16**, 1954 (1979).
4. T.M. Lyszczarz, D.C. Flanders, N.P. Economou, and P.D. DeGraff, *J. Vac. Sci. Technol.* **19**, 1214 (1981), DTIC AD-A117803 7.
5. R. Tsu and L. Esaki, *Appl. Phys. Lett.* **22**, 562 (1973).
6. L.L. Chang, L. Esaki, and R. Tsu, *Appl. Phys. Lett.* **24**, 593 (1974).
7. B.A. Vojak, S.W. Kirchoefer, H. Holonyak, Jr., R.D. Dupuis, P.D. Dapkus, and R. Chin, *J. Appl. Phys.* **50**, 5830 (1979).
8. H.R. Fetterman, P.E. Tannenwald, B.J. Clifton, C.D. Parker, W.D. Fitzgerald, and N.R. Erickson, *Appl. Phys. Lett.* **33**, 151 (1978), DTIC AD-A061203 6.
9. H.C. Torrey and C.A. Whitmer, *Crystal Rectifiers* (McGraw-Hill, New York, 1948), p. 336.
10. J.G. Small, G.M. Elchinger, A. Javan, A. Sanchez, F.J. Bachner, and D.L. Smythe, *Appl. Phys. Lett.* **24**, 275 (1974).



## 5. ANALOG DEVICE TECHNOLOGY

### 5.1 LOW-LOSS SUBSTRATES FOR SUPERCONDUCTIVE CIRCUITS

In a previous report<sup>1</sup> the dielectric properties of silicon at low temperature were examined and suitability as a substrate for superconductive microwave devices was demonstrated. Silicon can support low-loss striplines with low material dispersion. However, to implement stripline devices of adequate delay<sup>2</sup> on a compact substrate ( $\leq 7.5$ -cm dia.), one must use substrates less than  $25\text{-}\mu\text{m}$  thick. Silicon is fragile, and free-standing substrates thinner than  $125\text{ }\mu\text{m}$  are very difficult to handle. This report outlines a concept and gives preliminary results to support thin silicon. In addition, other isotropic substrates have been studied.

#### 5.1.1 Supported Silicon Substrates

Because of the fragility of silicon it is desirable to start with a thicker substrate which, after being attached to a support wafer, can be accurately thinned by selective etching of heavily doped silicon (Fig. 5-1).

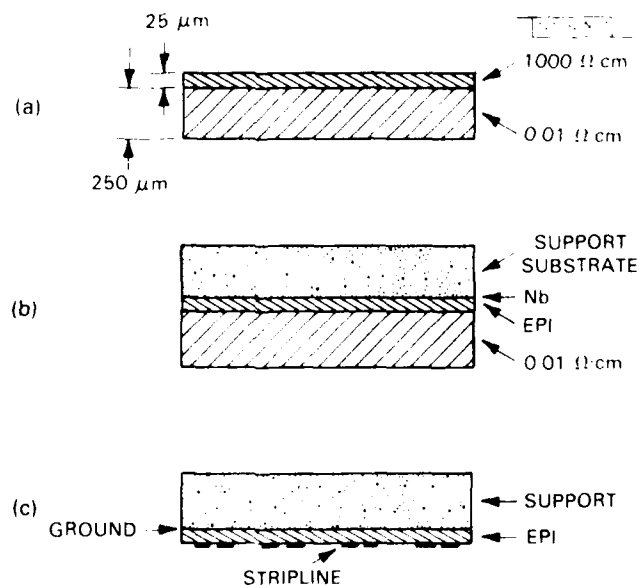


Fig. 5-1. Proposed fabrication of  $25\text{-}\mu\text{m}$ -thick silicon wafers by epitaxial deposition and preferential etching: (a) starting material; (b) assembly after deposition of Nb ground plane and bonding to support wafer; (c) completed structures after the preferential removal of the original substrate, Nb deposition and photolithographic definition of stripline circuit.

Epitaxial layers of sufficient resistivity ( $100\ \Omega\text{-cm}$ ), thickness ( $10\text{-}25\ \mu\text{m}$ ), and crystalline quality for superconductive substrates have been deposited by an outside vendor on heavily doped silicon. After these epitaxial substrates are attached to another silicon wafer, preferential etching removes the highly doped substrate. The selective etch is a mixture of nitric, hydrofluoric, and acetic acids that attacks heavily doped silicon rapidly but lightly doped material only slightly.<sup>3</sup> To date, the best surface finishes achieved have  $\sim 2000\ \text{\AA}$  rms roughness. The most critical material problem is that of the bonding layer. It must include a superconductive ground plane and, in addition, must be compatible with the elevated temperatures used to deposit Nb or high-transition-temperature Nb-alloy superconductors for the stripline. Process development is continuing.

### 5.1.2 Material Evaluation Technique

As described previously,<sup>1</sup> resonators are a convenient vehicle with which to evaluate loss and dispersion of candidate dielectrics. Besides the simple resonator structure described earlier (Fig. 5-2a), the two other configurations in Fig. 5-2 were used. The multipath resonator was used to test the uniformity of the substrate; the four-port structure was used to evaluate the quality of the Nb by measuring the ratio of resistivities at  $300$  and  $77^\circ\text{K}$ .<sup>4</sup> In all cases, the coupling gap was chosen to minimize the external loading.

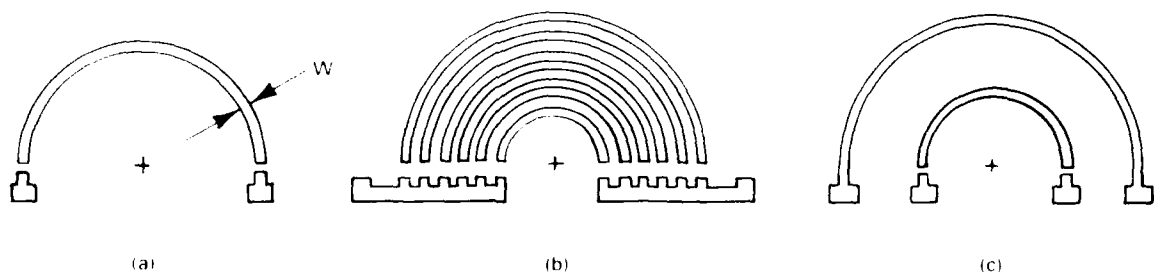


Fig. 5-2. Test structures to evaluate substrates: (a) simple resonator, (b) multiple resonator, (c) resonator and delay line.

The  $Q$  was measured by a signal generator with a resolution of  $1000\ \text{Hz}$  at  $10\ \text{GHz}$ . For the highest values of  $Q$ , the decay constant of a gated RF signal was also measured; identical results were obtained. The absence of dispersion in each dielectric was deduced by observing the variation of the difference in frequency between successive modes of the resonance. The lack of a systematic variation observed for all of the materials tested was taken to indicate dispersionless substrates. Isotropy is an important feature, as it permits

proximity-tapped structures to have large time-bandwidth products<sup>1</sup> without excessive loss. All of the materials evaluated below, except sapphire, are isotropic or nearly so.

### 5.1.3 Substrate Properties

**Crystalline Quartz:** Thin substrates (down to 25  $\mu\text{m}$ ) can be obtained from different vendors. Highly polished surfaces can be obtained by the use of colloidal silica abrasive. Crystalline quartz is compatible with Nb processing. Quartz is, however, very fragile and very difficult to handle. Also, the low dielectric constant ( $\epsilon_r = 4.5$ ) makes the devices built on quartz of a larger area than equivalent devices built on other substrates. Quartz is almost dielectrically isotropic. Because of the difficulty in handling quartz, losses and dispersion measurements were made on 350- $\mu\text{m}$ -thick substrates. The results of Q measurements for this, and the other materials, are presented in Table 5-1.

TABLE 5-1 RESONATOR Q FOR DIFFERENT SUBSTRATE MATERIALS						
	$f_1$ (GHz)	$Q_1$ $\times 10^3$	$f_2$ (GHz)	$Q_2$ $\times 10^3$	$f_3$ (GHz)	$Q_3$ $\times 10^3$
Crystal Quartz	1.393	10.7	1.833	1.41	7.05	0.156
Amorphous Quartz	----	----	1.22	1.0	7.27	5.5
Calcium Fluoride	0.359	44.8	1.800	3.093	----	----
Alumina	0.688	0.688	1.608	0.893	----	----
Sapphire $C_{\perp}$	0.567	113.	1.703	17.0	7.74	17.5
Sapphire $C_{\parallel}$	0.650	75.	1.83	18.0	----	----
Silicon	0.529	105.	1.589	48.0	7.60	15.5

**Amorphous (Fused Synthetic) Quartz:** RF loss increases with water content.<sup>5</sup> For this reason Supersil 2 with a low water content was chosen. The thinnest substrates used were 200- $\mu\text{m}$  thick, but thinner substrates can be obtained. Amorphous quartz is also very fragile and more difficult than crystalline quartz to polish because of gas-bubble inclusions that result in pits on the surface. This material is obviously isotropic and has an even lower dielectric constant ( $\epsilon_r = 3.8$ ) than crystalline quartz.

**Calcium Fluoride:** This material, commonly used for infrared windows, can be obtained in large diameters. It is very easy to polish but is slightly hygroscopic and very soft. Thin substrates could not be obtained commercially. Attempts to cut thin slices were unsuccessful most of the time. Because of this difficulty, measurements of Q were made on a stripline consisting of a Nb line on sapphire with the top insulator being the calcium fluoride. Calcium fluoride is cubic and so is dielectrically isotropic.

**Alumina:** Large area substrates as thin as 100  $\mu\text{m}$  are readily available. This polycrystalline material is nearly isotropic. The surface, even when polished, has enough pits to limit photolithographic resolution to tens of microns. Fine-grain alumina has a wavy surface that further limits the photolithographic resolution and causes problems with stripline packaging of the upper and lower dielectrics.

**Sapphire:** Sapphire is a very low-loss material, as previously reported.<sup>6</sup> It is very rugged; substrates as thin as 75  $\mu\text{m}$  are processed routinely by automatic cleaning equipment (scrubbers) without breakage. Round substrates with c-axis in the plane of the substrate, or perpendicular to it, were obtained with highly polished surfaces ("epitaxial finish").

For most applications the substrate losses for sapphire can be ignored. This low loss, coupled with its ruggedness, makes sapphire the material of choice for evaluating experimental device structures and monitor the quality of niobium and other superconductive films.

Of the many isotropic substrate materials evaluated for large time-bandwidth product devices, silicon is the best, and efforts will continue on the proper thinning of supported silicon wafers.

A.C. Anderson  
R.S. Withers  
S.A. Reible

## 5.2 SUPERCONDUCTOR-INSULATOR-SUPERCONDUCTOR JUNCTIONS

Superconductor-insulator-superconductor (SIS) tunnel junctions with high-frequency mixing<sup>7</sup> capability are being developed for use in programmable analog signal-processing devices.<sup>8</sup> A junction consists of niobium (Nb) and lead (Pb) superconducting thin-film electrodes separated by a very thin ( $\sim 30$  Å) insulating layer of niobium oxide ( $\text{Nb}_2\text{O}_5$ ). General fabrication techniques were described previously.<sup>9</sup> This report describes the dc electrical performance and relates these characteristics to the quality of the Nb  $\text{Nb}_2\text{O}_5$  interface. Also, the long-term stability of these high-quality junctions is characterized.

To standardize the collection of data from junction I-V characteristics, measurement of the critical Josephson current,  $I_c$ , leakage current,  $I_\ell$ , and normal current,  $I_n$ , are made at barrier potentials of 0, 2, and 4 mV (Fig. 5-3). Other significant parameters are the superconducting gap voltage,  $V_g$ , the normal state tunnel resistance,  $R_n$ , and the subgap leakage resistance,  $R_\ell$ . Standard figures of merit for tunnel junctions are the  $I_c R_n$  and  $I_c R_\ell$  products, and the resistance ratio  $R_\ell / R_n$ . Several parameters for Nb-based tunnel junctions at 4.2°K along with their intended applications are listed in Table 5-2.

The I-V characteristic of a high-quality junction is shown in Fig. 5-4. Tight control of process parameters is very important in the fabrication of Josephson tunnel junctions with reproducible I-V characteristics. The Nb base electrode is first cleaned by RF sputter etching and then a uniform oxide layer is grown in an  $\text{O}_2/\text{Ar}_2$  plasma. Proper control of gas pressures, sputtering voltages, temperatures and times allow fabrication of tunnel junctions with normal current densities,  $J_n$ , up to  $10^5$  A/cm<sup>2</sup> combined with low subgap leakage currents.

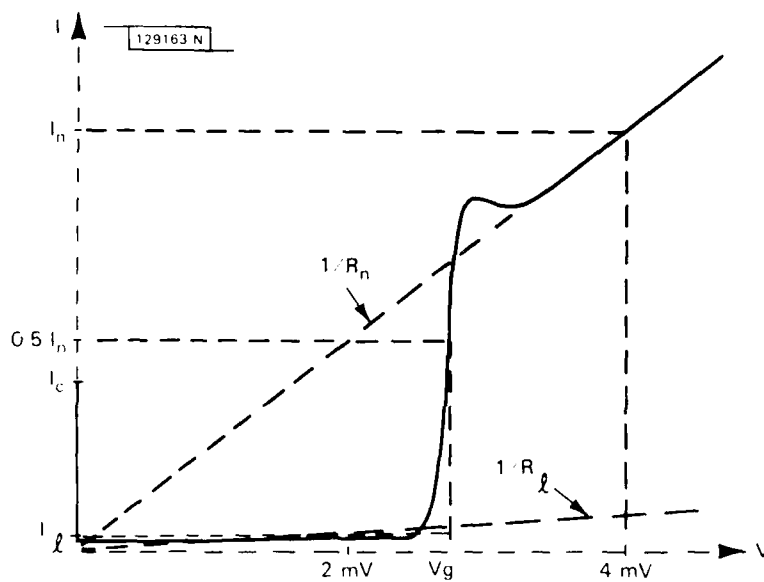


Fig. 5-3. I-V characteristics of a Nb/Nb<sub>2</sub>O<sub>5</sub>/Pb tunnel junction showing significant parameters.

TABLE 5-2  
SIS TUNNEL JUNCTION CHARACTERISTICS

Application	Area (cm <sup>2</sup> )	$J_n$ (A/cm <sup>2</sup> )	$I_c R_n$ (mV)	$I_c R_l$ (mV)	$R_l/R_n$
Test Junctions	$2.4 \times 10^{-6}$	$1.0 \times 10^3$	1.5	21	15
Convolver	$1.6 \times 10^{-7}$	$5.6 \times 10^2$	1.4	16	12
mm-Wave Mixers	$8 \times 10^{-9}$	$9.5 \times 10^4$	1.4	14	10

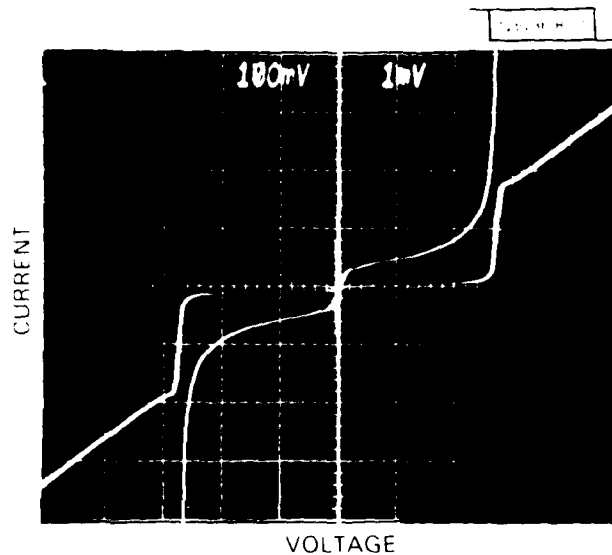


Fig. 5-4. I-V characteristics of a Nb/Nb<sub>2</sub>O<sub>5</sub>/Pb junction at 4.2°K. Vertical scales are 1 and 0.1 mA/div; horizontal scale is 1 mV/div.

High current densities ensure junction response times of 3 ps or less, while low-leakage currents provide efficient and sensitive mixing interactions in analog devices and large fanout capability in digital logic arrays.

Strong evidence exists that high-quality junctions are realized only when the tunnel barrier consists of Nb<sub>2</sub>O<sub>5</sub> and the transition region of conducting suboxides such as NbO and NbO<sub>2</sub> between the Nb<sub>2</sub>O<sub>5</sub> barrier and Nb electrode is much thinner<sup>10</sup> than the ~75 Å coherence length of the RF-sputtered Nb film. The transition region of suboxides which forms during Nb<sub>2</sub>O<sub>5</sub> growth acts as a poor-quality superconductor with a substantially depressed transition temperature compared to Nb, and thus provides high-leakage current through thermal generation of quasiparticles (normal electrons). By comparison, for Nb and Pb thin films having ideal transition temperatures, the theoretical  $I_c$  at 4.2°K should be less than 1%  $I_n$ . Also, through the proximity effect between the Nb and NbO<sub>x</sub> superconductors, the density of electron states is distorted, reducing the sharpness of the current knee at  $V_g$  and leading to a small nonlinearity in the I-V characteristic immediately above the knee (Fig. 5-4).

While the programmable signal processing devices, such as the superconductive convolver,<sup>11</sup> require up to eight thin films, the test junctions referred to in Table 5-2 are

fabricated with four thin films. These test junctions are employed for weekly monitoring of the oxidation process and provide necessary rapid feedback when adjustment of the process is required. Process control in conjunction with this monitoring procedure characteristically results in  $J_n$  uniformities of  $\pm 10\%$  or better on a single substrate and control of  $R_n$  to about  $\pm 30\%$  between runs. Improved control in runs is being sought.

The uniformity which is achieved across the single wafers facilitates the fabrication of series arrays of junctions. The I-V characteristic of a typical array is shown in Fig. 5-5. The Josephson current in this low-leakage array has been suppressed with a magnetic field. Series junction arrays are being employed in the programmable analog signal-processing devices<sup>11</sup> to increase the dynamic range.

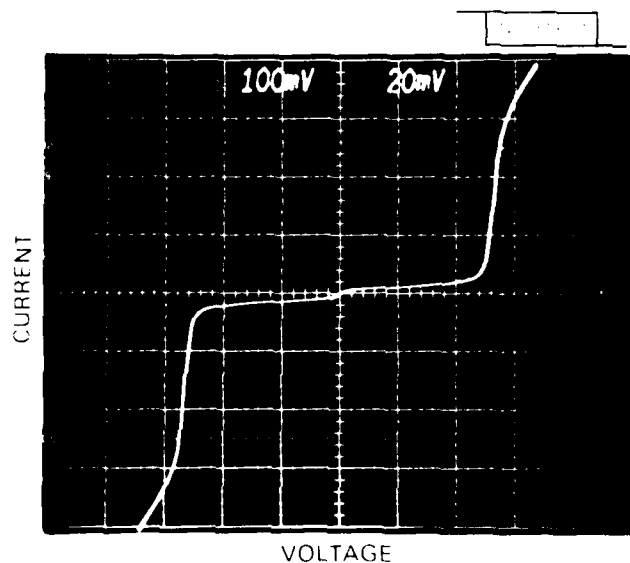


Fig. 5-5. I-V characteristics of a series array of 21 SIS junctions at 4.2°K.

Several Josephson test junctions have been tested at multiple-month intervals over a two-and-a-half-year span and, as indicated in Fig. 5-6, the average current density changed less than 15%. These junctions were stored at room temperature in a dry nitrogen atmosphere. These tests help to verify the mechanical ruggedness of niobium-based junctions and devices.

E.M. Macedo  
S.A. Reible

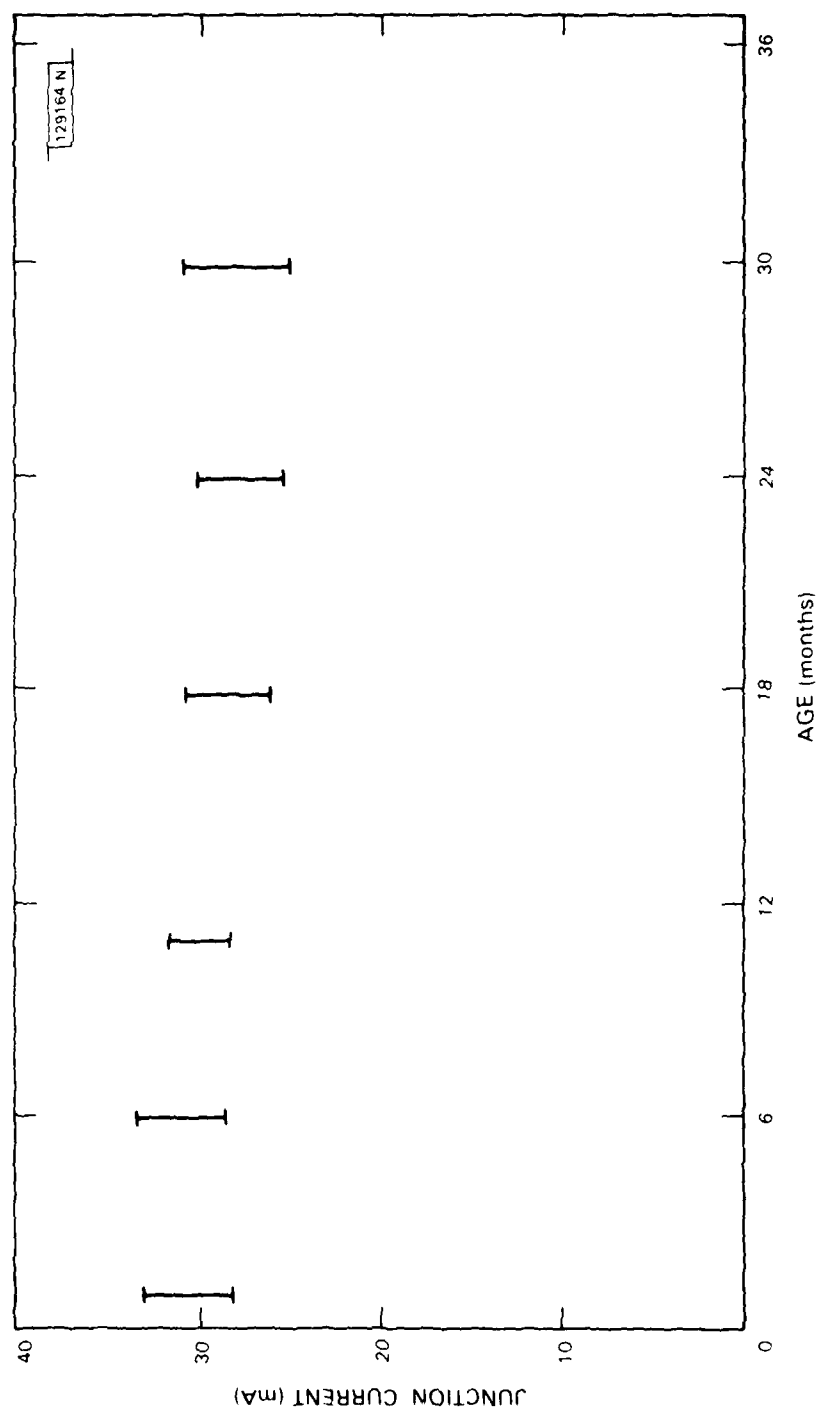


Fig. 5-6. Normal junction current at 4.2°K as a function of room-temperature storage time.



### 5.3 PARAXIAL ELECTROACOUSTIC COEFFICIENTS IN $\text{LiNbO}_3$ AND $\text{LiTaO}_3$ AND THEIR APPLICATION TO HOLOGRAPHICALLY WRITTEN BULK ACOUSTIC WAVE GRATINGS

#### 5.3.1 Experimental Determination of Electroacoustic Coefficients

The electroacoustic coefficients govern the modulation of the velocity of elastic waves in a solid via an electric field. These coefficients are members of a 5th-rank tensor. For the point group,  $3m$  which contains  $\text{LiNbO}_3$  and  $\text{LiTaO}_3$ , there are thirteen independent coefficients. Given a coordinate system where all but one of the electric field components are zero, the velocity modulation takes the form  $\Delta v_a/v_a = CE$ , where  $\Delta v_a/v_a$  is the relative velocity of the acoustic wave,  $E$  is the non-zero component of the electric field, and  $C$  is a coefficient that is a complicated function of the relative orientation of the  $E$  field, acoustic wavevector, crystal axis, and acoustic mode that is propagating. If all of the thirteen elements of the electroacoustic tensor were known,  $C$  could be calculated for any possible orientation. However, not all of the electroacoustic coefficients have been determined directly,<sup>12</sup> thus preventing accurate calculation of  $C$  except in a few special situations.

For a certain class of devices discussed in Sec. 5.3.2, the magnitude of  $C$  for a longitudinal  $Z$ -propagating wave with a paraxial electric field is of the utmost interest. Unfortunately, the required coefficients are among those not available accurately. The present study was done to measure  $C$  for  $\text{LiNbO}_3$  and  $\text{LiTaO}_3$  in the case of a  $Z$ -directed electric field.

The experimental determination employed a pulse interference technique, wherein a signal was delayed acoustically in the crystal sample and then beaten against an undelayed reference. The bulk acoustic wave was launched by an edge-bonded transducer.<sup>13</sup> Electrodes at either end of the sample allowed the application of the electric field.

The relative phase change is simply related to the velocity change of the elastic wave, and was measured to an accuracy of better than  $5 \times 10^{-8}$ . In practice, the accuracy of the velocity-change measurement depends not only on the accuracy of the relative-phase-change measurement, but also on the accuracy of previously determined piezoelectric coefficients,<sup>14</sup> and on the accuracy of the determination of the sample thickness. Data are shown in Fig. 5-7 giving the relative velocity change as a function of applied electric field for paraxial longitudinal waves in the  $Z$  direction in  $\text{LiNbO}_3$  and  $\text{LiTaO}_3$ . The slope of the curve is the coefficient  $C$ . Because of the aforementioned accuracy considerations, the values given for  $C$  in each case are good only to  $\pm 5\%$ , even though the linearity of the curve is much better. Data for other sample orientations and for larger field intensities have been collected and will be presented at a later date.

#### 5.3.2 Application to Holographically Written Acoustic Gratings

The coupling between the electric field and a traveling acoustic wave could provide an effective means to create a bulk-acoustic-wave grating within a crystal of  $\text{LiNbO}_3$  or  $\text{LiTaO}_3$  via the mechanism of a stored optical hologram, provided that the electroacoustic coefficients are large enough. It is possible to create a sinusoidal spatial variation of the  $Z$ -directed electric field in  $\text{LiNbO}_3$  or  $\text{LiTaO}_3$  through a hologram. In  $\text{LiNbO}_3$  this field can have a peak intensity greater than  $100 \text{ kV/cm}$ .<sup>15</sup> The sinusoidal field can then couple through the

129165 N

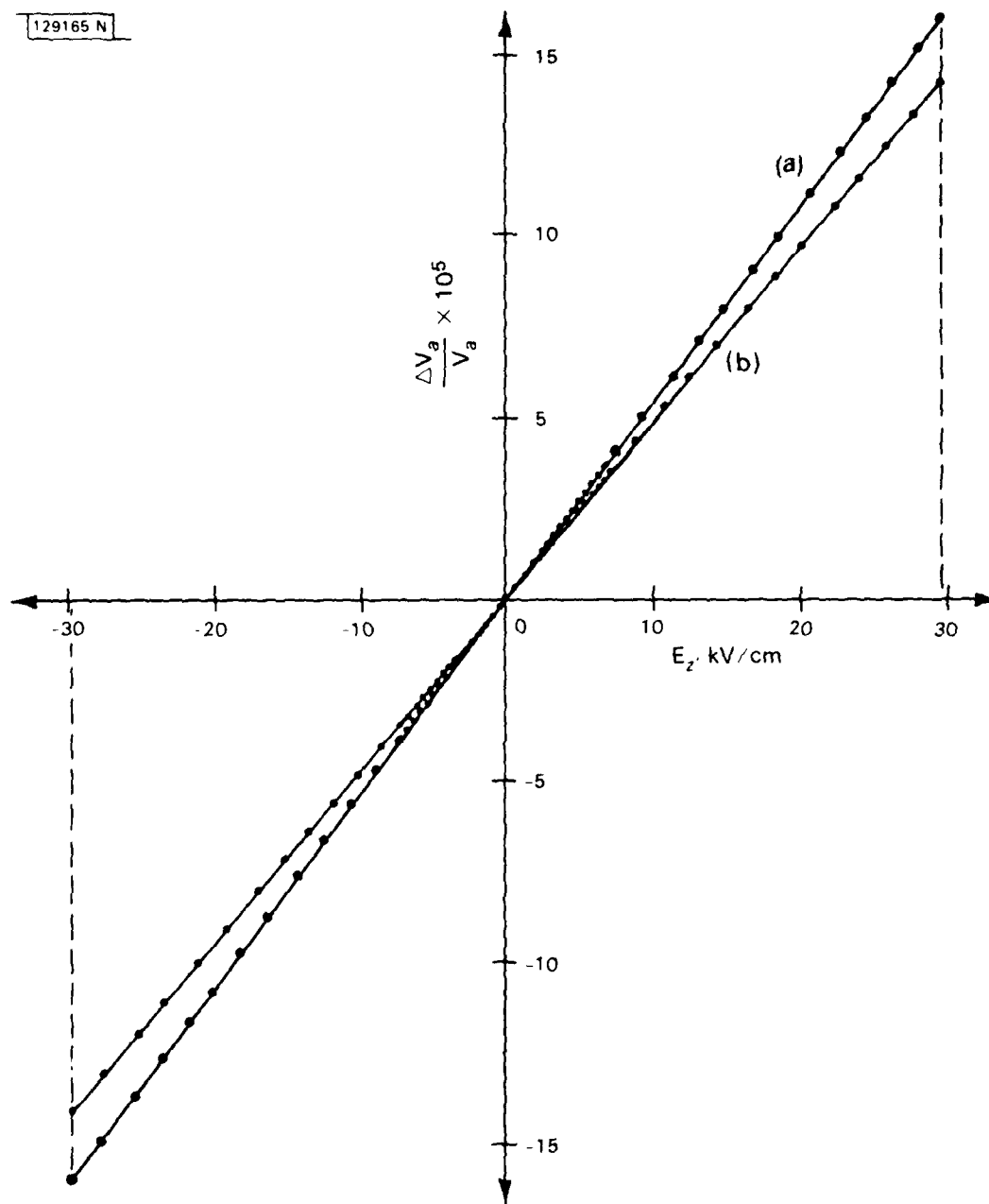


Fig. 5-7. Relative velocity change of a longitudinal Z-propagating bulk acoustic wave: (a) in  $\text{LiNbO}_3$ , (b) in  $\text{LiTaO}_3$ .

electroacoustic effect and through piezoelectrically induced density changes to create acoustic reflectors which collectively would form an acoustic grating.

To determine the order-of-magnitude strength of the interaction between a holographically formed grating and an acoustic beam, the grating can be modeled as  $N$   $\lambda$ -periodic acoustic transmission-line reflectors at the acoustic Bragg frequency.<sup>16</sup> If the acoustic wave is assumed undepleted, then the total grating reflection coefficient  $|\Gamma|$  is  $\approx 2N|\delta|$ , where  $\delta$  is the reflection coefficient of a single reflector. This reflection coefficient can be estimated from the changes in acoustic impedance. The impedance  $z$  is  $\rho v_a$ , where  $\rho$  is the material density and  $v_a$  is the acoustic velocity. A reflector is approximately modeled as material with  $z_0 = \rho_0 v_a$  butted against material with  $z_r = (\rho_0 + \Delta\rho)(v_a + \Delta v_a)$ . Using  $|\delta| = |z_0 - z_r| / |z_0 + z_r|$ , one finds, to first order in  $\Delta\rho/\rho_0$  and  $\Delta v/v_a$ ,  $|\delta| = 1/2 (\Delta\rho/\rho_0 + \Delta v_a/v_a)$ . From the  $\text{LiNbO}_3$  data above and the piezoelectric coefficients,  $|\Gamma| = (5.43 \times 10^{-4})N$  at a field of 100 kV/cm. For the interaction to be of practical interest, it is desirable to achieve  $|\Gamma| \sim 1$  for  $N$  no greater than  $10^5$ . It appears, then, that the proposed technique is feasible. The lithographic writing technique should allow convenient production of bulk acoustic gratings. Envisioned are a variety of grating devices (such as filters and pulse compressors expanders) that operate at high frequencies relative to their surface-acoustic-wave counterparts because of the reduced propagation loss of bulk waves.

P. Gottschalk  
D.E. Oates

## REFERENCES

1. Solid State Research Report, Lincoln Laboratory, M.I.T. (1982:3), p. 74, DTIC AD-A124305 4.
2. Solid State Research Report, Lincoln Laboratory, M.I.T. (1983:1), p. 83.
3. H. Muraoka, T. Ohhashi, and Y. Sumitomo in *Semiconductor Silicon 1973*, edited by Huff and R.R. Gurgess (Electrochemical Society, Princeton, New Jersey, 1973), p. 327.
4. G. Costabile, A.M. Cucolo, V. Fedykkin, S. Pace, R.D. Parmentier, B. Savo, and R. Vaglio, "Progress on Niobium Based Josephson Junction Technology," Internal Report 8777, Universita'Degli Studi Di Salerno, Salerno, Italy, 1977.
5. W.A. Phillips, *Physics of Dielectric Solids*, edited by C.H.L. Goodman (The Institute of Physics, Techno House, Bristol, UK, 1980), p. 64.
6. V.B. Braginsky and V.I. Panov, IEEE Trans. Magn. **15**, 30 (1979).
7. Solid State Research Report, Lincoln Laboratory, M.I.T. (1981:3), p. 26, DTIC AD-A112696 0.
8. Solid State Research Report, Lincoln Laboratory, M.I.T. (1983:1), p. 89.
9. Solid State Research Report, Lincoln Laboratory, M.I.T. (1979:3), p. 52, DTIC AD-A084270 8.
10. P.C. Karulkar and J.E. Nordman, J. Vac. Sci. Technol. **17**, 462 (1980); and Appl. Surf. Sci. **4**, 282 (1980).
11. S.A. Reible, A.C. Anderson, P.V. Wright, R.S. Withers, and R.W. Ralston, IEEE Trans. Magn. (in press).
12. B.A. Agishev, V.V. Lemanou, and N.K. Yushin, Sov. Phys.-Solid State **20**, 1629 (1978).
13. D.E. Oates and R.A. Becker, *1980 Ultrasonics Symposium Proceedings* (IEEE, New York, 1980), pp. 367-370, DTIC AD-A102964 4.
14. B.A. Auld, *Acoustic Waves and Fields in Solids, I* (Wiley, New York, 1973), p. 375.
15. D.L. Staebler, *Topics in Applied Physics: Holographic Recording Materials*, 20, edited by H.M. Smith (Springer-Verlag, New York, 1977), pp. 101-114.
16. More accurate coupled-wave calculations have been carried out by the authors in an unpublished work. The results of the simple model are borne out there.

UNCLASSIFIED

SECURITY CLASSIFICATION OF THIS PAGE (When Data Entered)

REPORT DOCUMENTATION PAGE		READ INSTRUCTIONS BEFORE COMPLETING FORM
1. REPORT NUMBER ESD-TR-83-029	2. GOVT ACCESSION NO. <i>A134 594</i>	3. RECIPIENT'S CATALOG NUMBER
4. TITLE (and Subtitle)  Solid State Research		5. TYPE OF REPORT & PERIOD COVERED Quarterly Technical Summary 1 February — 30 April 1983
7. AUTHOR(s)  Alan L. McWhorter		6. PERFORMING ORG. REPORT NUMBER 1983:2
9. PERFORMING ORGANIZATION NAME AND ADDRESS Lincoln Laboratory, M.I.T. P.O. Box 73 Lexington, MA 02173-0073		8. CONTRACT OR GRANT NUMBER(s)  F19628-80-C-0002
10. CONTROLLING OFFICE NAME AND ADDRESS Air Force Systems Command, USAF Andrews AFB Washington, DC 20331		10. PROGRAM ELEMENT, PROJECT, TASK AREA & WORK UNIT NUMBERS Program Element No. 63250F Project No. 6491.
12. MONITORING AGENCY NAME & ADDRESS (if different from Controlling Office)  Electronic Systems Division Hanscom AFB, MA 01731		12. REPORT DATE 15 May 1983
		13. NUMBER OF PAGES 9
		15. SECURITY CLASS. (of this report) Unclassified
		15a. DECLASSIFICATION DOWNGRADING SCHEDULE
16. DISTRIBUTION STATEMENT (of this Report)  Approved for public release; distribution unlimited.		
17. DISTRIBUTION STATEMENT (of the abstract entered in Block 20, if different from Report)		
18. SUPPLEMENTARY NOTES  None		
19. KEY WORDS (Continue on reverse side if necessary and identify by block number)		
solid state devices	photodiode devices	infrared imaging
quantum electronics	lasers	surface-wave transducers
materials research	laser spectroscopy	charge-coupled devices
microelectronics	imaging arrays	acoustoelectric devices
analog device technology	signal processing	
20. ABSTRACT (Continue on reverse side if necessary and identify by block number)		
<p>This report covers in detail the solid state research work of the Solid State Division at Lincoln Laboratory for the period 1 February through 30 April 1983. The topics covered are Solid State Device Research, Quantum Electronics, Materials Research, Microelectronics, and Analog Device Technology. Funding is primarily provided by the Air Force, with additional support provided by the Army, DARPA, Navy, NASA, and DOE.</p>		

UNCLASSIFIED

SECURITY CLASSIFICATION OF THIS PAGE (When Data Entered)